

MAGNETOPLASMDYNAMIC CHANNEL FLOW
FOR DESIGN OF COAXIAL MPD THRUSTERS

David Quimby King

A DISSERTATION
PRESENTED TO THE
FACULTY OF PRINCETON UNIVERSITY
IN CANDIDACY FOR THE DEGREE
OF DOCTOR OF PHILOSOPHY

RECOMMENDED FOR ACCEPTANCE BY THE
DEPARTMENT OF
MECHANICAL AND AEROSPACE ENGINEERING

June 1982

CONTENTS

Title Page	i
Acknowledgements	ii
Table of Contents	iii
List of Illustrations	v
Notation	vii
Abstract	x

<u>Chapter</u>	<u>Page</u>
1. INTRODUCTION	1-1
Thesis Organization	1-4
2. GEOMETRY EXPERIMENTS	2-1
A: Introduction	2-1
B: Experimental Facility and Diagnostics	2-1
C: Electrode Geometry Exploration	2-7
D: Effect on the Onset Current	2-10
E: Specific Impulse and Efficiency	2-18
F: Summary	2-30
3. 1-D, IDEAL GAS, STEADY, ACCELERATING, MPD CHANNEL FLOW	3-1
A: Introduction	3-1
B: The 1-D Analysis	3-4
C: The Electric Field Related To Mach 1	3-7
D: The "Cold" Inlet Simplification of the Governing Equations	3-9
E: The Dimensionless Electric Field	3-11
F: Accelerating Flows on the u-B Plane	3-15
G: The Magnetic Reynolds Number	3-21
H: Electric Field Characteristics for Fixed Length Electrodes	3-25
I: Modeled Effects of Length and Mass Flux	3-27
J: Summary	3-29

4.	REAL GAS EFFECTS IN 1-D MPD FLOW	4-1
A:	Introduction	4-1
B:	Real Gas Channel Equations	4-2
C:	Differences Between Ideal and Real Gas Analyses	4-5
D:	Magnetic Reynolds Number	4-8
E:	Simple Thermodynamics of MPD Channels	4-15
F:	Role of Tensor Conductivity	4-16
G:	Effect of Tensor Conductivity	4-22
H:	1-D Streamtube "Terminal" Characteristics	4-23
I:	Comparison of Theory and Experiment	4-31
J:	Summary	4-34
5.	APPLICATIONS OF THE 1-D REAL-GAS MODEL	5-1
A:	Introduction	5-1
B:	Voltage-Current Characteristics and Electrode Geometry	5-1
C:	Onset Limit and Thruster Geometry	5-3
D:	Thrust Efficiency and Electrode Design	5-4
E:	Summary	5-7
6.	CONCLUSIONS	6-1

APPENDICIES

A1.	Additional Calculations for Ideal Gas Acceleration	A1-1
A2.	Approximate Real Gas State Equation	A2-1
A3.	Solution of 1-D Real Gas MPD Channel Equations	A3-1
A4.	Real Gas Model - Interpolator of Results	A4-1
REFERENCES	R-1

LIST OF ILLUSTRATIONS

Figure	Title	Page
1.1	Coaxial MPD Accelerator Schematic	1-2
2.1	Nominal 10 cm Research Thruster	2-2
2.2	MPD Apparatus	2-4
2.2.1	Current and Voltage Signature $\dot{m}=6$ g/sec	2-5
2.3	Onset Current, J^* , $\dot{m}=6$ g/sec	2-8
2.4	Voltage Current Characteristics, $\dot{m}=6$ g/sec	2-11
2.5	Oscillatory Voltage Amplitude, $\dot{m}=6$ g/sec	2-12
2.6	Onset Current for Various Anodes	2-14
2.7	Onset Current J^* vs. Anode Orifice Radius	2-17
2.8	Current Contours (VFP 11-6)	2-21
2.9	Current Contours (VFP 21-12)	2-22
2.10	Voltage for Various Anodes	2-25
2.11	Various Anode Orifice Characteristics	2-26
2.12	Inferred Thrust Efficiency	2-28
2.13	Thrust Efficiency vs. Specific Impulse	2-29
3.1	Schematic of the Martinache Model	3-2
3.2	1-D Model Schematic	3-6
3.3	Dimensionless Electric Field (Ideal Gas)	3-14
3.4	Ideal Gas, Electrothermal Mode Acceleration Profile, $\beta_0 = 1/4$, $\gamma = 5/3$	3-16
3.5	Ideal Gas, Electromagnetic Mode Acceleration Profile, $\beta_0 = 1/6.68$, $\gamma = 5/3$	3-18
3.6	Ideal Gas, Transition Mode Acceleration Profile, $\beta_0 = 5/27$, $\gamma = 5/3$	3-20
3.7	Magnetic Reynolds Number vs. β_0 , $\gamma = 5/3$	3-22
3.8	Electric Field vs. Magnetic Field, $\gamma = 5/3$	3-26

3.9	Exhaust Enthalpy vs. Electrode Length and a Velocity Scale	3-28
4.1	Argon Equilibrium Equation of State	4-3
4.2	Real Gas Electromagnetic Mode Acceleration Profiles, $\beta_0 = 1/4$, $F = 1.0$	4-6
4.3	Mach Number Profiles $\beta_0 = 1/4$, $F = 1.0$	4-7
4.4	Illustration of 3 Cases of Rm Computation.	4-10
4.5	Real Gas Magnetic Reynolds Number	4-11
4.6	Dimensionless Electric Field (Real Gas)	4-13
4.7	Lorentz Efficiency	4-17
4.8	Streamtube Electric Field vs. Current for $L = 0.2$ m .	4-24
4.9	Streamtube Computed Electric Field vs. Current for 3 Lengths, $F = 3$ kg/m ² -sec	4-25
4.10	Streamtube Exhaust Characteristics	4-26
4.11	Streamtube Thrust Efficiency	4-28
4.12	Streamtube Lorentz Efficiency	4-30
4.13	High Aspect Ratio Thrusters	4-32
4.14	Radial Electric Field vs Current, $\dot{m} = 3$ g/sec	4-34
4.15	Radial Electric Field vs Current, $\dot{m} = 6$ g/sec	4-35
4.16	Radial Electric Field vs Current, $\dot{m} = 9$ g/sec	4-36
5.1	Measured and Computed Voltage-Current Characteristics for two High Aspect Ratio Thrusters	5-2
5.2	Thruster Design for Improved Thrust Efficiency . . .	5-5
A1.1	$B'_{T=0}$ vs $1/\beta_0$	A1-2
A2.1	Argon Scalar Conductivity	A2-3
A2.2	Enthalpy vs Temperature (Argon)	A2-4

NOTATION

Symbol	Useage
a	Isentropic Speed of Sound
B	Magnetic Field
C_0	Constant in Momentum Equation
D	Electric Displacement
E	Electric Field
f	Thrust
f_{em}	Electromagnetic Component of Thrust
F	Mass Flux
g	State Equation
G	Approximate State Equation
g_g	Earth gravitational constant
h	Enthalpy
h_{zi}	Reference Enthalpy (5.8154E7 J/kg)
I_{sp}	Specific Impulse
j	Current Density
J	Terminal Current
J^*	Onset Current
k	Constant in Electromagnetic Thrust Equation
L	Electrode Length
m	Mass Flow
n	Number Density
p	pressure
r_{ac}	Ratio of Effective Anode Current Attachment Radius to Cathode Attachment Radius

R	Ideal Gas Constant
\bar{R}	Collision Frequency in units of resistivity
R_a	Effective Anode Current Attachment Radius
R_c	Effective Cathode Current Attachment Radius
R_m	Magnetic Reynolds Number
s	Entropy
S_t	Transverse Magnetic Interaction Parameter
T	Temperature
u	Velocity
V	Terminal Voltage
X_a	Anode Length
X_c	Cathode length
X_f	Anode Face Position
z	Average Charge Per Atom in units of number of electrons
β_0	Ratio of Inlet Pressure to Magnetic Pressure
γ	Ratio of Specific Heats
ϵ_0	Permittivity of Free Space
\mathcal{E}	Dimensionless Energy Scale $((B_0^2/2\mu_0 F)^2/h_{zi})$
η	Thrust Efficiency
η_L	Lorentz Efficiency
μ_0	Magnetic Permeability of Free Space
ν_c	Collision Frequency
\mathcal{E}	Dimensionless Electric Field $(E/(B_0^3/2\mu_0 F))$
ρ	Mass Density

- σ Electrical Conductivity
- σ_{∞} Reference Conductivity (7800 mho/m)
- ϕ_{TP} Fraction of Current on Cathode Tip
- ω_b Electron Gyro Frequency
- Ω Hall Parameter

Modifiers

- The subscript $_o$ refers to the inlet, $_e$ refers to the exit, and $_s$ indicates a stagnation quantity.
- The subscript $_+$ refers to a supersonic region, and $_-$ to a subsonic region.
- The superscript $*$ refers to a quantity at Mach 1, except for J^* above.
- The $'$ indicates a non-dimensional quantity.

ABSTRACT

The current, mass flow, and electrode geometry of self-field, coaxial MPD thrusters are related to terminal characteristics such as voltage, specific impulse and thrust efficiency by both experiment and a simple 1-D model. For high power, magnetically accelerated flows, analysis shows that the gas is subsonic near the inlet, and that the terminal voltage has a strong dependence on the electrode geometry up to and including the sonic location. The electrode configuration in the downstream, supersonic portion strongly affects the exit Mach number, which for argon propellant can be as high as 6 or more. Experiments show that terminal voltage-current characteristics remain unchanged within the error bar, when the downstream 9/10 ths of a long cylindrical thruster is flaired to a 3:1 expansion ratio. Thrust efficiency however, is improved in the flaired thruster and is 1.5 that of the cylindrical thruster.

The 1-D model, with an equilibrium argon state equation, compares favorably with experiments in that the parametric behavior of computed and measured electric fields is the same for current and mass flow variations. By relating the thermodynamics of heat and energy addition to plasmadynamic quantities, the model shows that the thrust efficiency has an asymptote of 0.70 at large magnetic Reynolds numbers. Ignoring electrode losses, the model predicts thrust efficiencies of 65% at 1500 secs and 70% above 3000 secs specific impulse.

Previous experiments have shown that thrust efficiency and specific impulse are limited by severe erosion which is accompanied by voltage oscillations. Experiments in this thesis show that this limit is improved for both longer electrodes and anodes of smaller diameters. The model shows that axial profiles of the Hall parameter are reduced for these geometry changes. Thus, longer electrodes and smaller anode diameters postpone the occurrence of large and perhaps critical Hall parameters.

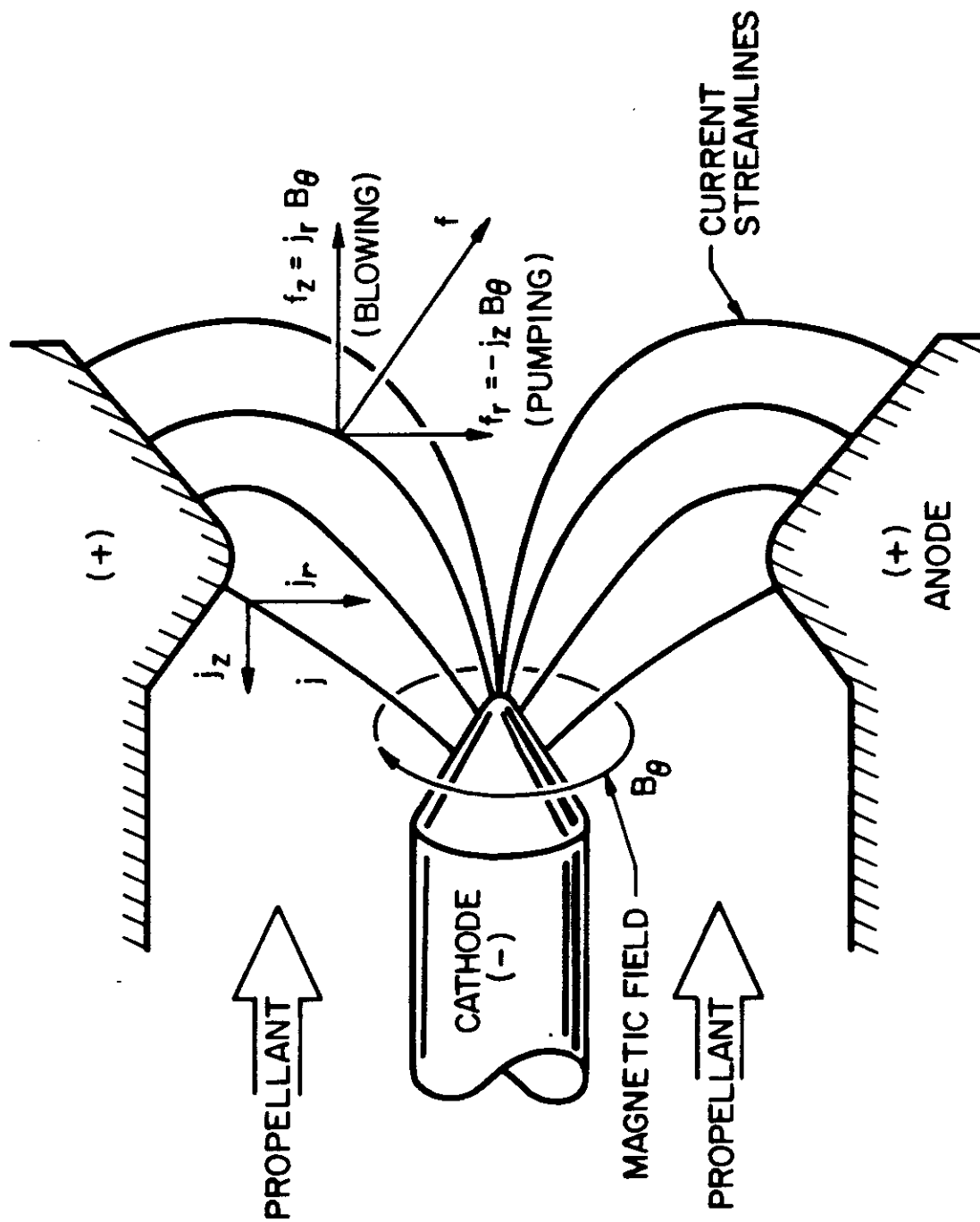
Chapter 1

INTRODUCTION

Electric propulsion can provide spacecraft with large velocity increments for a modest expenditure of reaction mass¹. Chemical systems do not enjoy this advantage since the energy release is chemically bound to the reaction mass and this limits the ultimate exhaust velocity or specific impulse. The separation of the energy source from the propellant chemistry permits electric thrusters to achieve large specific impulse or, in other words, large directed kinetic energy per unit of thrust.

Although a power supply is required, its additional mass can be more than offset by propellant savings, making electric propulsion attractive for high ΔV missions.² A Solar Electric Propulsion Stage (SEPS) has been considered for power levels less than 100 kWe.^{3,4,5} For power levels of 100 kWe and missions far from the sun, nuclear-electric propulsion is under development⁶ and according to NASA, "... is the ultimate system for transportation in the solar system."⁷ A nuclear-thermoelectric supply has also been proposed as the heart of an electrically propelled orbital transfer vehicle.^{1,8}

The coaxial MPD thruster is a self-field accelerator produces a large $j \times B$ (current density cross magnetic field) body force and a high thrust density. A schematic of the thruster, fig. 1.1, shows current streamlines, the magnetic field and the direction of the body force. The anode is the outer electrode and typically passes tens of kiloamperes through the plasma to the



SELF - FIELD MPD ACCELERATOR

FIGURE 1-1

AP 25 5033

center cathode. A nominal 10 cm diameter thruster consumes 6 megawatts of power and accelerates 6 g/sec of argon to 25 km/sec which yields 150 N of thrust. At these conditions the electromagnetic body force acceleration dominates any thrust due to thermal expansion. The net electromagnetic force on the propellant can be found by integrating $\mathbf{j} \times \mathbf{B}$ over the current conducting volume. By using Maxwell's stress tensor, the volume integral is replaced with a surface integral of magnetic pressure, and for the coaxial MPD thruster can be written:¹⁰

$$f_{em} = b J^2 \quad (1a)$$

$$b = \frac{\mu_0}{4\pi} \left(\ln \frac{R_a}{R_c} + k \phi_{TIP}^2 \right) \quad (1b)$$

where R_a and R_c are the effective anode and cathode current attachment radii, k is a geometric constant of order 0.2, and ϕ_{TIP} is the fraction of current on the cathode tip. For the nominal 10 cm thruster, b is about $2E-7$ (MKS) and 27 kA is required to develop 150 N of thrust.

The specific impulse, defined as exhaust velocity over the gravitational constant, is related to thrust and mass flow (\dot{m}):

$$I_{SP} = \frac{f}{\dot{m} g_E} \approx \frac{f_{em}}{\dot{m} g_E} = \frac{b J^2}{\dot{m} g_E}$$

Specific impulse increases with J^2/\dot{m} up to a critical value where experiments have shown a geometry dependent limit.^{11,12,13,14} When operated at and above the critical value of J^2/\dot{m} , the thruster exhibits an abrupt and severe increase in insulator and electrode erosion, large megahertz voltage oscillations, and a bright, cylindrical layer surrounding the cathode located at

twice the cathode radius. Measurements show that the layer exists in a region of large power deposition and high Hall parameter.¹⁴ The mechanisms causing the erosion and voltage oscillations are not fully understood, but the onset of these phenomena, called the onset limit, places a ceiling on the useful operational range of the thruster.

In a broad sense, this thesis addresses two major problems confronted in the design of high specific impulse, high efficiency MPD thrusters. The first problem encountered in thruster design is the inability to relate or accurately compute terminal voltage-current or thrust efficiency - specific impulse characteristics to the electrode geometry. The second problem is a lack of understanding of the relationship between electrode geometry and the processes that limit thrust efficiency and specific impulse.

Thesis Organization

The focus of this thesis is to develop an understanding that will aid in the design of high efficiency MPD thrusters. To do so a combined experimental and analytical attack is executed. In chapter 2, experiments which explore the effects of electrode geometry on thrust efficiency and specific impulse are presented. These show that electrode length and anode radius have a strong effect on performance, but the information is not sufficient to fully explain the underlying phenomena. In chapter 3, a 1-D idealized analysis of the acceleration process is undertaken. This analysis is improved over previous work in that solutions are algebraically simpler. These solutions are used to explain

and illustrate the behavior of accelerating MPD channel flow. Chapter 4 extends the theory to include ionization and tensor conductivity phenomena. Also, the thermodynamics and plasmadynamics of MPD channel flow are used to describe the thrust efficiency limiting process in the channel. This chapter is the cornerstone of the thesis as the model is found to be in parametric agreement with experiment; i.e. the model is a valid and useful tool in understanding accelerating MPD flow. From this model, an explanation of some experimental geometry effects is given. Chapter 5 extends the understanding of MPD flow to a technique for design of high efficiency thrusters. A new thruster geometry is designed, built, and tested wherein terminal voltage is primarily controlled by inlet configuration while exhaust temperature and velocity are primarily controlled by the downstream electrode configuration.

Chapter 2

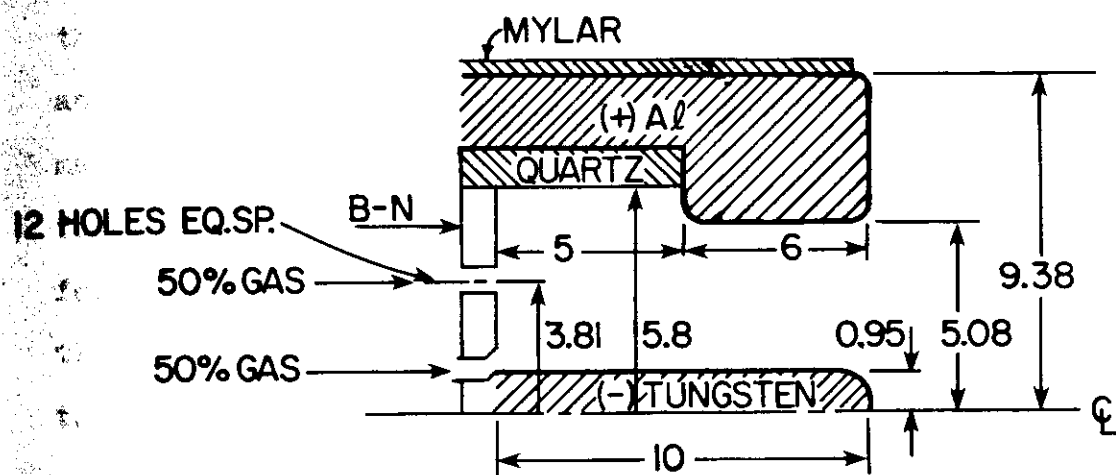
GEOMETRY EXPERIMENTS

A: INTRODUCTION

The design of high efficiency MPD thrusters can be pursued in two ways: 1) by exploring terminal characteristics, and developing a phenomenological view of the thruster, and 2) by exploring the detailed conduction processes, electric and magnetic fields, and state properties of the gas. Certainly the two are related, and combining the two perspectives should provide a clear understanding and a sound basis for design of the thruster. This chapter explores the terminal phenomenology in a series of electrode geometry experiments and then suggests a course for a more detailed investigation of the acceleration process.

B: EXPERIMENTAL FACILITY AND DIAGNOSTICS

The current MPD thruster has evolved over a period of years, and now provides repeatable operation from a flexible design that is amenable to many diagnostics.^{13,15,16,17,18} A baseline 5 MWe pulsed, 10 cm thruster is shown in fig. 2.1 with an aluminum anode, tungsten cathode, and quartz or boron-nitride insulators. These materials have been selected for ease of machining and resistance to erosion.¹⁹ Special attention has been given to the mass injection geometry which has a very strong influence on the steady operation of the thruster.^{17,18}



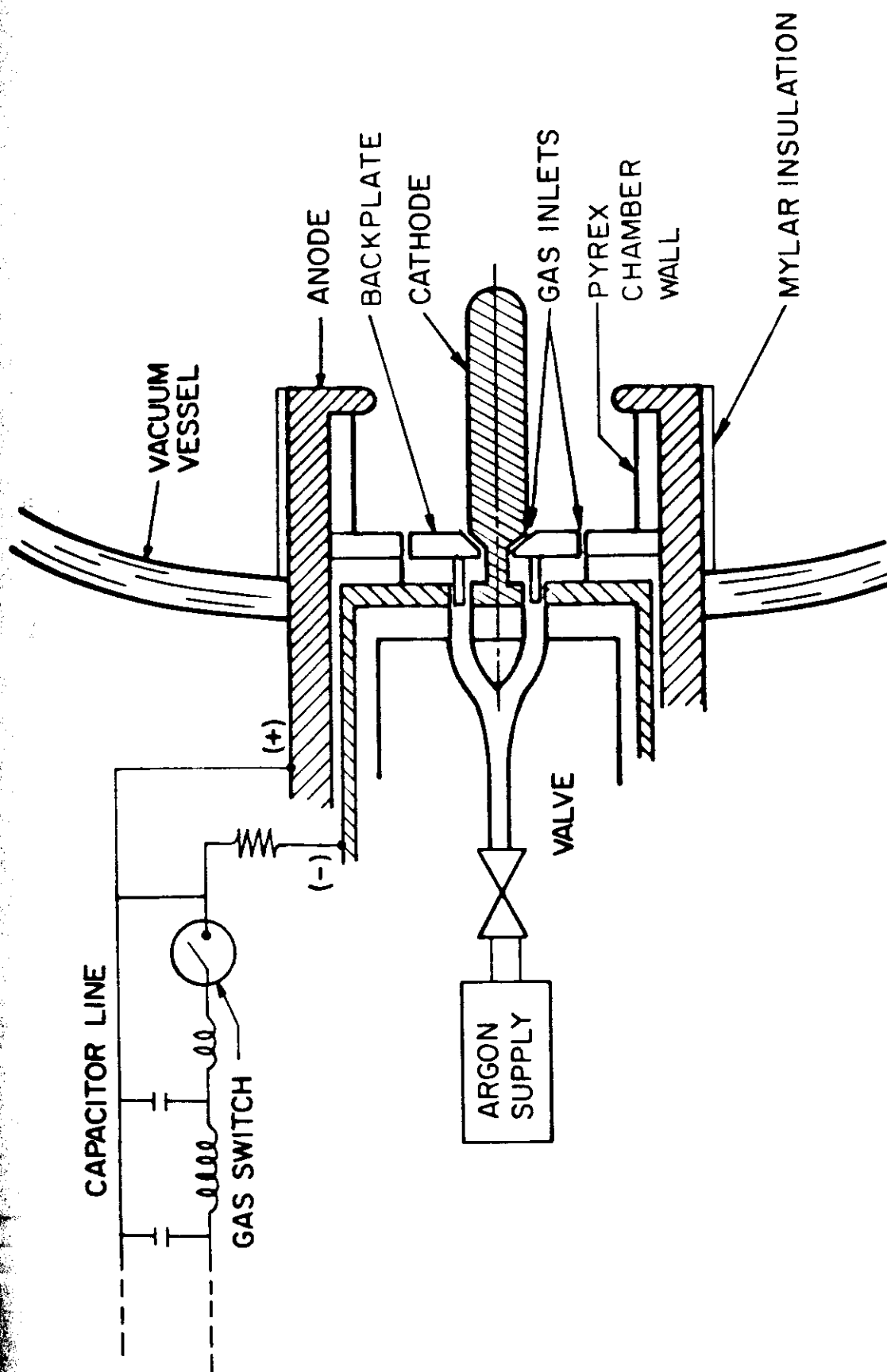
NOMINAL 10cm DIAMETER RESEARCH THRUSTER

FIGURE 2-1

Specifically, the radial position of the outer twelve holes has been tuned for the lowest terminal voltage operation. Half the mass is distributed, via choked orifices, through the outer 12 holes, with the other half through an annulus around the base of the cathode.

Experiments are conducted in a 1.5x1.0 m dia. dielectric vacuum tank providing thruster operation with a minimum of electromagnetic and background gas interference.¹⁹ To initiate quasi-steady operation, the tank is evacuated to 10^{-5} torr, and the propellant is admitted through a solenoid valve to the choked orifices in the thruster (fig. 2.2). After 10 ms, the propellant flow is steady and a capacitor line²⁰ is discharged through a gas switch,²¹ a matching 0.150 Ω resistor, and the thruster. Quasi-steady operation follows in generally less than 200 μ s. The 330 μ f L-C ladder network forms one rectangular current pulse of either 1.0 or 0.5 ms duration. With the present switch gear, the 1 ms line can deliver up to a 26 kA pulse, and for 0.5 ms up to a 52 kA pulse.

The total current is monitored by a 120.6 $\mu\Omega$ stainless steel, shielded, low inductance shunt in series with the grounded anode, and the terminal voltage is measured by a Tektronix P6013 voltage probe. The signals are carried by coax cable dressed along a 1x3.5 m ground plane to an oscilloscope housed in a Faraday cage. The typical oscillogram in fig 2.2, shows terminal voltage and current for a benchmark thruster.

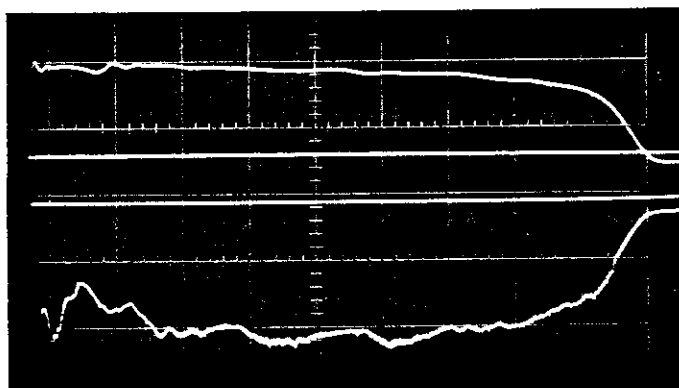


MPD APPARATUS

FIGURE 2.2

ARC CURRENT, J
7.7 kA/DIV

ARC VOLTAGE, V
50 V/DIV



→ | ← 100 μ sec

CURRENT AND VOLTAGE SIGNATURES

FIGURE 2-2-1

The ground plane and Faraday cage form an electrical umbrella which permits small signal measurements to be made with acceptable signal to noise ratios. For instance, the magnetic field is measured by a 120 turn inductor,²² wound on a 2x2 mm cylinder. The coil is mounted on a 40 cm glass rod, and a shielded and twisted pair conduct the signal through a port in the tank wall. The signal is integrated by an operational amplifier providing a measurement range from 0.01 Tesla with 1 megahertz frequency response and a 7% absolute error.

The electric field in the thruster is determined from the difference in floating potential measured by a 2 mm spacing double Langmuir probe. Each electrode is 0.25 mm dia. by 2.5 mm long tungsten wire held by a drawn and tapered 2 mm dia. quartz tube. Each probe signal, which may reach 100 V, is attenuated 10x by a high impedance voltage probe and then connected to a Tektronix 22 differential preamp. The difference signal may be 1 V or less, but may contain 0.5 V amplitude megahertz noise which is cut off by a 30 kHz low pass filter. The system can measure a 0.05 V difference with 10% absolute error. To ensure reproducible results, deposits on the probe are removed by a 3 minute, 10 mA glow discharge between the probe electrodes and the thruster anode, after exposure to 5 plasma pulses.

Axial exhaust velocity is also measured by two double Langmuir probes,²³ axially displaced by 5 cm. These observe time-of-flight fluctuations in plasma properties, reflected in the ion saturation currents of the two probes. Each double probe has 0.25 mm dia. by 6 mm long electrodes separated by 2.5 mm.

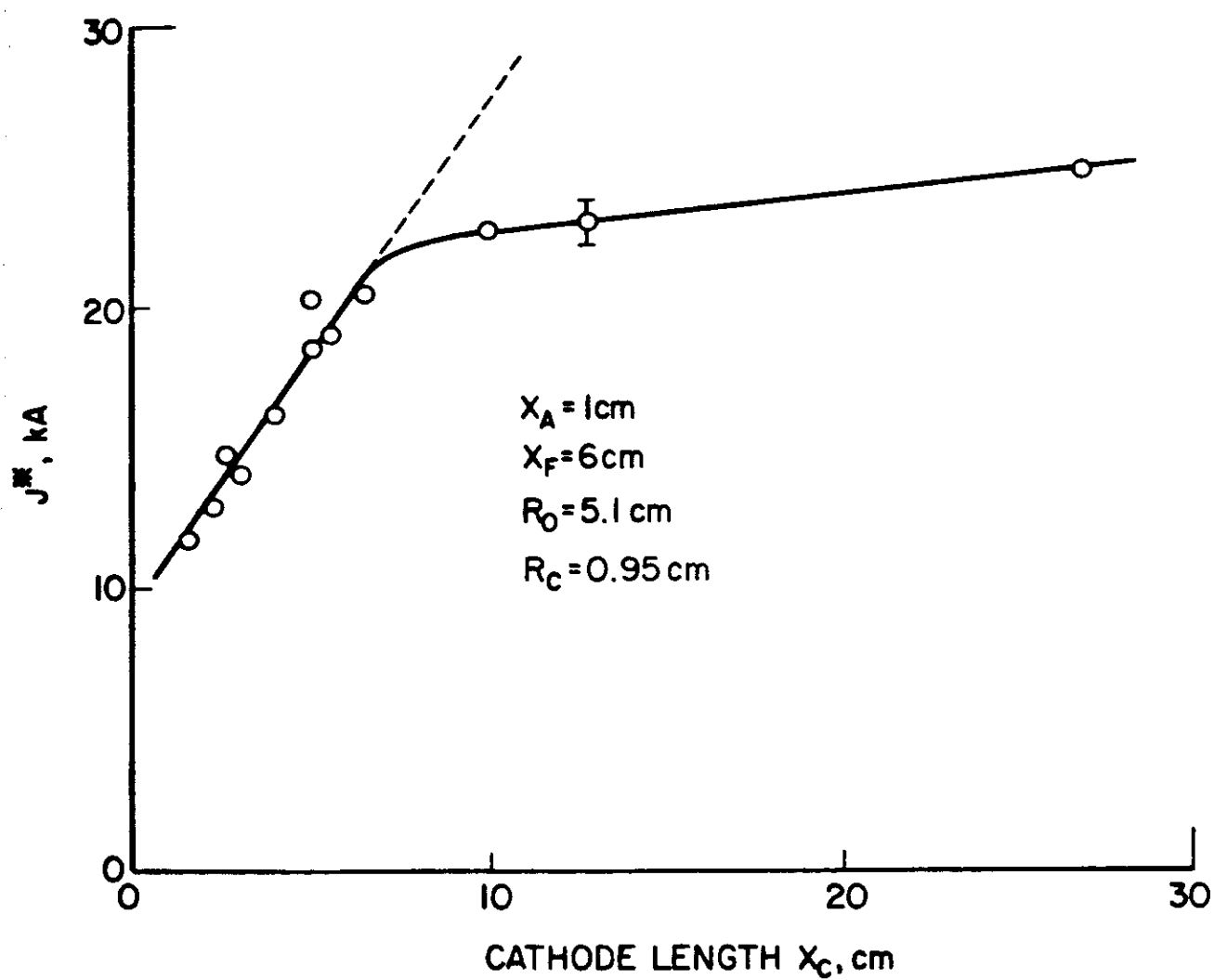
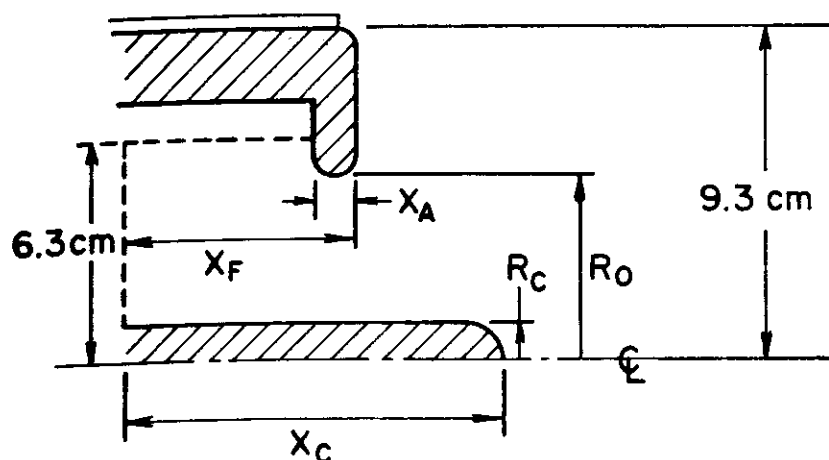
the system frequency response limits the maximum measurable velocity to 50 km/s.

2. ELECTRODE GEOMETRY EXPLORATION

Data giving the performance limit for changes in cathode length are well established. Examination of these data suggests a course for further geometry exploration. The increase in the onset parameter which results from increasing the cathode length^{24,25} is shown in fig 2.3. Since these data were obtained with a fixed mass flow of 6 g/sec, the onset condition is denoted simply by J^* , which increases rapidly for short cathodes, reaching an asymptote of about 30 kA for longer cathodes. Referring to the sketch of the arc chamber at the top of the figure, the knee of the curve occurs where the cathode tip is even with the anode plane, suggesting that the anode position and dimensions may also play a role in establishing the onset condition.

To further investigate the effect of electrode configuration and location on the thruster operation, a total of 13 tests have been conducted with 7 different anodes and 3 cathodes. These anodes are of fixed outer radius (9.3 cm), but varying orifice diameter, X_o , and axial extent, X_a , while the cathodes are of three different lengths, X_c , at a fixed diameter of 1.9 cm. A selection of pyrex chamber wall insulators allows independent position of the downstream face of the anode relative to the chamber backplate, X_f .

Table I shows the division of the experiments into three major groups according to changes in key dimensions as shown in fig 2.3:



ONSET CURRENT, J^*
 $\dot{m} = 6 \text{ g/sec}$

FIGURE 2.3

Table I Thruster Configurations

Thruster Designation	X_F	Dimensions (cm)		
		X_A	R_O	X_C
VFP 3-1	3.5	1.0	5.1	10.0
VFP 6-1 (Benchmark)	6.0	1.0	5.1	10.0
VFP 6-6	6.0	6.0	5.1	10.0
VFP 8-3	8.5	3.5	5.1	10.0
VFP 8-6	8.5	6.0	5.1	10.0
VFP 8-8	8.5	8.5	5.1	10.0
VFP 11-1	11.0	1.0	5.1	10.0
VFP 11-6	11.0	6.0	5.1	10.0
VFP 21-21	21.6	21.6	5.1	10.0

VCL 10	21.6	21.6	5.1	10.0
VCL 20	21.6	21.6	5.1	20.0

VAO 3	6.0	1.0	3.2	5.0
VAO 4	6.0	1.0	4.1	5.0
VAO 5	6.0	1.0	5.1	5.0

first group examines the effect of Varying anode Face Position (VFP) for anodes of differing axial extent with fixed orifice diameter and fixed cathode length; the second group tests Varying Cathode Length (VCL) for a given long anode; and the third group examines Varying Anode Orifice diameter (VAO) for fixed anode position, axial extent and cathode length. The numbers in a particular designation refer to the principal variable for that test series, e.g., VFP 6-1 refers to an anode with its outer face 6 cm from the number back plate, and a 1-cm axial extent.

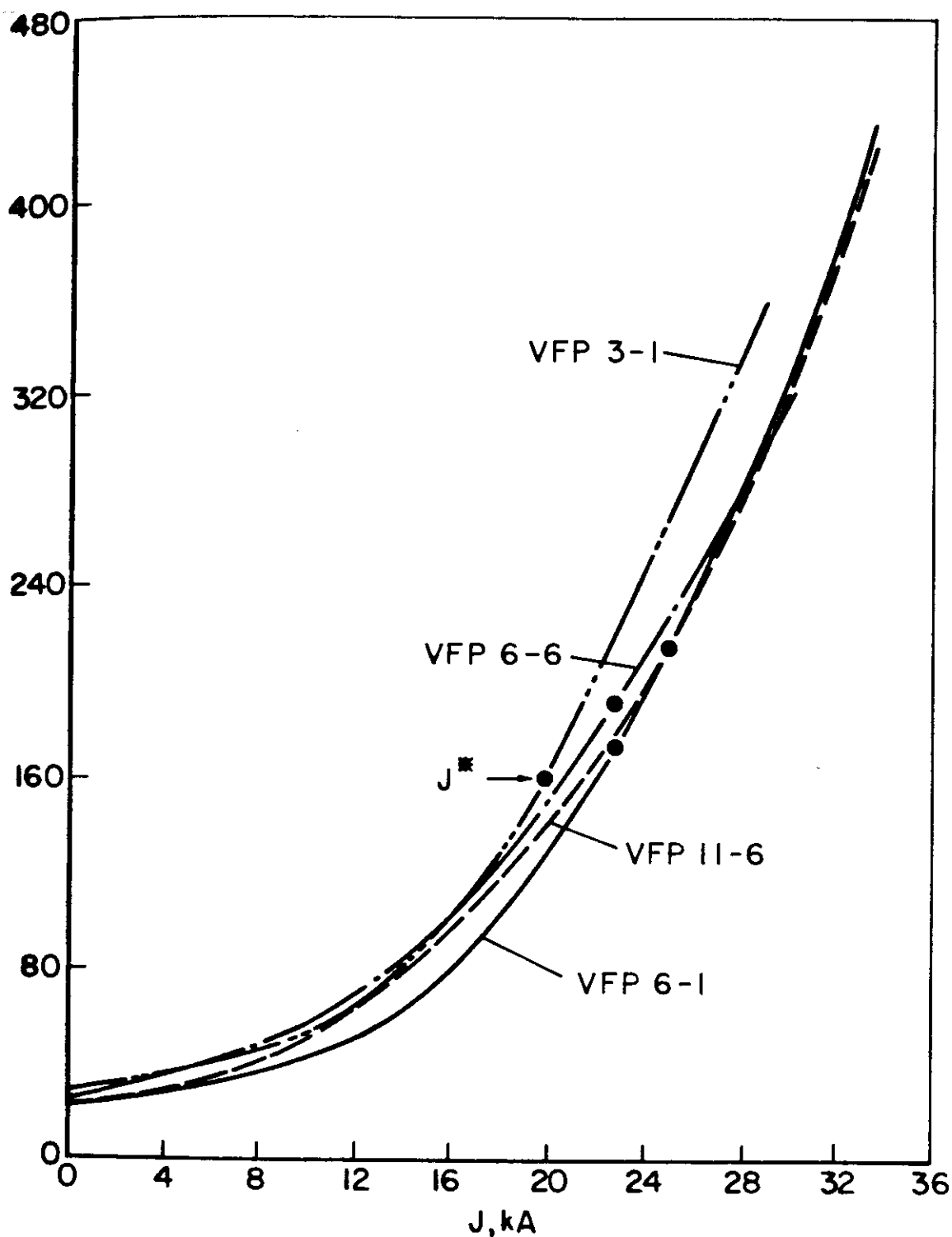
RESULTS

EFFECT ON THE ONSET CURRENT

For all of the electrode configurations tested, the onset current is considered to be the primary dependent variable. Consequently, voltage-current characteristics have been obtained for all configurations, samples of which are shown in fig 2.4. Some of the anodes used to assess the effects of anode position and axial extent. The characteristics show the familiar transition from a weak current dependence at low current to a higher current dependence at higher current, usually associated with the transition from electrothermal acceleration to a process dominated by electromagnetic forces.

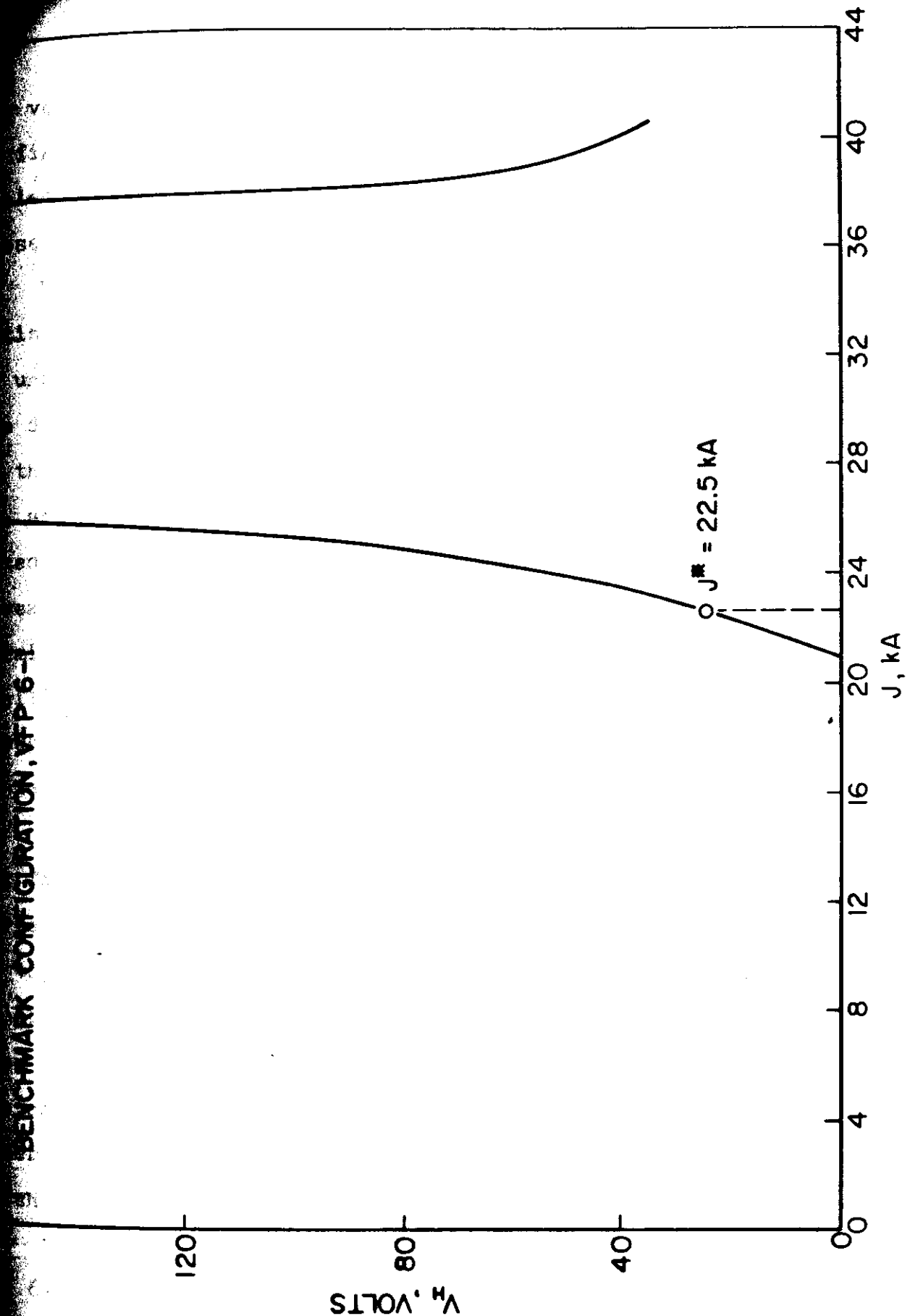
For each anode, the value of J^* has been determined using the criterion indicated in fig 2.5. Here, the peak-to-peak amplitude of the terminal voltage oscillation, V_h is plotted as a function of current. The onset current J^* is defined as that current for which the amplitude of V_h reaches 10% of the mean.

BOUNDARY CONFIGURATION, VFP 6-1 V_T , VOLTS



VOLTAGE CURRENT CHARACTERISTICS
 $\dot{m} = 6$ g/sec

FIGURE 2.4



OSCILLATORY VOLTAGE AMPLITUDE

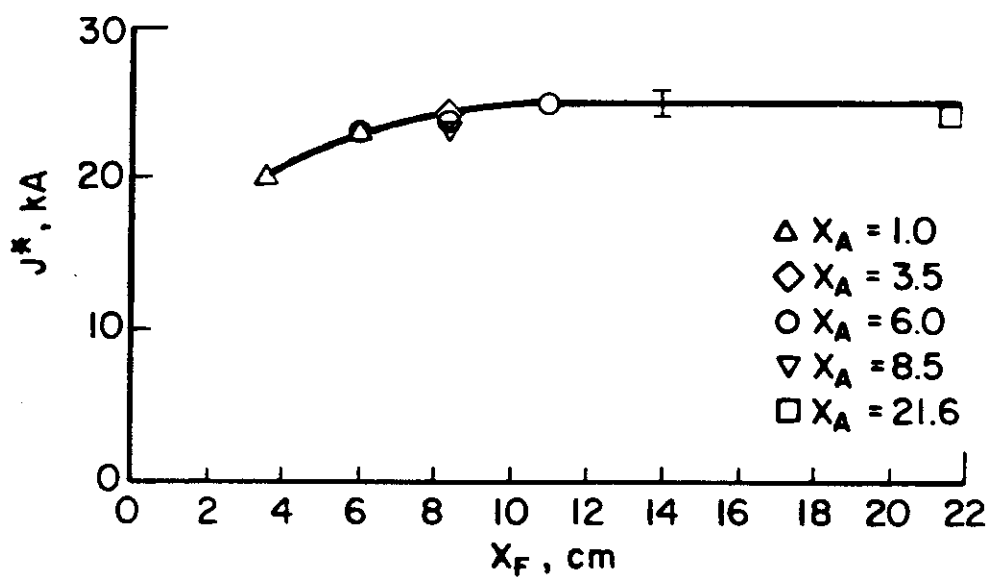
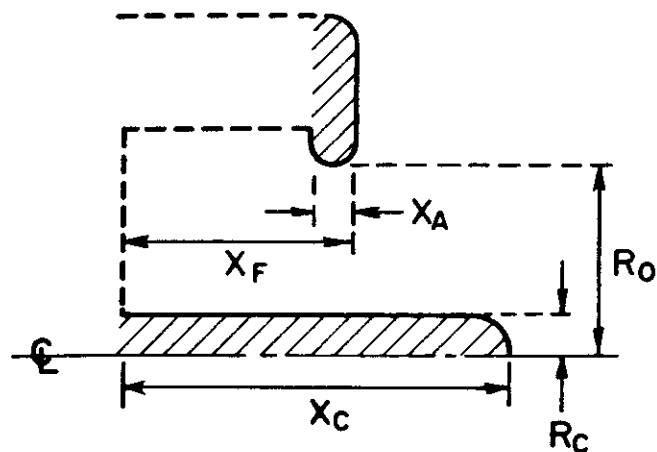
$\dot{m} = 6$ g/sec

FIGURE 2.5

voltage oscillations again decrease at high currents, as shown in fig 2.5, but spectra¹⁴ indicate that the arc operation is accompanied by considerable erosion of electrodes and insulators at these conditions.

Not all of the anode geometries in the VFP group operate satisfactorily. The long chamber configuration, VFP 11-1 produces an unexpected unstable discharge for all currents from 5 to 35 kA. This discharge is characterized by a pervasive 50 kHz oscillation of the terminal voltage which precludes any attempt to identify the cause and by severe pitting of the anode, possibly indicating localized current attachment at that surface. Magnetic probe records reveal no major asymmetries and suggest that the low frequency terminal voltage oscillation is due to an azimuthally symmetric oscillation of the current in the arc chamber. Subsequent tests showed that this unstable operation occurs for all chamber depths, X_d , greater than approximately 6 cm.

The effect of anode face position, X_f on J^* is shown in fig 2.6 for a fixed cathode length and anode orifice diameter. The onset current is seen to increase with increasing anode face position up to $X_f=10$ cm, beyond which the onset current appears to remain about 25 kA. Since the chamber depth, X_f-X_d , must be less than 10 cm to prevent low frequency oscillations, fig 2.6 implies that the anode axial extent must also increase for the more downstream anode face positions. Two important subsets of the data in fig. 2.6 show that this change in anode axial extent has no effect on J^* . Configurations VFP 8-3, 8-6 and 8-8 and configurations VFP 6-6 and 6-1 (data points at $X_f=8$ cm and $X_f=6$ cm, respectively) show that J^* only depends on the anode face position, regardless of the anode axial extent.



ONSET CURRENT FOR VARIOUS ANODES

FIGURE 2.6

Comparison of figs 2.3 and 2.6 reveals an important similarity between the effects of cathode length and anode face position on J^* . Figure 2.3 shows that for cathodes longer than the anode, J^* becomes asymptotic with cathode length; in fig 2.6, J^* is seen to increase with anode face position until the face is further downstream than the cathode tip, at which point a second asymptote is reached. This similarity suggests that J^* may be limited by the shorter of the two electrodes.

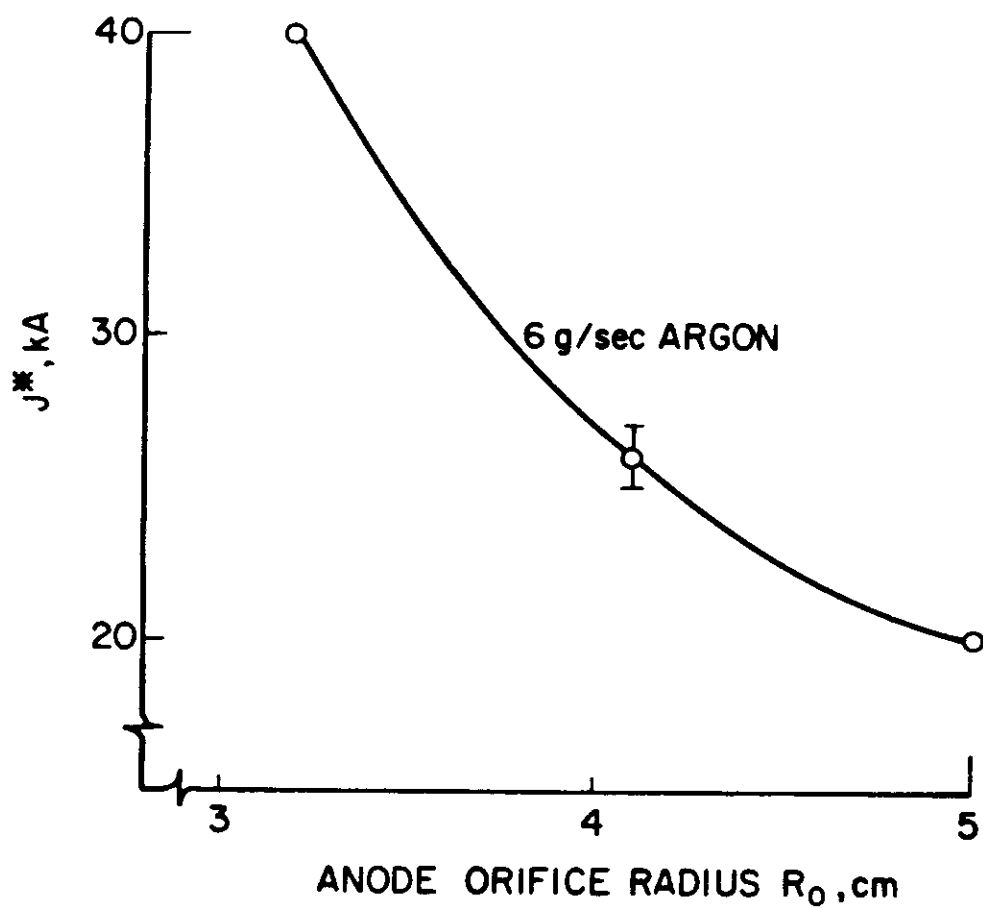
To investigate this possibility, the VCL series of experiments was performed. Configuration VCL 10 is identical to VFP 21-21, i.e. a 21-cm long anode butted against the chamber backplate, with a 10-cm long cathode. This configuration is shown as the most downstream data point in fig 2.6, X_f 21.6 cm. By increasing the cathode length to 20 cm (VCL 20), the onset current could be raised from 24.5 kA to 27 kA, indicating that the 25 kA asymptote in fig 2.6 is indeed related to the relatively short 10-cm cathode.

These data indicate that the shorter of the two electrodes does play an important role in establishing the onset current, and that further increases in J^* may be possible with yet longer electrodes. Although the physical basis for this increase has not been established, one possibility is that the decreased current density at the rear of the chamber, which may be expected to accompany the larger electrode surface areas, delays the onset of insulator ablation to higher total currents. Further, the more distributed acceleration zone should provide a more gradual and thereby more efficient plasma acceleration process.¹⁰

The investigation of the effect of the anode orifice was suggested by some early experiments in a much smaller glass vacuum vessel (0.45-m dia. by 0.76-m long).²⁶ During these tests, it was observed that for identical configurations, J^* is higher and the terminal voltage lower when the thruster is in the smaller tank. This effect was traced to a higher backpressure in the smaller tank, caused by the pre-discharge propellant injection transient. Postulating that a decreased anode orifice diameter may have the same effect by increasing the propellant mass density in the acceleration chamber, a series of experiments have since been conducted in which the anode orifice was varied in an otherwise identical arc chamber (VAO group of experiments).

The orifice radius is found to have a pronounced effect on J^* ,²⁷ as shown in fig 2.7. Decreasing the orifice radius from 5.1 cm to 3.2 cm increases J^* from 22.5 kA to nearly 40 kA. Since the average mass flux through the anode orifice increases with the smaller orifice radius, these data suggest a link between onset current and the propellant number density at some critical location in the arc chamber. It is interesting to speculate that since J^* is known to increase with the square root of the mass flow for a given configuration, i.e. $(J^*/\dot{m})^* \sim \text{constant}$, the physics underlying these two phenomena may be the same.

The large gains in the onset current realized by decreasing the anode orifice radius correspond directly to increases in specific impulse, since thrust decreases logarithmically with orifice radius. However, a net gain in specific impulse is indeed indicated, as discussed in the next section.



ONSET CURRENT J^*

FIGURE 2.7

E. SPECIFIC IMPULSE AND EFFICIENCY

In the high current MPD accelerator, the thrust is dominated by the electromagnetic body force of the crossed current and magnetic fields. Ignoring the electrothermal term, which can be 5 to 15% of the total thrust at high current, this thrust can be written

$$f_{EM} = b J^2 \quad (1)$$

where

$$b = \frac{\mu_0}{4\pi} (\ln R_A/R_C + K \phi_{TIP}^2) \quad (2)$$

and R_A and R_C are the current attachment radii at anode and cathode, respectively, K is a geometrical constant equal to 0.2 for the hemi-tip cathode, and ϕ_{TIP} is the fraction of current on the cathode tip.^{10,14}

To determine the values of R_A and ϕ_{TIP} for use with (2), the current distributions over the electrodes were measured using a small magnetic probe. An assumption of azimuthal symmetry allows conversion of these data into total current enclosed within a circle whose radius is the probe radial position with respect to the thruster centerline.

The data show that to a reasonable approximation, the current densities on the downstream face of the anode and on the cathode tip are uniform, from which values of R_A and ϕ_{TIP} are computed. These values are shown in Table 2 for all of the configurations examined except VFP 11-1, which had the low frequency oscillation problem.

Table II Calculated Thrust and Specific Impulse at J*;

$$\dot{m} = 6 \text{ g/sec}$$

Thruster Designation	R_A (cm)	ϕ	J^* (kA)	F^* (N)	I_{sp}^* (sec)
VFP 3-1	8.4+.16	0.1+.005	20+.5	87	1482
VFP 6-1	8.4	0.1	22.5	110	1871
VFP 6-6	8.4	0.1	23	115	1960
VFP 8-3	8.4	0.1	24	125	2125
VFP 8-6	8.4	0.1	24	125	2125
VFP 8-8	8.4	0.1	24	125	2125
VFP 11-6	8.4	0.1	25	136	2316

VCL 10 (VFP 21-21)	7.4	0.1	24.5	123	2095
VCL 20	7.4	0.05	27	149	2542

VAO 3	3.4	.13	39	194	3300
VAO 4	4.4	.17	26	103	1765
VAO 5	6.0	.26	20	74	1260

It is interesting to note that seven of the configurations in the VFP group have the same R_a and ϕ_{hp} and therefore the same thrust coefficient b . This is due to the fact that the same fraction of total current attaches to the anode face for these configurations, even those with large horizontal anode surface areas inside the chamber. The current streamlines of fig 2.8 show the surprising result that no current attaches over the horizontal surface of one of these anodes, VFP 11-6. This is not the case for the extremely long anode in the VFP 21-21 configuration. Figure 2.9 shows that nearly 60% of the current attaches on the axial surface of this anode, reducing the fraction of the total current on the outer face of the anode and hence the effective current attachment radius R_a .

Using the values for R_a and ϕ_{hp} in Table 2, the thrust and specific impulse, I_{sp}/mg , can be calculated at $J = J^*$. Once again, it should be stated that the electrothermal component is not included in these calculations since no quantitative information is available for these configurations. The resulting thrusts and specific impulses shown in Table 2 thus may be regarded as conservative estimates of the actual values. The configurations with the 4.1 and 3.2-cm anode orifice radii show pronounced reduction of R_a and hence of the thrust coefficient b with respect to the "benchmark" values. However, since the thrust is also dependent on J^2 , the maximum operating current overcomes the smaller b , yielding the highest implied value of I_{sp}^* of 3300 secs, 76% over the benchmark configuration.

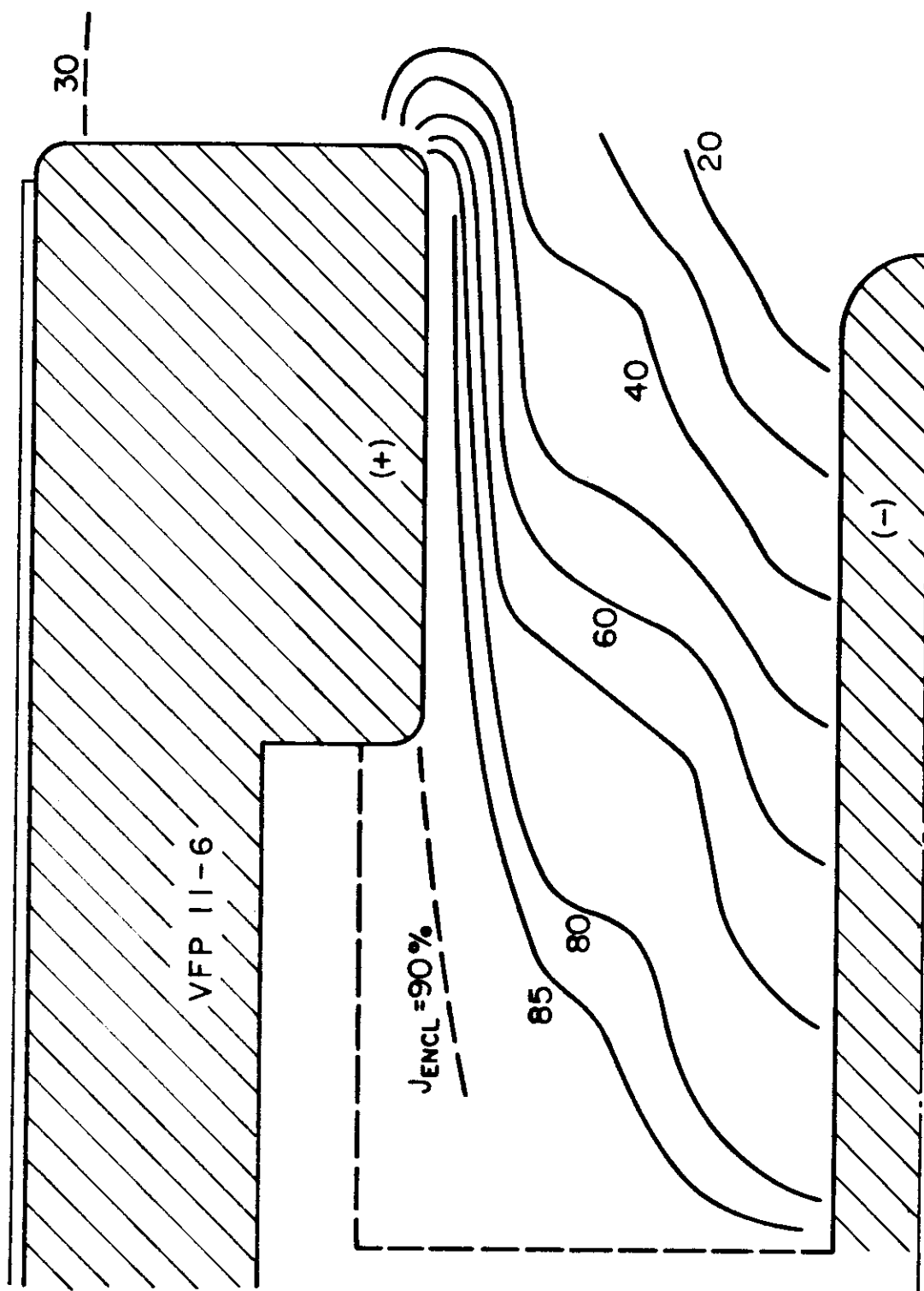
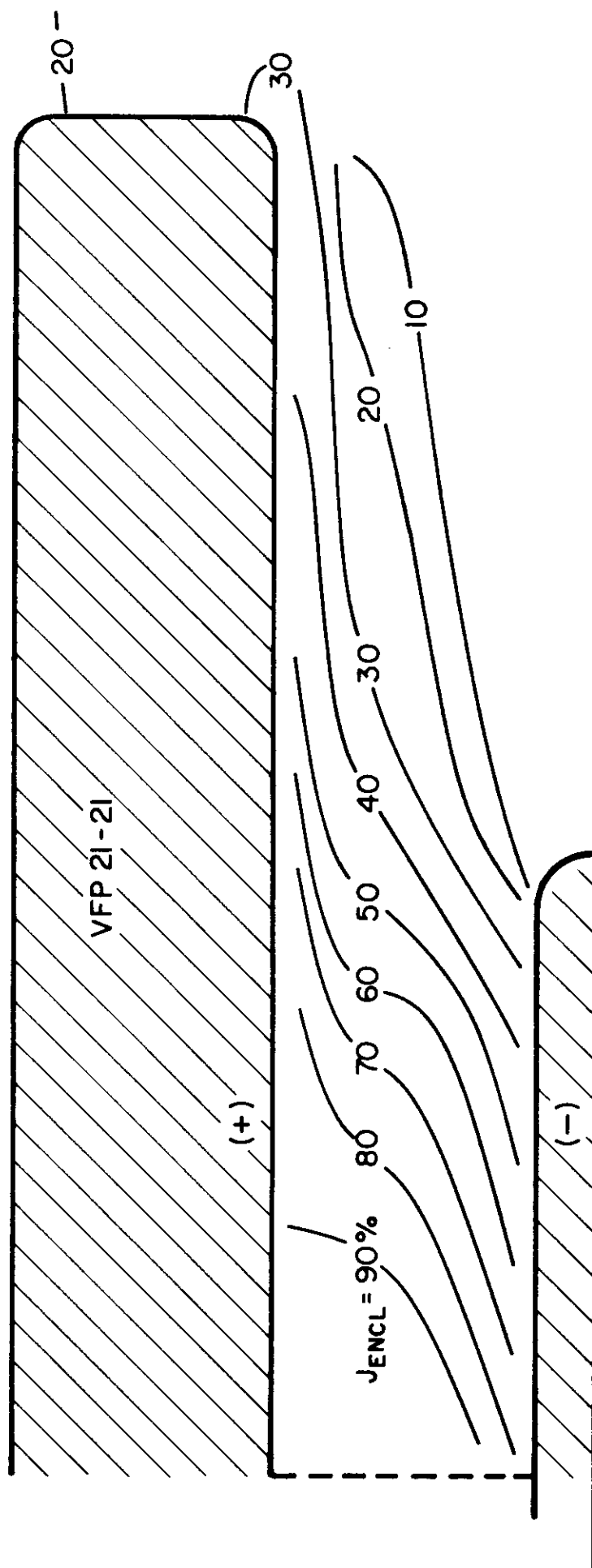


FIGURE 2.8



CURRENT CONTOURS
21.5 kA ; 6 g/sec

FIGURE 2.9
2-22

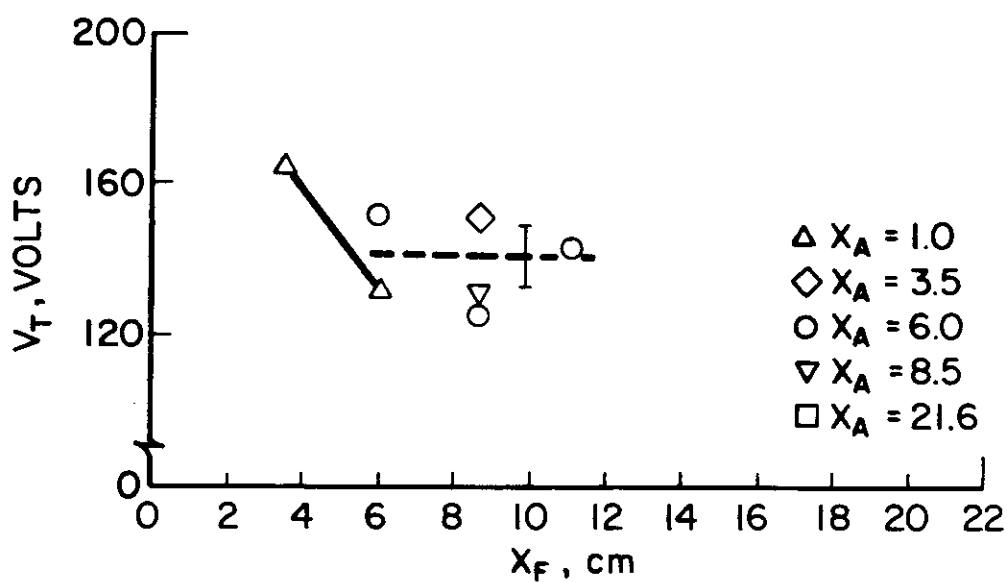
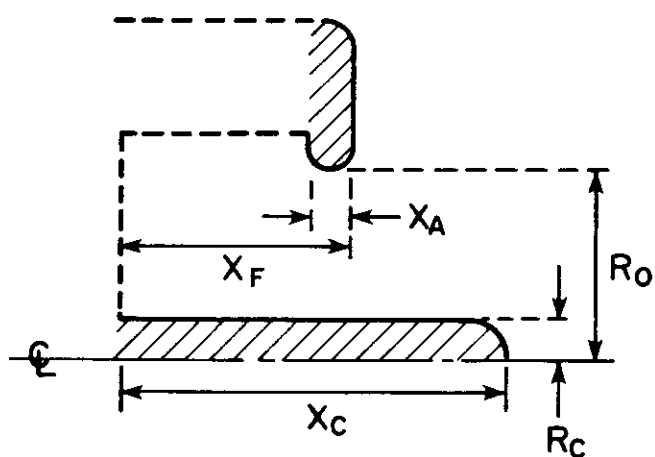
To check that the specific impulse does indeed increase with a higher J^* , the exhaust velocities have been measured for two geometries with the same R_a and A_p , but different specific impulses. One geometry is the benchmark configuration, VFP 6-1, with a J^* of 22.5 kA; the other is designated VFP 11-6, having a 6-cm long anode, an anode face at 11 cm and a J^* of 25 kA. For a thruster dominated by the electromagnetic thrust mechanism, this 11% increase in J^* above the benchmark value should correspond to a 23% increase in thrust and a similar increase in exhaust velocity or specific impulse at fixed mass flow. The exhaust velocity on the centerline is measured with a time-of-flight probe for these two configurations. Since the velocity profile is typically peaked about the centerline,²⁸ the centerline velocities will be greater than the bulk values. Thus, these measurements can only be used for a relative comparison of the configurations, based on the assumption of similar radial profiles of velocity.

The measurements indicate a centerline velocity of the benchmark configuration at $J^* = 22.5$ kA and $\dot{m} = 6$ g/sec of 27 ± 4 km/sec, and of 31.5 ± 4 km/sec for the VFP 11-6 configuration at its onset current of 25 kA and the same mass flow. Within the accuracy of the data, the 17% increase in the measured velocity agrees well with that calculated from the increase in J^* , supporting the premise that increases in J^* imply improvements in thruster performance.

The thrust efficiency, η_r , represents that fraction of the total input power, VJ , which is converted into useful thrust power, $\frac{F^2}{2m}$. For thruster configurations with identical thrust power, the relative efficiency is simply indicated by the terminal voltage. This comparison is possible for seven of the geometries tested, which have the same thrust coefficient, and thus produce the same thrust and thrust power at constant current and mass flow. Figure 2.10 shows the terminal voltages for these configurations at a current of 20 kA and a mass flow of 6 g/sec. The figure shows losses decreasing as the 1 cm thick anode is moved downstream. All other configurations represented in fig 2.10 have approximately the same losses, since the variations are within the 10% error bar, and so may be expected to have about the same thrust efficiency.

A significant difference in thrust efficiency is seen in the group of thruster configurations with varying anode orifice radius (VAO group). This can be seen most easily by plotting lines of constant power and constant calculated thrust on a graph of the voltage-current characteristics for the three configurations in this group, as shown in fig 2.11.

For a given thrust level, the best anode is one for which the input power or JV product is the smallest. Thus, since a constant power contour on this log plot is just a line of slope -1, it appears that of these three anodes, the configuration with the 3.2 cm orifice radius is the most efficient for almost all thrust levels. The optimum appears to vary weakly with current, with the smaller orifice anodes having a greater efficiency at the larger currents.

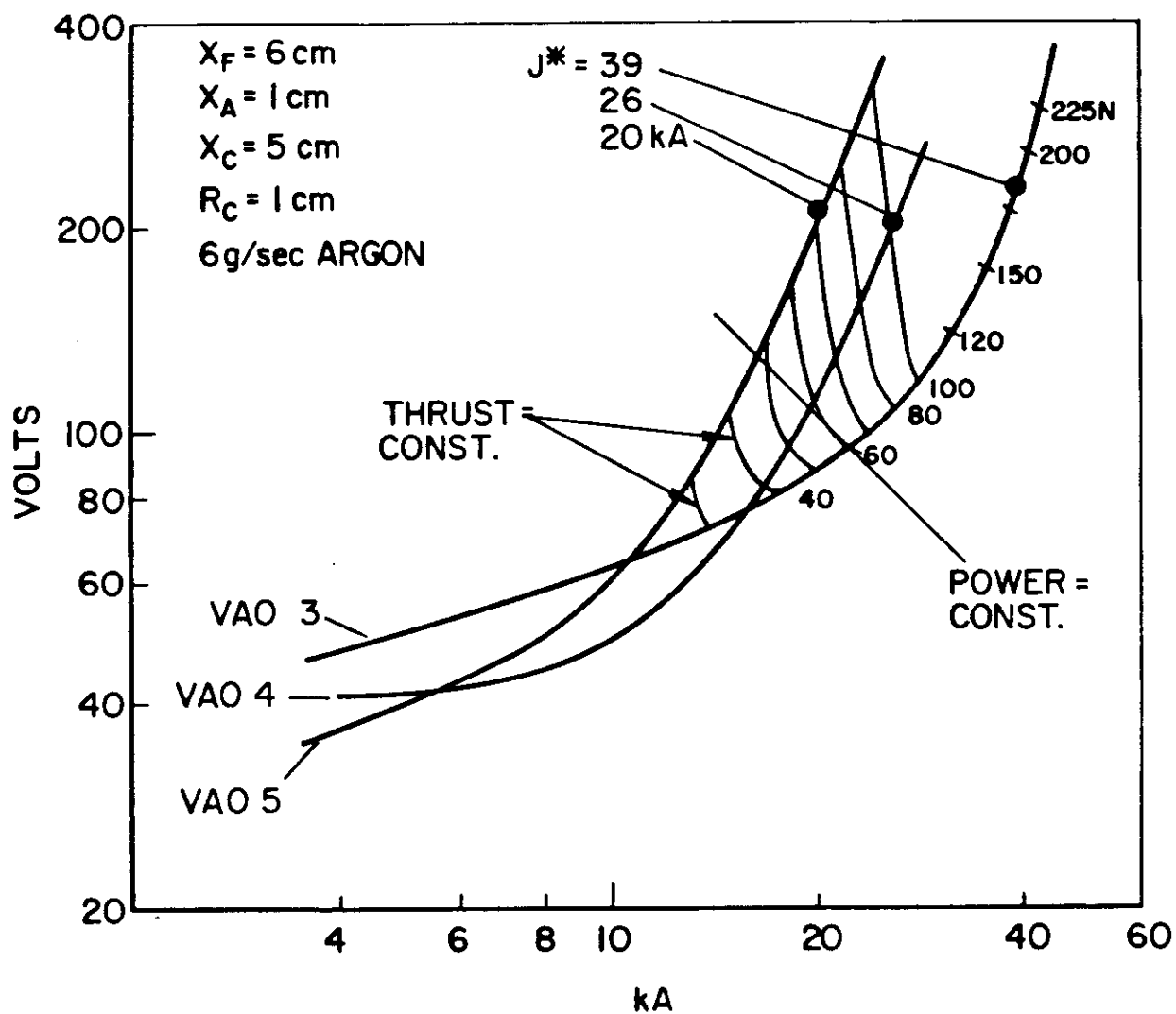


$J = 20 \text{ kA}, \dot{m} = 6 \text{ g/sec}$

$X_C = 10 \text{ cm}, R_0 = 5.1 \text{ cm}$

VOLTAGE FOR VARIOUS ANODES

FIGURE 2.10

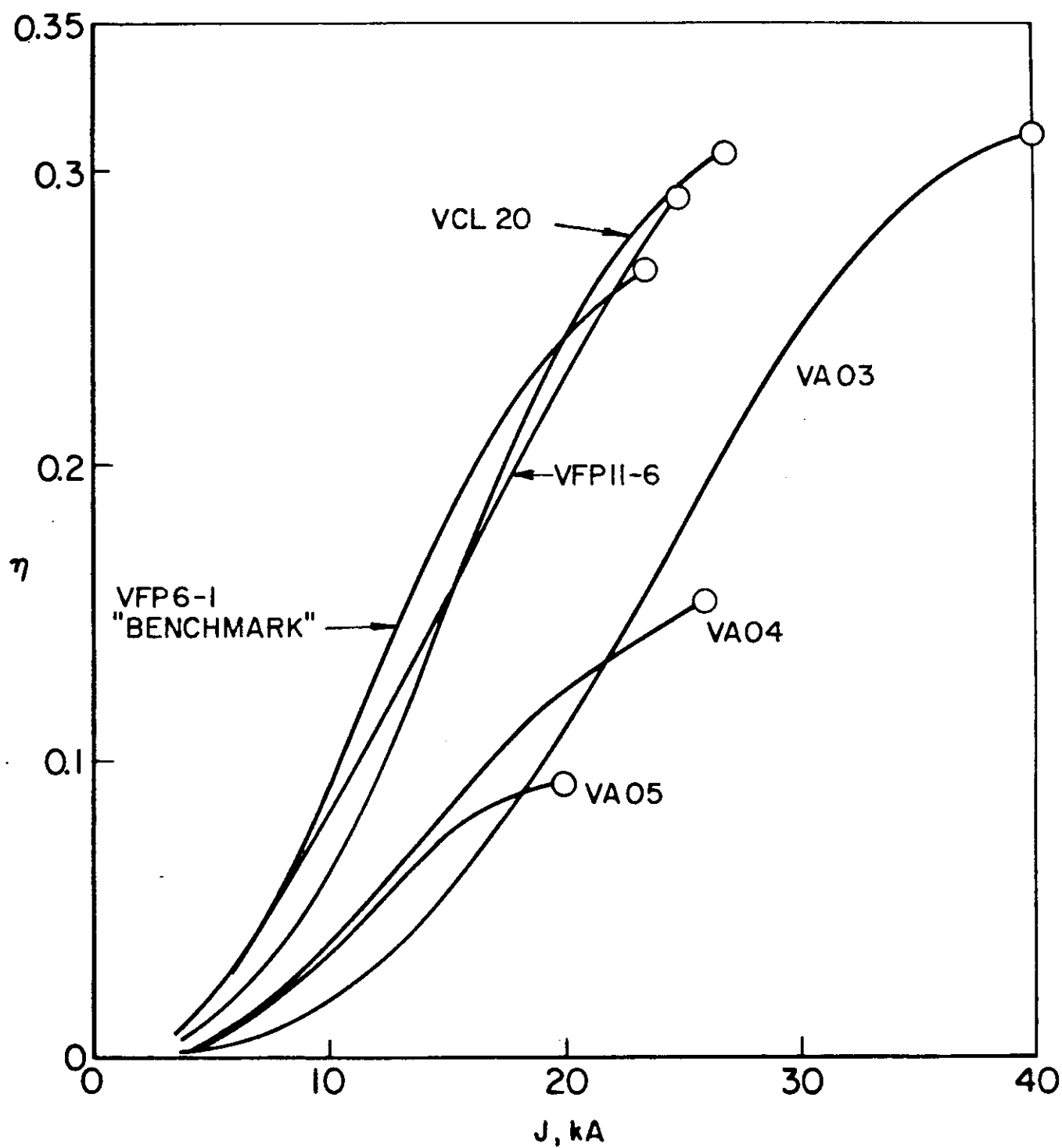


VARIOUS ANODE ORIFICE CHARACTERISTICS

FIGURE 2.11

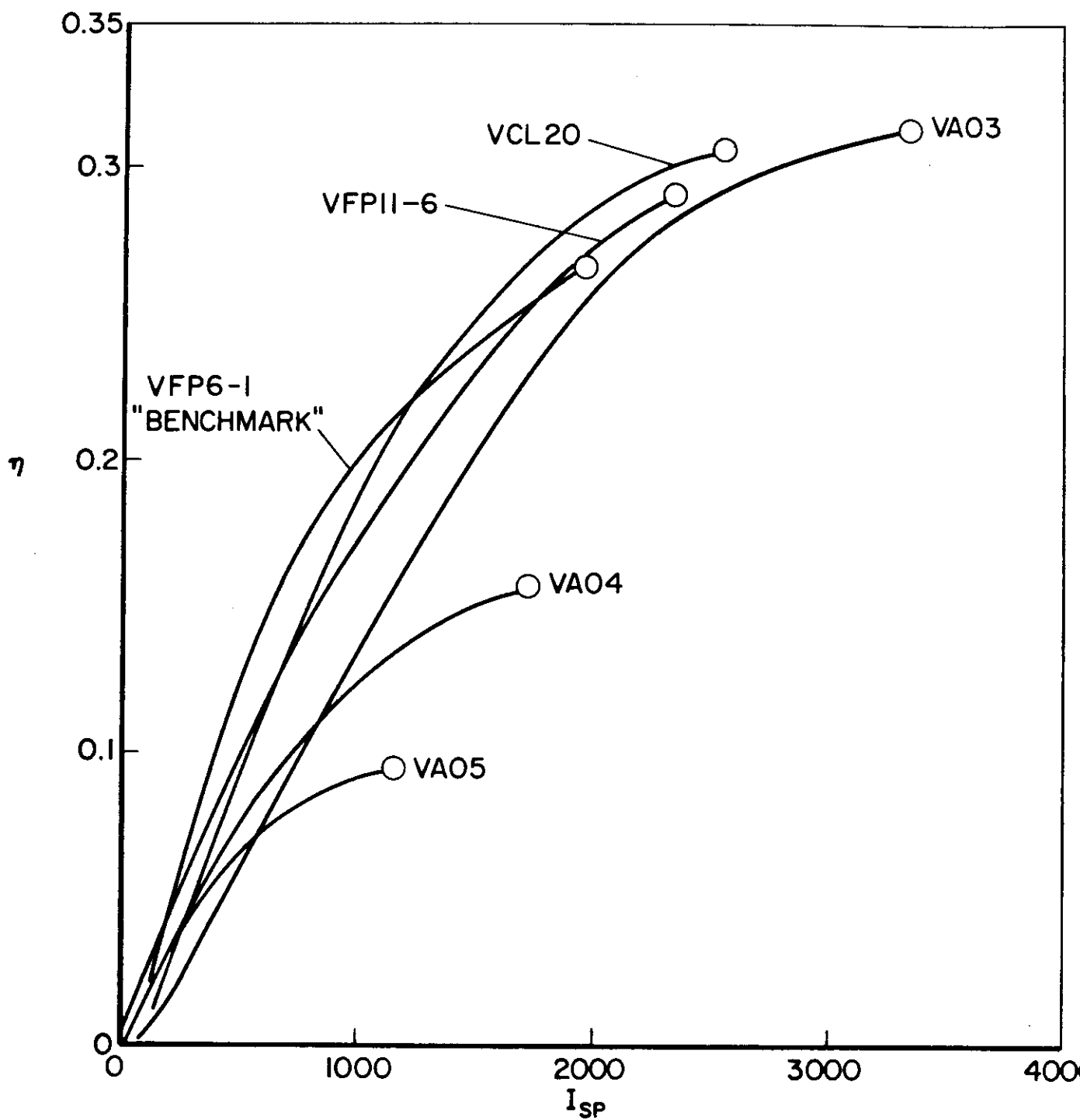
The greater efficiency of the VAO 3 thruster compared with thrusters of larger anode orifice (VAO 4 and VAO 5) is evident in fig 2.12, which shows curves of calculated thrust efficiency vs. current for six configurations, three of different anode orifice and three others with different length electrodes, all at an argon mass flow of 6 g/sec. Two configurations in this figure which have different length cathodes but all other dimensions the same are designated VFP 6-1 (the "benchmark" configuration with a 10 cm long cathode) and VAO 5 (a 5-cm long cathode). Comparison of the efficiencies of these two thrusters shows that the benchmark configuration has a higher efficiency at a given current and furthermore that it can be operated at a higher current before significant ablation occurs, i.e. it has a higher J^* , denoted in the figure by the circular data point. Other electrode configurations, e.g. an extended anode face (VFP 11-6), or a longer cathode and anode (VCL 20), show only small improvements over the benchmark efficiency curve, as long as the cathode is at least 10 cm long. Although the efficiency of the best of these (VCL20) is approximately that of the small anode orifice thruster (VAO 3), it does not provide the same high current operation and thus produces a lower specific impulse.

A more comprehensive summary of these configurations is shown in the efficiency-specific impulse characteristic of fig 2.13. Here, calculated performance for the same six thruster configurations show that for appropriately designed thrusters, an operating domain is



INFERRED THRUST EFFICIENCY η
 $\dot{m} = 6 \text{ g/sec}$

FIGURE 2-12



THRUST EFFICIENCY vs. SPECIFIC IMPULSE

FIGURE 2-13

prescribed which includes a thrust efficiency of 28% at a specific impulse of 2000 sec and 31% at 3300 sec.

F: SUMMARY

The geometry experiments summarized in fig 2.13 must be viewed with two considerations in mind. First, the configurations were selected to demonstrate the changes in apparent performance due to changes in the MPD electrode length and diameter, and were made separately. No attempt has been made to iterate the changes to couple the length and diameter effects.

The second consideration in evaluating fig 2.13 is that the performance figures have been calculated from magnetic field data, not measured directly. The figures were made from experimental data obtained at a fixed mass flow of 6 g/sec. It has been shown that the limiting specific impulse is consistent with $(J^2/\dot{m})^*$, but no such experimental confidence exists for the thrust efficiency.

Chapter 3

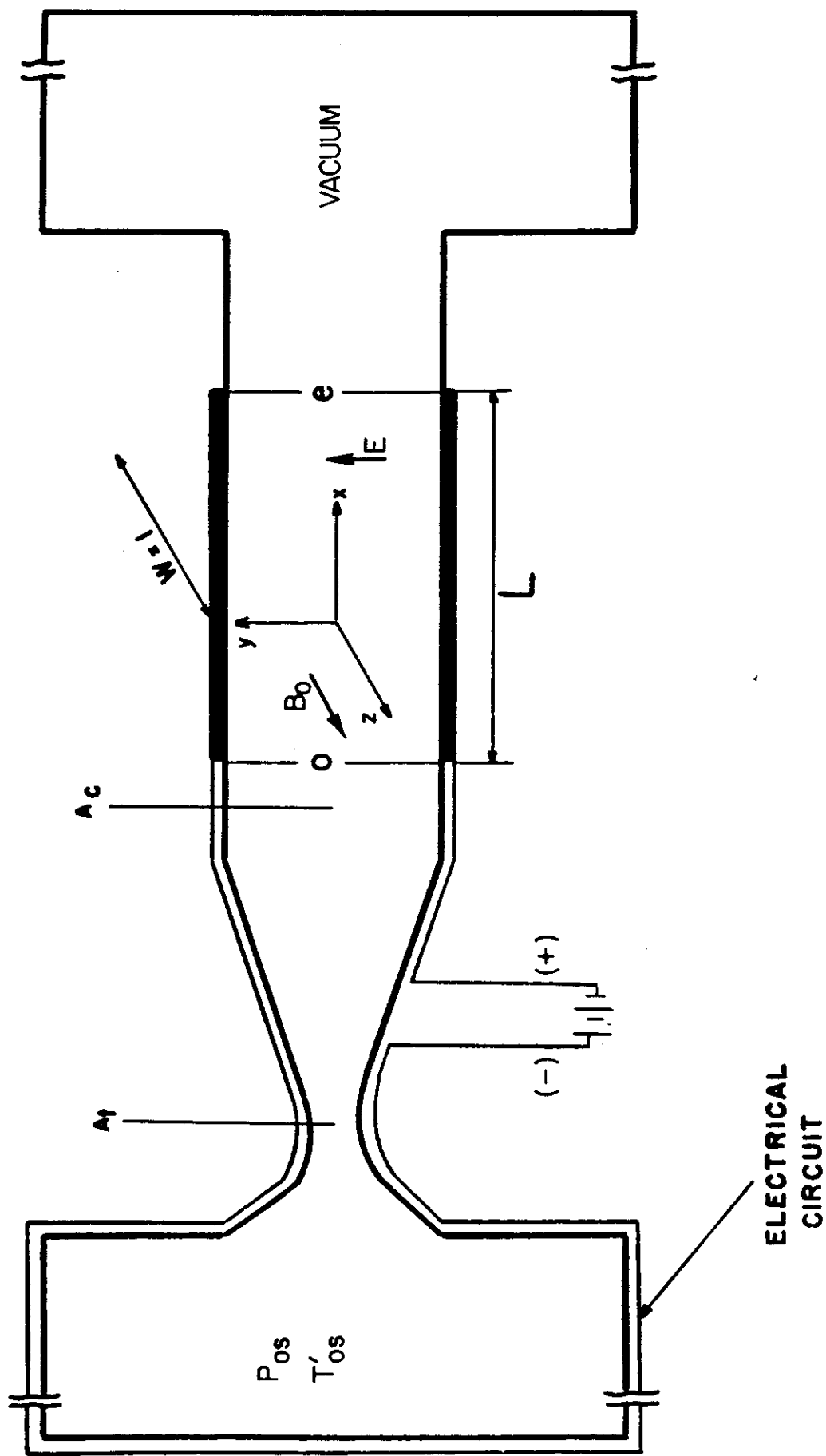
1-D, IDEAL GAS, STEADY, ACCELERATING, MPD CHANNEL FLOW

A: INTRODUCTION

This chapter presents a theoretical analysis of the MPD acceleration process. For the purposes of this analysis, certain idealizations and simplifications are made. The process is modeled as a one-dimensional channel free from viscous boundary layers and electrode sheaths; the model resembles flow along a streamtube in the thruster. After reviewing pertinent literature, the analysis is performed, and the results are used to illustrate the acceleration process and explain some experimental results.

Hughes and Young have analyzed 1-D ideal MPD channel flow for accelerating and decelerating body forces.\32\ Their presentation of this work is limited to Mach number profiles along the channel, and is a useful but brief introduction to the problem.

A more thorough analysis of 1-D accelerating monofluid has been performed by Martinache and Lam.\33\ Figure 3.1 shows the schematic of the model configuration and boundary conditions. Fluid enters a nozzle from a fixed stagnation temperature and pressure plenum. The fluid is presented to the left edge of the electrodes with a constant magnetic field imposed by the electrical circuit. The electric field generated by this circuit is uniform and perpendicular to the electrodes and exists only over the length L . Upon leaving the 1-D channel, the flow exhausts to



SCHEMATIC OF THE MARTINACHE MODEL

FIGURE 3.1

a vacuum. The key results of the Martinache analysis are the following:

- 1) The relation of the electric field to boundary conditions (p_{0s} , T_{0s} , B_0 , L) is established for accelerating flows in an algebraic form for an ideal monofluid.
- 2) The details of MPD choking phenomena are established in a constant area duct. Most importantly, the electric field is selected by the point where the flow passes through Mach 1.
- 3) No onset phenomena as observed in the laboratory are predicted by this ideal gas model.

In this chapter, the results of the 1-D analysis are presented in a form more readily compared to experiment. This form expresses the electric field as a function of ρ_{0u0} , T_{0s} , B_0 , and L , a small but significant difference from other analyses. The complexity of the dimensionless solutions is reduced from previous analyses in that these solutions are parameterized by a single group. This simplification permits a straight forward discussion of accelerating MPD channel flow. Also, chapter 3 is used as a basis for a real gas analysis in chapter 4.

B: THE 1-D ANALYSIS

The approximations used to develop the 1-D equations are the following:

- a) due to one dimensionality:
 - 1) field fringing is nil
 - 2) electrode sheaths are not considered
 - 3) assume the pressure tensor is isotropic
- b) simplifications:
 - 1) neglect viscous effects
 - 2) neglect heat transfer
 - 3) neglect ionization effects
 - 4) assume constant scalar conductivity

For these assumptions, the one dimensional, steady, constant area conservation equations are \34\:

$$\frac{d\rho u}{dx} = 0 \quad (1)$$

$$\rho u \frac{du}{dx} + \frac{dp}{dx} - j_y B_z = 0 \quad (2)$$

$$\rho u \frac{du^2/2}{dx} + \rho u \frac{dh}{dx} - E_y j_y = 0 \quad (3)$$

The magnetic field is related to current by one of Maxwell's equations:

$$j_y = -\frac{1}{\mu_0} \frac{dB_z}{dx} \quad (4)$$

The ideal equation of state is:

$$p = \rho RT \quad (5a)$$

$$h = c_p T \quad (5b)$$

where R is the gas constant and c_p is the specific heat at constant pressure. Ohm's law is:

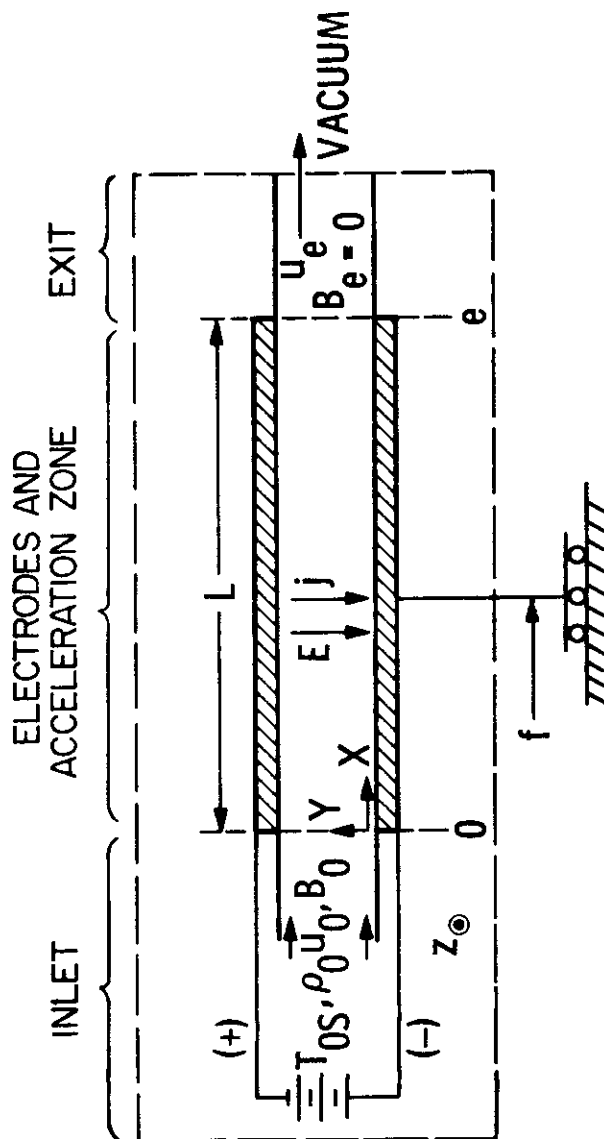
$$j_y = \sigma (E_y - u B_z) \quad (6)$$

Note that there are 7 equations ((1)-(6)) and 8 unknowns (ρ , u , p , T , h , j_y , B_z , and E_y) which pose an eigenvalue problem in finding the piecewise continuous functions $u(x)$, $B(x)$, etc.

Referring to the schematic in fig. 3.2, the boundary conditions are:

- 1) $\rho_0 u_0$ (considered given)
- 2) B_0 (considered given)
- 3) T_{05} (considered given)
- 4) L (considered given)
- 5) $B_z = 0$
- 6) $M_e \geq 1.0$ (exhaust to a vacuum)

The eigenvalue problem will be attacked in the following manner. Rather than finding $u(x)$, $B(x)$, $M(x)$, etc. and E directly, the problem will be mapped onto u - B coordinates. Then the electric field eigenvalue will be found, along with the functions $u(B)$, $M(B)$, etc. The final step will map these solutions back to spatial coordinates.



1-D MODEL SCHEMATIC

FIGURE 3-2

C: THE ELECTRIC FIELD RELATED TO MACH 1

In this section, the electric field is determined by considerations of the sonic point in the channel. This relationship permits the eigenvalue problem to be solved.

MPD channel flow can be considered as a conventional compressible flow with an external body force coupled to energy addition. The equations governing compressible flow have a singularity at Mach 1. In a converging-diverging nozzle, the area decrease causes the conventional flow to approach Mach 1, but the singularity permits a steady, sonic speed at only the throat. The diverging area then accelerates the Mach number away from 1. This conventional choking phenomena, with Mach 1 at the throat, requires a variable area channel. In contrast, a constant area MPD channel can have a subsonic inlet and a supersonic exit. In this case, heat addition accelerates the subsonic flow to Mach 1. At this point the balance of thermal to kinetic energy addition shifts, and the body force can accelerate the downstream flow to supersonic speeds. The precise balance of these two competing effects results in steady, accelerating flow through Mach 1 and also relates the electric field eigenvalue to boundary conditions.

The MPD "choking" phenomena is readily analysed on the u - B plane, and the development of an equation for du/dB is a convenient vehicle for this procedure. This equation is obtained by removing p , j , and h from equations (2) and (3) leaving u , B , F , and E . To remove p requires use of the combined first and second laws of thermodynamics:

$$Tds = dh - \frac{dp}{\rho} \quad (7)$$

and several auxilliary thermodynamic relationships derived from (7) and the ideal gas law, $p = \rho RT$:

$$\frac{1}{\rho T} \left(\frac{\partial p}{\partial s} \right)_\rho = \gamma(T) - 1 \quad (8a)$$

$$\left(\frac{\partial p}{\partial \rho} \right)_s \equiv a^2 ; a^2 = \gamma(T) \frac{p}{\rho} \quad (8b)$$

Note that relationships (8) hold for specific heats that are a function of temperature. Expanding dp over s and ρ in equation (7) and using (8) a relationship for dp , du , and dh is obtained:

$$dp = \frac{\gamma-1}{\gamma} \rho dh - \rho \frac{a^2}{\gamma u} du \quad (9)$$

Installing (4) and (9) in (2) and removing dx , a modified momentum equation is produced:

$$\rho u \left(1 - \frac{a^2}{\gamma u^2} \right) du + \frac{\gamma+1}{\gamma} \rho dh + \frac{B dB}{\mu_0} \quad (10)$$

Using (4) in (3) and again removing dx , the energy equation is:

$$dh + u du + \frac{E dB}{\mu_0 \rho u} = 0 \quad (11)$$

Removing dh by combining (10) and (11) and some rearrangement produces the desired relation for du/dB : /35/

$$\frac{du}{dB} = \frac{[(\gamma-1)E - \gamma u B] u}{\mu_0 \rho u (u^2 - a^2)} \quad (12)$$

To locate the electric field eigenvalue inside the constant area MPD channel, the sonic singularity requires:

$$E = \frac{\gamma}{\gamma-1} u^* B^* \quad (13)$$

where * denotes the sonic condition. Note that up to this point, the equations are valid for a gas with varying specific heats, $\gamma(T)$.

D: THE "COLD" INLET SIMPLIFICATION OF THE GOVERNING EQUATIONS

This section describes a simplification of the governing equations. This simplification in turn permits the solutions to be parameterized by a single group without loss of generality. First, explicit use of j_y and the spatial variable is avoided by substituting (4) in (2) and (3), followed by integration over x . After dropping the coordinate subscripts, the system can be written:

$$\rho u = \rho_0 u_0 \equiv F \quad (14)$$

$$Fu + p + \frac{B^2}{2\mu_0} = Fu_0 + p_0 + \frac{B_0^2}{2\mu_0} \quad (15)$$

$$Fu^2/2 + Fh + \frac{EB}{\mu_0} = Fu_0^2/2 + Fh_0 + \frac{EB_0}{\mu_0} \quad (16)$$

The equations for conservation of mass, momentum and energy ((14), (15), and (16)) can be made dimensionless by dividing by mass flux, magnetic pressure, and a characteristic velocity squared, respectively. The characteristic velocity is similar to the empricle J^2 / \dot{m} scale:

$$u_m = \frac{B_0^2}{2\mu_0 F} \quad (17)$$

The dimensionless conservation equations are:

$$\rho' u' = 1 \quad (18)$$

$$u' + p' + B'^2 = u'_0 + \beta_0 + 1 \quad (19)$$

$$u'^2_{/2} + h' + 2\xi B' = u'^2_{/2} + h'_0 + 2\xi \quad (20)$$

where $u' = u/U_m$; $\rho' = \frac{\rho U_m}{F}$; $p' = \frac{p/B_0^2}{2/\mu_0}$; $\beta_0 = \frac{p_0/B_0^2}{2/\mu_0}$;

$$h' = h/U_m^2 \quad ; \quad \xi = \frac{E}{U_m B_0} .$$

To remove h' from (20), the ideal gas law (5) and equation (18) can be combined to give:

$$\frac{\gamma}{\gamma-1} u' p' = h' \quad (21)$$

Substituting (21) in (20) gives:

$$\frac{u'^2}{2} + \frac{\gamma}{\gamma-1} u' p' + 2\xi B' = \frac{u'^2_0}{2} + h'_0 + 2\xi \quad (22)$$

According to reference 33, if 3 positive, real parameters such as u'_0 , h'_0 , and β_0 are given then the eigenvalue problem can be solved. This solution consists of the eigenvalue $\xi(u'_0, h'_0, \beta_0)$ and the piecewise-continuous, real functions $u'(B', u'_0, h'_0, \beta_0)$ and $p'(B', u'_0, h'_0, \beta_0)$ on the interval $0 \leq B' \leq 1$. Recognizing that these solutions with a "warm" inlet ($u'_0 > 0$, $h'_0 > 0$) have a "cold" point ($u'_c = 0$, $h'_c = 0$) in common permits the dimensionless family of solutions to be collapsed to depend on a single group.

The simpler family of solution is found by defining a "cold" inlet point, $u'_c = 0$. According to (22), this point lies outside the interval $0 \leq B' \leq 1$; i.e. $B'_c > 1$. Redefining variables such that the right bound becomes the "cold" inlet, $(u'_c, B'_c) \equiv (0, 1)$, will place the "warm" inlet somewhere inside the interval. With this redefinition, the governing equations (19) and (20) become:

$$u' + p' + B'^2 = 1 + \beta_0 \quad (23)$$

$$\frac{u'^2}{2} + h' + 2\xi(1 - B') = 0 \quad (24)$$

Here, the only parameter assumed given is β_0 .

E: THE DIMENSIONLESS ELECTRIC FIELD

Working in u-B coordinates, the "cold inlet" dimensionless electric field eigenvalue is found to be a function of only β_0 . To derive this function, it is convenient to first relate the Mach number to β_0 , B' , and ξ . The Mach number is defined as $M^2 \equiv u^2/a^2$ where a is the isentropic speed of sound. This speed of sound can be related to enthalpy:

$$h = \frac{a^2}{\gamma - 1} \quad (25a)$$

or in dimensionless parameters:

$$h' = \frac{a'^2}{\gamma - 1} \quad (25b)$$

Using the above definitions and (21) to eliminate p' and h' in (23) and (24), and then combining these to solve for M gives:

$$\frac{\frac{M^2}{2} + \frac{1}{\gamma - 1}}{(M + \frac{1}{\gamma M})^2} = \frac{2\xi(1 - B')}{(1 + \beta_0 - B'^2)^2} \quad (26)$$

The electric field is related to the choking point (*) by substituting $M=1$ into (26):

$$\xi(\beta_0, B'^*) = \frac{(1+\beta_0 - B'^*{}^2)^2}{(1-B'^*)} \quad (27)$$

The sonic point may occur at the exit and in this case, the electric field is found from (27) with $B'^*=0$:

$$\xi_T(\beta_0) = \frac{\gamma^2}{4(\gamma^2-1)} (1+\beta_0)^2 \quad (28)$$

The sonic point may also occur inside the duct; that is $0 < B'^* < 1$. This point is found by eliminating ξ , p' , h' , u' , and a' by combining (13), (21), (23), (24), (25), and $u'=a'$ to give:

$$B'^*{}^2 - \frac{4}{3} B'^* + \frac{1}{3} (1-\beta_0) = 0 \quad (29a)$$

with solutions:

$$B'^* = \frac{2 \pm \sqrt{1-3\beta_0}}{3} \quad (29b)$$

A simpler form of $\xi(B'^*, \beta_0)$ can be found by combining $u=a$, (13), (21), (23), and (25) to eliminate u' , a' , p' , and h' , but is restricted to $B'^* < 0$:

$$\xi(\beta_0, B'^*) = \frac{\gamma^2}{\gamma^2-1} [(1+\beta_0)B'^* - B'^*{}^3] \quad (30)$$

Substituting (29b) with the minus sign in (30) provides ξ_m :

$$\xi_m = \frac{\gamma^2}{\gamma^2-1} \left[(1+\beta_0) \left\{ \frac{2-\sqrt{1-3\beta_0}}{3} \right\} - \left\{ \frac{2-\sqrt{1-3\beta_0}}{3} \right\}^3 \right] \quad (31)$$

Substituting (29b) with the plus sign in (30) provides ξ_p :

$$\xi_p(\beta_0) = \frac{\gamma^2}{\gamma^2-1} \left[(1+\beta_0) \left\{ \frac{2+\sqrt{1-3\beta_0}}{3} \right\} - \left\{ \frac{2+\sqrt{1-3\beta_0}}{3} \right\}^3 \right] \quad (32)$$

Figure 3.3 shows $\xi_T(\beta_0)$, $\xi_m(\beta_0)$ and $\xi_p(\beta_0)$ plotted vs. $1/\beta_0$ for graphical clarity. The point of intersection of ξ_T and ξ_m can be found by letting $v = \sqrt{1-3\beta_0}$, equating (28)=(31) and simplifying. The resulting polynomial is:

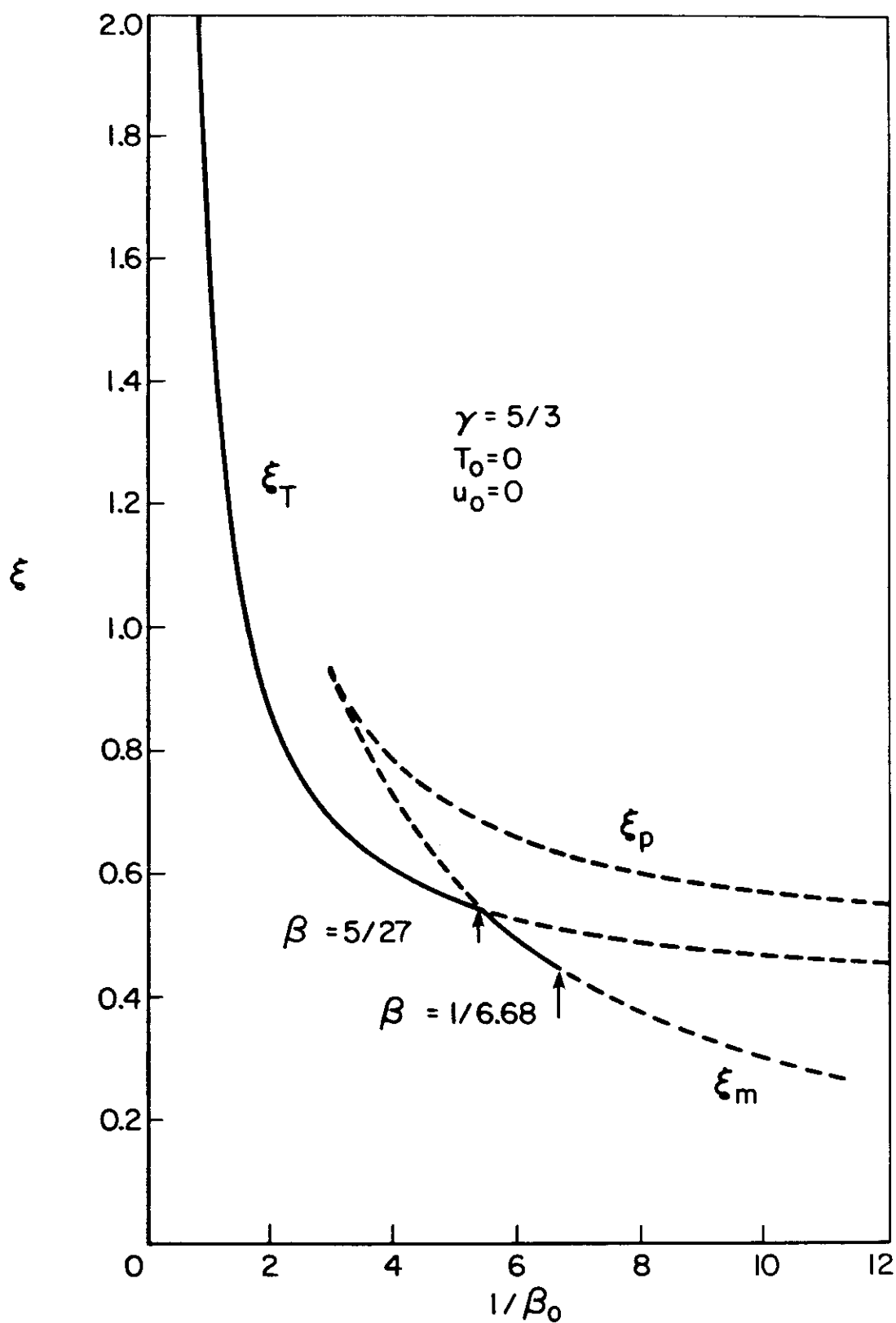
$$3v^4 + 16v^3 + 24v^2 - 16 = 0 \quad (33)$$

One root of (31) is $v=2/3$, which is $\beta_0=5/27$, the point of intersection. The other three roots are $v=-2$, which are complex β_0 values.

The dashed portions of the curves in fig. 3.3 are to be discarded for the following reasons. First, with $\xi_m(\beta_0)$ for $\beta_0 < 1/6.68$, the back EMF may be larger than the electric field, causing the flow to decelerate. The point $\beta_0=1/6.68$ has been located numerically and is discussed further in the following sections. Using any other dashed $\xi(\beta_0)$ curve will not produce piecewise-continuous, real Mach number profiles (from equ (26)) in the channel.

To summarize, the ξ values that give piecewise-continuous, real Mach number solutions for accelerating flow over $0 < B' < 1$, and the related electric field values are:

$$\xi = \begin{cases} \xi_T(\beta_0) ; \beta_0 \geq 5/27 \\ \xi_m(\beta_0) ; 1/6.68 \leq \beta_0 < 5/27 \end{cases} \quad (34)$$



DIMENSIONLESS ELECTRIC FIELD (IDEAL GAS)

FIGURE 3.3

F: ACCELERATING FLOWS ON THE u-B PLANE

Three cases of MPD flows with energy addition are discussed on the u-B plane in this section. To do so an expression for velocity can be developed. Using (21) in equations (22) and (23) and then combining these to eliminate p' produces:

$$u'^2 - 2 \frac{\gamma}{\gamma+1} (1+\beta_0 - B'^2) u' + \frac{4(\gamma-1)}{(\gamma+1)} (1-B') \xi = 0 \quad (35a)$$

which has solutions:

$$u'_{\pm}(\beta_0, B') = \frac{\gamma}{\gamma+1} \left[(1+\beta_0 - B'^2) \pm \left\{ (1+\beta_0 - B'^2)^2 - \frac{4(\gamma^2-1)}{\gamma^2} (1-B') \xi \right\}^{1/2} \right] \quad (35b)$$

By substituting (21) and $u'^* = a'^*$ into (23), the locus of sonic velocities is found:

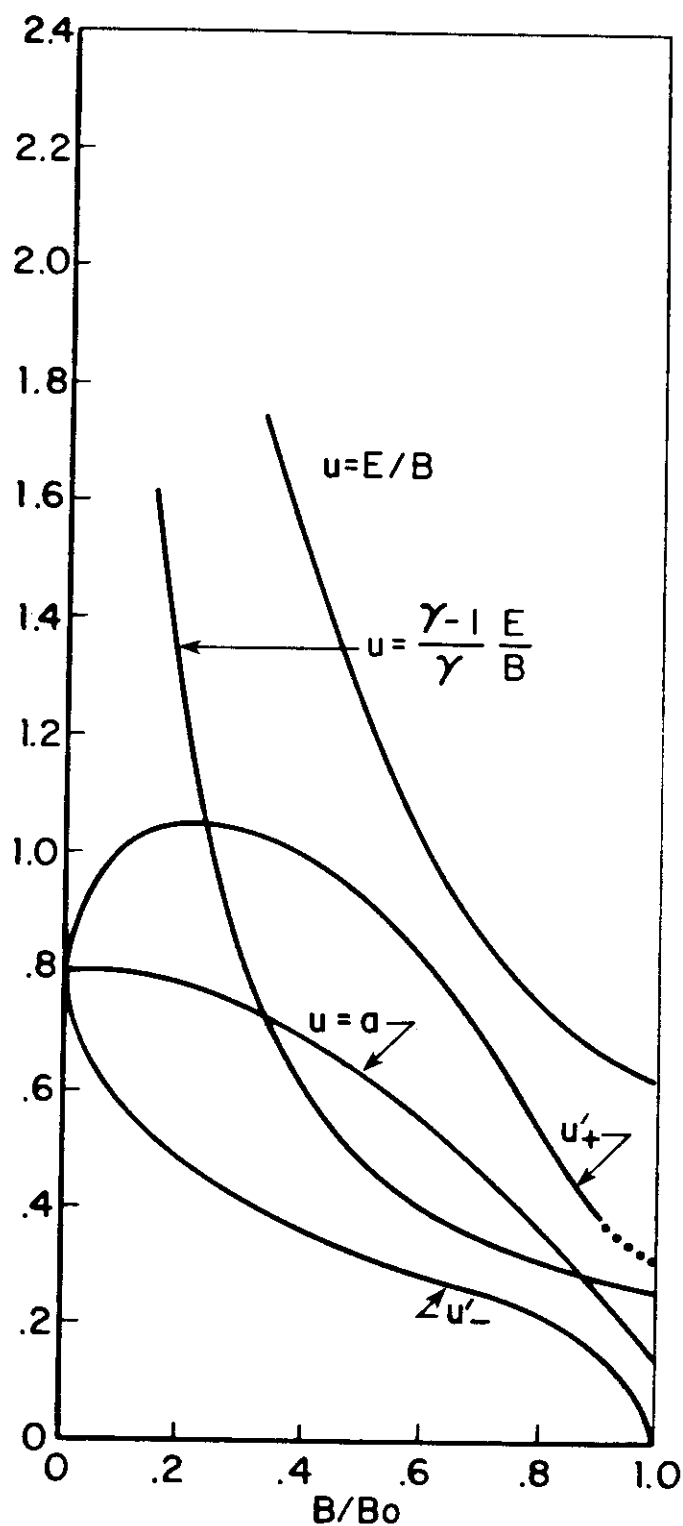
$$a'^* = \frac{\gamma}{\gamma+1} (1+\beta_0 - B'^2) \quad (34)$$

Equation (36) is the first term in (35b) and this means u'_+ denotes supersonic velocities and u'_- denotes subsonic velocities. The two electric field functions are given designations according to the predominant mode of acceleration, thermal or magnetic. The three cases of velocity profiles to be discussed are: the electrothermal mode, the electromagnetic mode, and the transition mode.

1) Electrothermal Acceleration Mode ($\beta_0 > 5/27$)

Figure 3.4 shows velocity profiles for $\beta_0 = 1/4$, as well as several other curves which can be used to further describe the acceleration process. The curve labeled u'_- is the subsonic velocity profile, and meets u'_+ at the exit, where the Mach number is 1. Since thermal effects drive the Mach number toward

$$u' = \left(\frac{\frac{u}{B_0^2}}{2\mu_0 \rho u} \right)$$



IDEAL GAS, ELECTROTHERMAL MODE
ACCELERATION PROFILE, $\beta_0 = 1/4$, $\gamma = 5/3$

FIGURE 3.4

1, this case has been designated the "electrothermal" mode.

Any segment of $u'_-(\beta_0, B')$ extending from $B'=0$ to some $B'<1$ represents a subsonic velocity profile with a non-zero inlet speed and temperature. Similarly for $u'_+(\beta_0, B')$, a segment extending from $B'=0$ to some $B'<B'_{T=0}$ represents a supersonic velocity profile with a non-zero inlet speed and temperature. The inlet location is bounded by $B'_{T=0}$, the point where temperature is zero on the u'_+ curve. This point, $B'_{T=0}$, is calculated in appendix 1 as a function of β_0 .

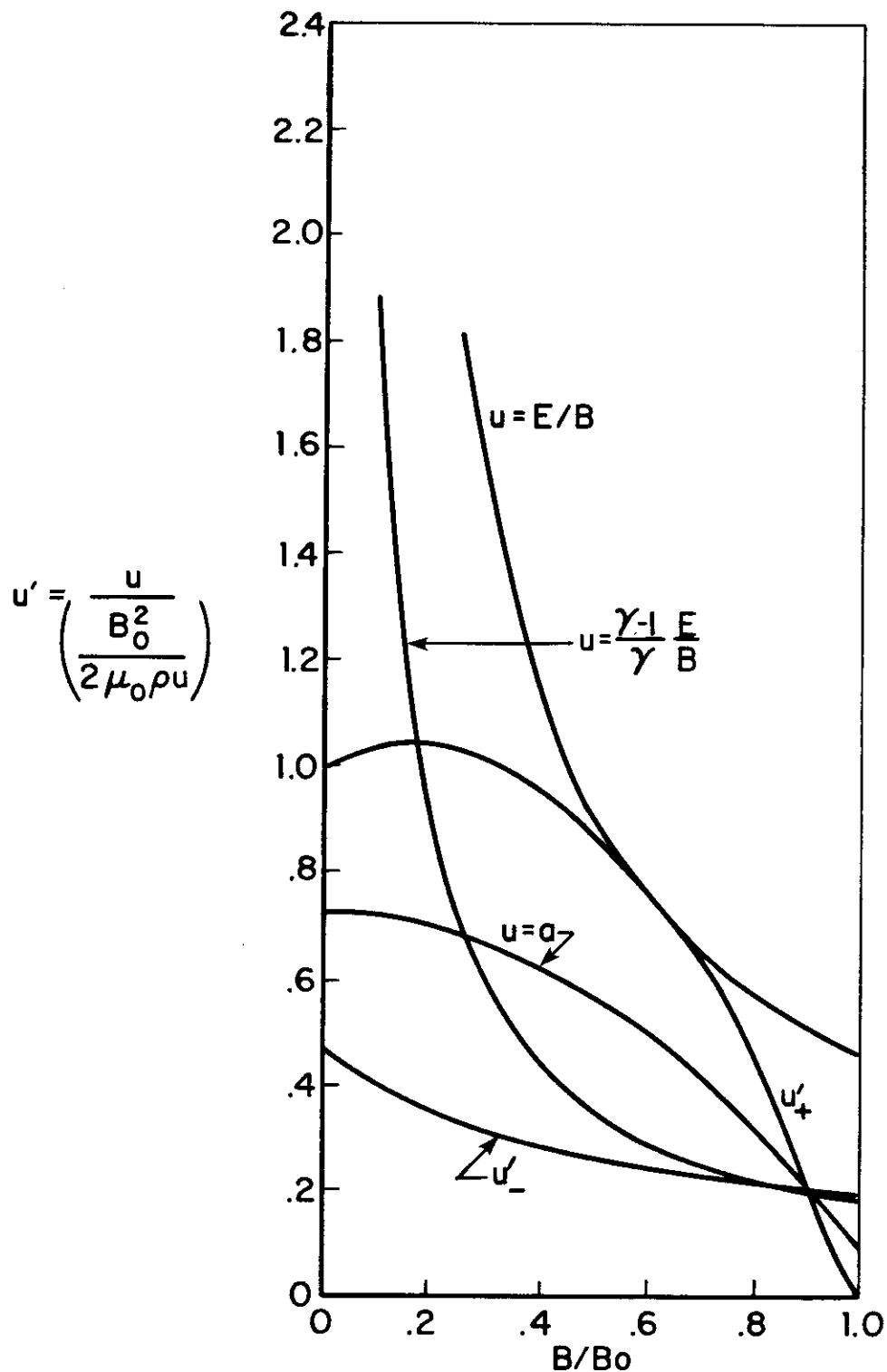
Along the curve $u=a$, the denominator of du/dB is zero. Accordingly, note that the slope of u' is infinite where $u'_-=u'_+=a'$. Along the hyperbola $u=\frac{\gamma-1}{\gamma} E/B$, the numerator of du/dB is zero. Note that the slope of u'_+ changes sign where the hyperbola crosses this curve.

Finally, the curve $u=E/B$ can be compared to u'_+ or u'_- to assess the back EMF.

2) Electromagnetic Acceleration Mode ($1/6.68 < \beta_0 < 5/27$)

Figure 3.5 shows the u - B profile for $\beta_0=1/6.68$. Note that the exit Mach number is either supersonic or subsonic. Since the magnetic body force drives the Mach number away from 1, this case is designated the "electromagnetic" mode.

The point where curves u'_+ , u'_- , $u=a$, and $u=\frac{\gamma-1}{\gamma} E/B$ intersect is of singular importance. At this point both the denominator ($u=a$) and the numerator ($u=\frac{\gamma-1}{\gamma} E/B$) of du/dB are zero. This point is also used to select the electric field eigenvalue. Note that velocity profiles with subsonic inlet speeds can be smoothly accelerated through the sonic point.



IDEAL GAS, ELECTROMAGNETIC MODE
 ACCELERATION PROFILE, $\beta_0 = 1/6.68$, $\gamma = 5/3$

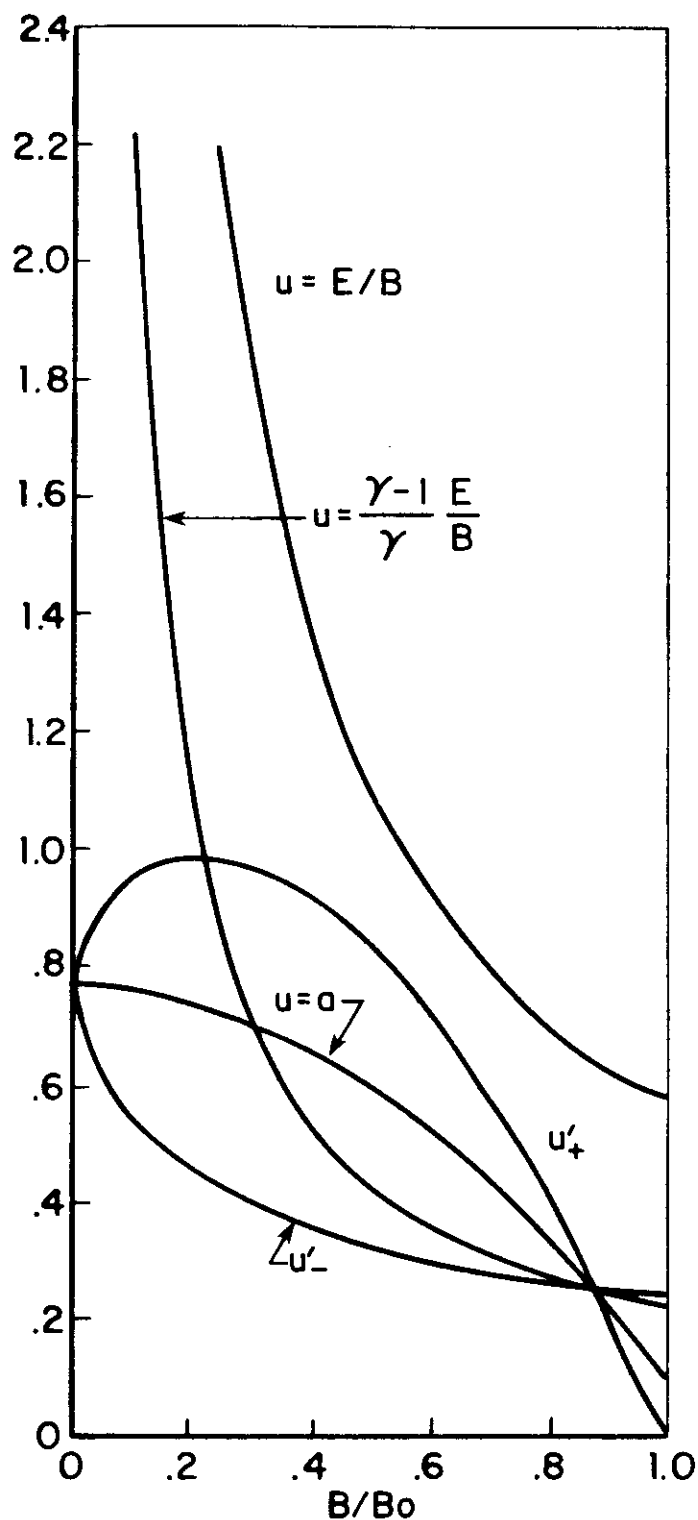
FIGURE 3.5

Although this figure shows the limiting case $\beta_o = 1/6.68$, the shapes of u'_- and u'_+ are typical of the electromagnetic mode acceleration. But in this limiting case, the supersonic profile is tangent to $u=E/B$ indicating that the back EMF equals the electric field at this point ($E-uB=0$). If $\beta_o < 1/6.68$, then the back EMF can be larger than the electric field and current will reverse along some portion of the channel.

3) Transition Mode ($\beta_o = 5/27$)

Figure 3.6 shows that the velocity is sonic at two locations. In this case, a typical velocity profile might consist of a subsonic inlet, smooth acceleration through Mach 1, a shock dropping velocity from u'_+ to u'_- , and final acceleration along u'_- to the exit. Current density, which is $\sigma(E-uB)$, increases across the shock. The position of the shock is adjusted to conduct a given current over a given length.

$$u' = \left(\frac{u}{\frac{B_0^2}{2\mu_0\rho u}} \right)$$



IDEAL GAS, TRANSITION MODE
ACCELERATION PROFILE, $\beta_0 = 5/27$, $\gamma = 5/3$

FIGURE 3.6

G: THE MAGNETIC REYNOLDS NUMBER

In this section, velocity profiles on the u-B plane are mapped onto the spatial variable. Given appropriate inlet conditions, the length of the acceleration zone can be computed. Rearranging Ohm's law (6) and applying (4):

$$\int_0^{B_0} \frac{dB}{\mu_0 \sigma (E - uB)} = \int_0^L dx = L \quad (37)$$

Assuming, for the ideal gas model, constant conductivity, and using dimensionless quantities, (34), and (35b), the integral can be written

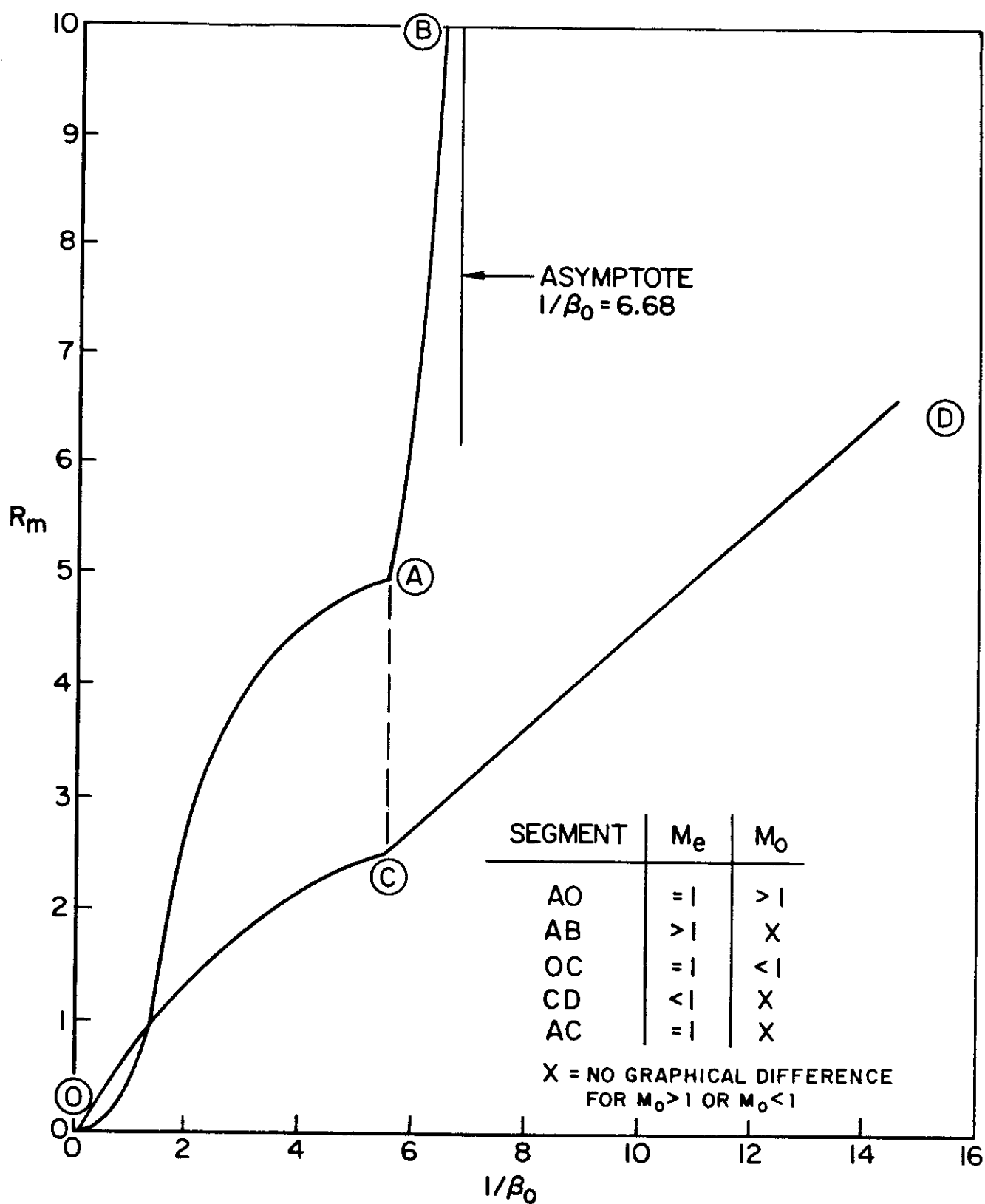
$$\int_0^{B'_{IN}} \frac{dB'}{\xi - u' B'} = \mu_0 \sigma U_m L \quad (38)$$

The right hand is defined as the magnetic Reynolds number, R_m :

$$R_m = \mu_0 \sigma U_m L \quad (39)$$

The upper bound is the magnetic field at the inlet. For subsonic inlets with $T_0=0$, $B'_{IN}=1$, for supersonic inlets with $T_0=0$, $B'_{IN} = B'_{T=0}$.

Equation (38) is computed numerically and is expressed as a function of β_0 , as shown in fig. 3.7. There are 8 segments of $R_m(\beta_0)$ although only 5 segments are graphically distinct. The $R_m(\beta_0)$ segments are constructed using ξ given by (34) and using various segments of $u'_\pm(B', \beta_0)$ indicated by Mach number in table 3.1.



MAGNETIC REYNOLDS NUMBER vs β_0
- IDEAL GAS, $\gamma = 5/3$

FIGURE 3.7

	$M_o < 1$	$M_o > 1$	
$M_e = 1$	OC	OA	electrothermal, $\beta_o > 5/27$
$M_e = 1$	AC	AC~	transition, $\beta_o = 5/27$
$M_e > 1$	AB	AB~	electromagnetic, $1/6.68 \leq \beta_o < 5/27$
$M_e < 1$	CD	CD~	electromagnetic, $\beta_o < 5/27$

Note: Segments AB and AB~ cannot be graphically distinguished in fig. 3.7. This is also true for (CD, CD~) and (AB, AB~).

Segments of $Rm(\beta_o)$ - See fig. 3.7

TABLE 3.1

For instance segment AB has a subsonic inlet and a supersonic exhaust and so u'_- would be used for the subsonic upstream portion and u'_+ for the supersonic downstream portion. This profile can be seen in fig. 3.6.

Note that Rm approaches an asymptote at $\beta_o = 1/6.68$. The infinite magnetic Reynolds number occurs when the denominator of the integrand (38) is zero.

The transition mode (segment AC) also deserves special attention. On this curve, the position of the shock is related to the average velocity and current density. Thus for a fixed electrode length, both Rm and the position of the shock are controlled by Um . In a 2-D geometry, the current conducting region may blow downstream of the electrodes, and the shock need

not occur.

Certainly, the assumption of constant conductivity affects the theoretical current distribution. Also the exclusion of the ionization process from the state equation must distort the enthalpy, pressure, and therefore velocity and current profiles. These approximations may be reasonable in cases where small amounts of specific energy (small with respect to the ionization potential) are added to the flow. Otherwise, the distortions in the relationship between electrode length and exhaust velocity, temperature, etc. must be present. However, the u-B profiles are not directly affected, and for this reason the constant conductivity solutions can be considered to be illustrative of the acceleration process. That is, regardless of the conductivity formulation, the 1-D channel will exhibit electrothermal, electromagnetic, and transition modes of acceleration.

H: ELECTRIC FIELD CHARACTERISTIC FOR FIXED LENGTH ELECTRODES

In this section, the dimensionless solutions are converted to a dimensional electric field characteristic for comparison with experiment. Given the first four boundary conditions, specified in section B, the electric field can be computed. The process is simplest for zero stagnation temperatures as curves 3.7 and 3.3 can be used directly. The procedure is to first compute R_m , locate β_0 from fig. 3.7, and then look up E on fig. 3.3. Figure 3.8 shows the characteristic OCAB for the above boundary conditions, and two other curves OA and CD. To coordinate this figure with the previous ones, the point designations and joining segments correspond to those in fig 3.7. Along OCAB, the acceleration process is in the electrothermal mode on OC, the transition mode on CA, and the electromagnetic mode on AB. Point B is drawn at an arrowhead since there is no upper bound to either B_0 or E values in this model.

For B_0 values typical of laboratory operation ($B_0 \sim 0.2$ T), the exit temperature is very large ($T_e > 200E3$ °K) since ionization is not considered in this ideal gas analysis. Correspondingly large and unrealistic values of pressure are also computed at the exit.

Segment OA is included in fig. 3.8 to show the effect of supersonic over subsonic inlet Mach numbers on the electric field. On OA, the inlet temperature is zero, but the velocity and stagnation temperature are larger than zero. The Mach number and inlet pressure are related to B , F , T_{0s} , and L by the arc.

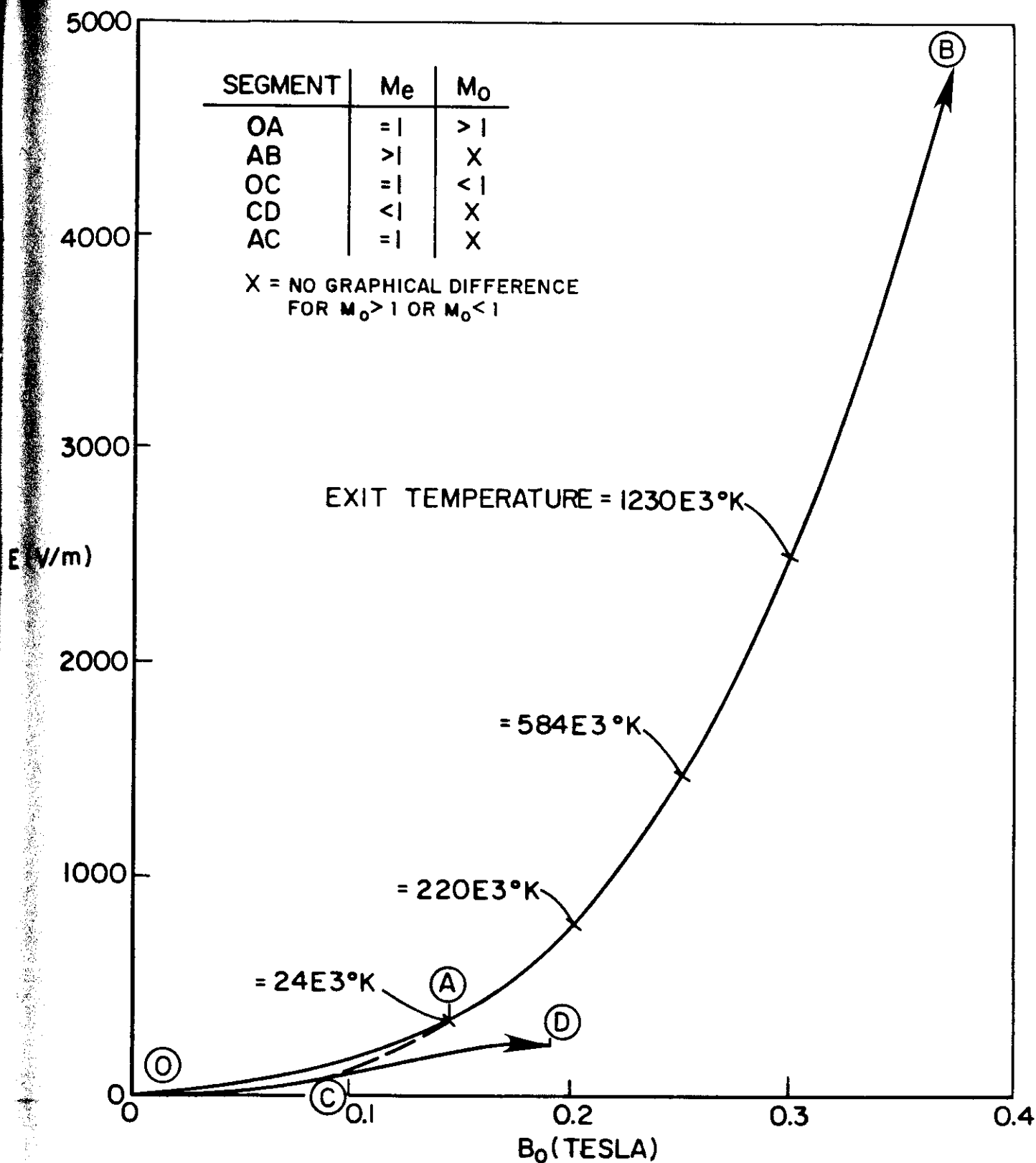


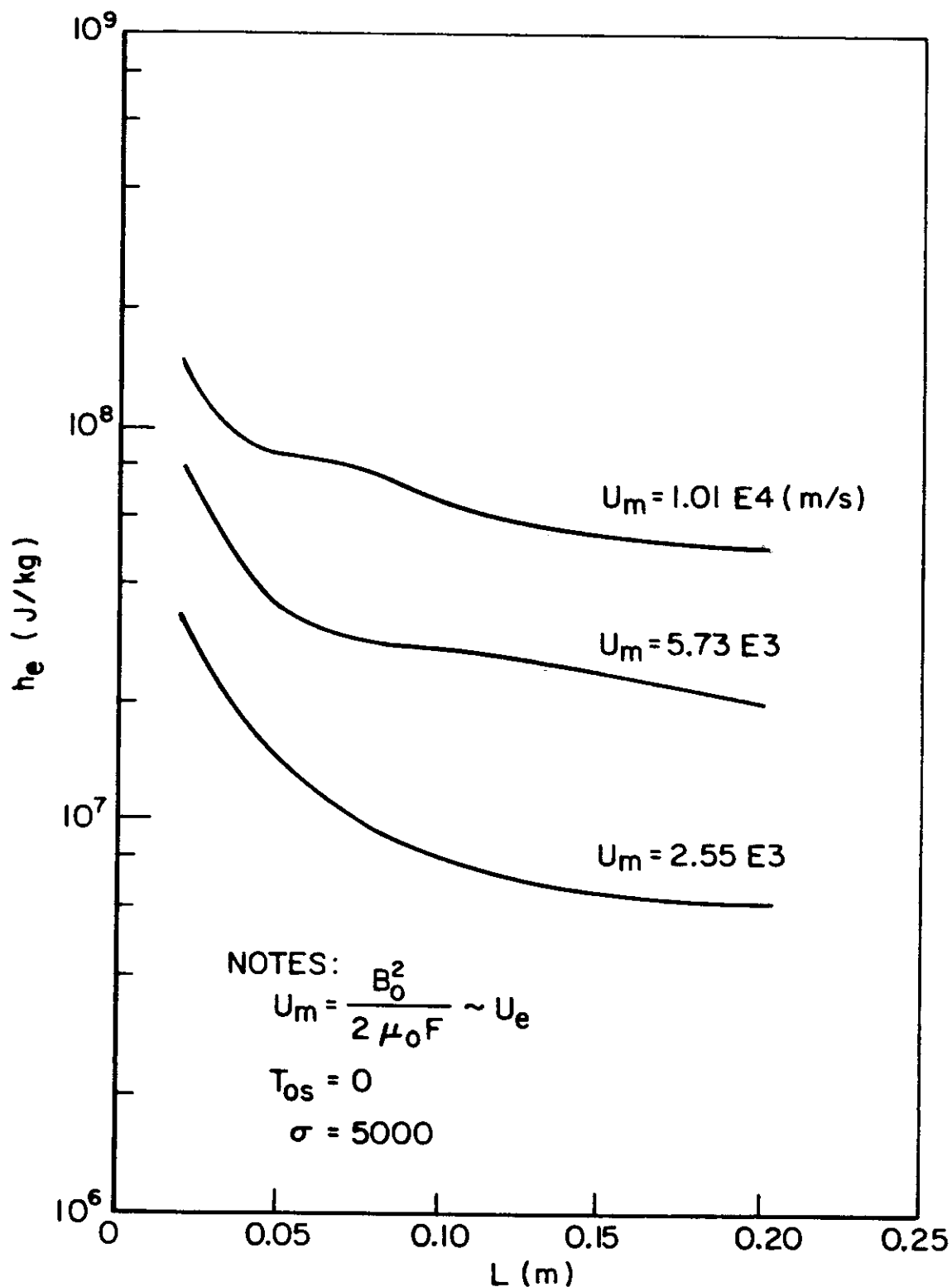
FIGURE 3.8

Segment CD is included to show the effect of a high pressure, subsonic exit on the electric field. Note that the field is substantially smaller than the supersonic case.

To summarise, curve OCAB is the characteristic for the accelerator model operating in a vacuum with a given (zero) stagnation temperature, electrode length, and mass flux. This curve exhibits a cubic dependence of E on B_0 , much like the observed dependence of thruster terminal voltage on current. Also on segment CA, a normal shock is present and adjusts the current density over the fixed length electrodes.

I: MODELED EFFECTS OF LENGTH AND MASS FLUX

Laboratory data have shown that the upper limit to specific impulse, reported as the parameter $(J^2/\dot{m})^*$, increases for longer electrodes and anodes of smaller diameters. For fixed J^2/\dot{m} , the effect of longer electrodes can be modeled directly as larger L , or R_m . For smaller diameter anodes, mass flux increases while holding J^2/\dot{m} fixed. The modeled effect of longer electrodes and smaller anode diameters at fixed J^2/\dot{m} indicates that enthalpy at the exit decreases for both changes. Figure 3.9 displays this effect, cast in the parameters $U_m (=B_0^2/z/\mu_0 F)$ and L . The model shows that these geometry changes delay the occurrence of high exit temperatures or enthalpies to larger J^2/\dot{m} values. Experiments show that these changes delay the onset of electrode erosion and voltage fluctuations to larger J^2/\dot{m} values. This correlation is thought to be important since temperature affects many plasma dynamic processes.



EXHAUST ENTHALPY VS ELECTRODE LENGTH
AND A VELOCITY SCALE

FIGURE 3.9

J: SUMMARY

A 1-D, steady, ideal gas model is developed and relates the electric field to boundary conditions. By taking the inlet stagnation temperature to zero the algebraic complexity of the solution is reduced. These solutions can be used to illustrate general characteristics of MPD accelerators in a simple form. Solutions with non-zero inlet stagnation temperatures are considered as a subset of the general characteristics.

Three modes of MPD acceleration are evident and can be delineated by a single parameter. These modes are:

- 1) electrothermally dominated with an exit Mach number of unity,
- 2) electromagnetically dominated with a sonic point near the inlet and a supersonic exit, and
- 3) the transition mode with sonic points both near the inlet and at the exit, with a Rankine-Hugoniot jump in between.

In each case the electric field is related to boundary conditions through the sonic singularity. Note that should a two dimensional geometry permit elongation of the acceleration zone, the shock in the transition mode need not occur.

To prescribe the problem with non-zero inlet temperatures, only four parameters are independent. The choice of these four strongly affects the model characteristics and considering B_0 , F , L , and T_{0s} as given will provide the closest representation of experimental operation. For this selection, the inlet gas dynamics are coupled to the arc such that the inlet pressure and Mach number vary strongly with the magnetic Reynolds number.

With an ideal working fluid, the parameter $B_o^2 / 2\mu_0 F$, which is similar to the empirical J^2 / \dot{m} scale, has a uniform effect on the thermodynamics and velocity such that it cancels out of the dimensionless problem. Should a real gas be incorporated in the problem, ionization would be important and dimensionless parameter such as $\frac{B_o^2}{2\mu_0 F} / \sqrt{\frac{q V_i}{m}}$ might be used to scale the thermodynamics, where the quantity in the square root is roughly the ionization energy per kilogram.

The ideal gas MPD channel flow is numerically unrealistic. The constant specific heats over the wide range of enthalpies encountered for typical boundary conditions produces exit temperatures and pressures far higher than measured values in laboratory thrusters. Utility of the results of the ideal gas they are thus limited to qualitative, rather than quantitative comparison with experimental thrusters.

Chapter 4

REAL GAS EFFECTS IN 1-D MPD FLOW

A: INTRODUCTION

The purpose of this chapter is to present solutions and analysis of a more realistic model of the acceleration process. In this chapter effects of both ionization and tensor conductivity on the 1-D channel are assessed. Also, to substantiate the analytical results, a methodical comparison with experiment is made. To assess the effects of ionization, an equilibrium equation of state is introduced to the simple algebraic model of chapter 3. The more complex real gas model is analysed in depth as the behavior of thermodynamic and plasmadynamic phenomena are examined. Heat addition, work done on the fluid, magnetic convection and diffusion, and exhaust characteristics are related to geometry, mass flow, and current.

Tensor conductivity effects are assessed as an approximation to the 1-D channel. As such, the magnitude of the effect is estimated but not incorporated in the quantitative results or comparison with experiment. The text of this chapter follows this course:

- 1) The building blocks of the equilibrium gas MPD channel analysis and tensor conductivity approximation are given in sections B-G.

- 2) The various phenomena are summarized in section H by examining the characteristics of a 1-D MPD channel or streamtube.
- 3) Parametric agreement with experiment and a sensitivity analysis of modeled parameters verify the model in section I.

B: REAL-GAS MPD CHANNEL EQUATIONS

This section presents the argon equilibrium equation of state, a simplified form of that equation, and the dimensionless conservation equations used in this analysis. An equilibrium state equation that includes ionization effects may be written:

$$p/\rho = g(h, \rho)$$

Figure 4.1 shows g vs. h at 3 typical densities, and since g is insensitive to density, the curve with $\rho = 0.003$ will be used to construct an approximate equation of state $G(h)$: \36\

$$p/\rho = G(h) \tag{1a}$$

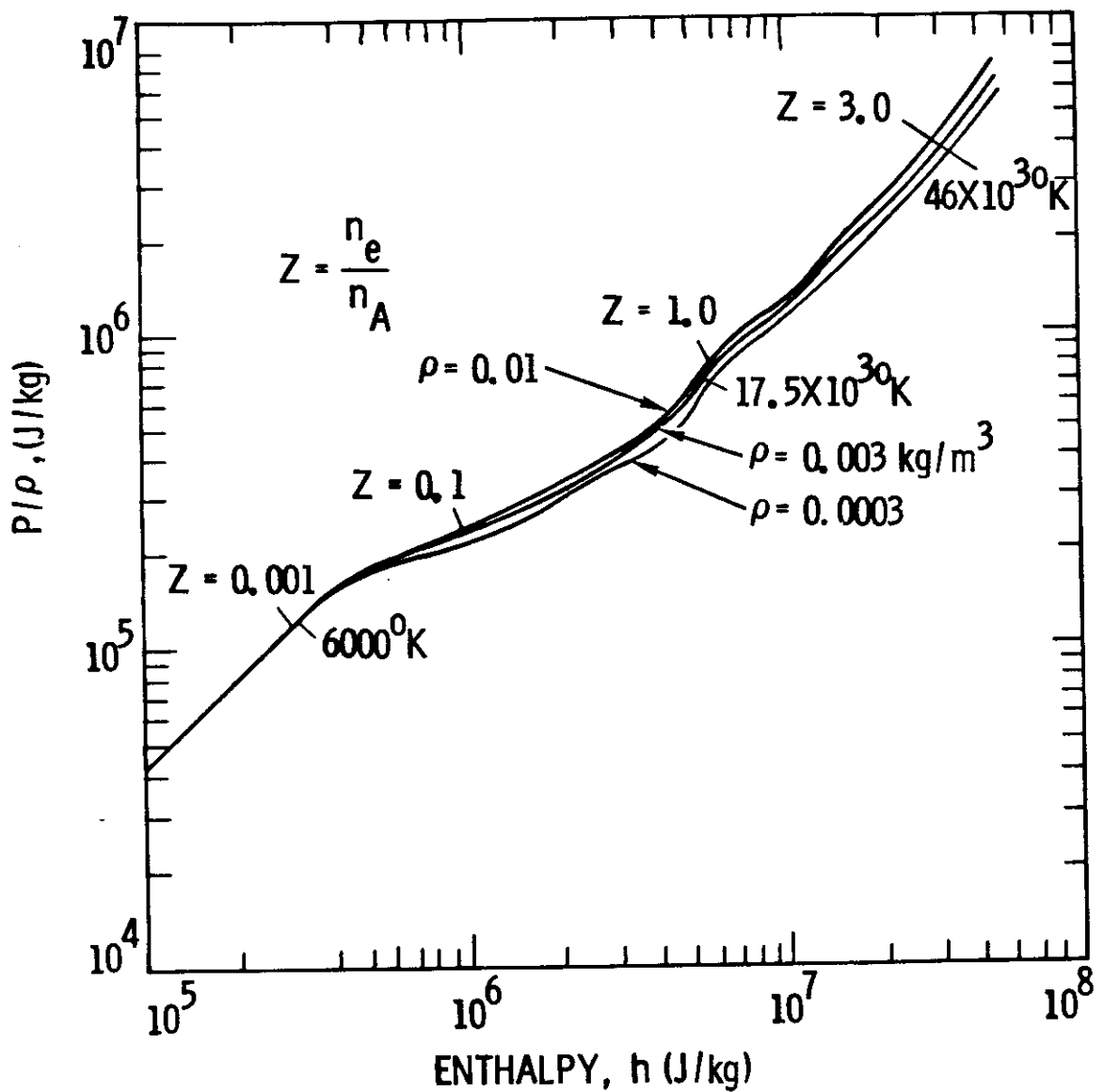
$$G(h) \equiv g(h, 0.003) \tag{1b}$$

For this state equation the isentropic speed of sound, derived in appendix 2, is:

$$a^2(h) \equiv \left. \frac{\partial p}{\partial \rho} \right|_{s=\text{CONST}} = \frac{G(h)}{1 - \frac{dG}{dh}} \tag{2}$$

Both G and a^2 are obtained from a table of equilibrium argon properties by a method described in appendix 2.

Due to non-constant specific heats, enthalpy is made dimensionless by a constant, h_{∞} :



ARGON EQUILIBRIUM EQUATION OF STATE
FIGURE 4.1

$$h' = h/h_{zi} ; \quad n_e/n_a = z ; \quad z(h_{zi}) = 1 ;$$

where n_e and n_a are the electron and atomic number-densities. G and a^2 are also rendered dimensionless by h_{zi} :

$$G' = G/h_{zi} ; \quad a'^2 = a^2/h_{zi} .$$

Conductivity is made dimensionless in a similar fashion:

$$\sigma' = \sigma(h)/\sigma_{zi} ; \quad \sigma_{zi} = \sigma(h_{zi}) .$$

Inserting the dimensionless state variables into the governing equations requires, in addition to the definitions of chapter 3, a new dimensionless parameter $\mathcal{F} = U_m^2/h_{zi}$. This parameter accounts for non-uniform specific heats and controls the range of enthalpy in the problem. For small values ($\mathcal{F} < 0.01$) solutions tend toward low temperature, ideal gas behavior, while large values ($\mathcal{F} > 1$) signify energetic solutions with a fully ionized gas. With the above definitions, the dimensionless 1-D, steady mass, momentum and energy equations are:

$$\rho' u' = 1 \tag{3}$$

$$u' + \frac{G'}{u' \sqrt{\mathcal{F}}} + B'^2 = u_o' + 1 + \beta_o \tag{4}$$

$$u'^2/2 + h'/\mathcal{F} + 2\mathcal{F} B' = u_o'^2/2 + h_o' + 2\mathcal{F} \tag{5}$$

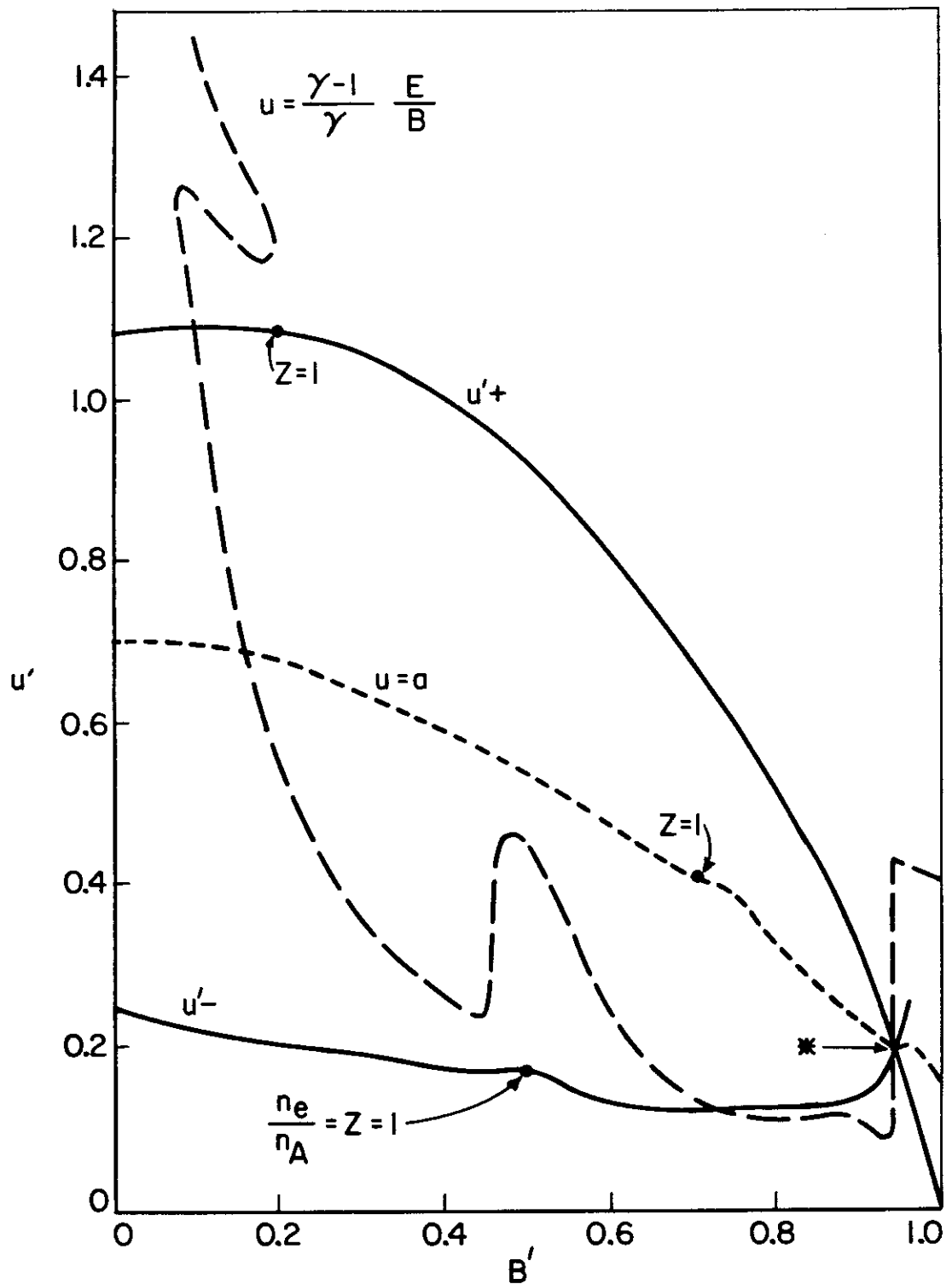
After specifying T_{os} , \mathcal{F} , and β_o , these equations are solved by numerical methods using algebra similar to the ideal gas analysis. These methods are described in appendix 3.

C: DIFFERENCES BETWEEN IDEAL AND REAL GAS ANALYSES

The major difference introduced by the equilibrium equation of state is the change to non-constant specific heats. Due to a variable ratio of specific heats, the profile of u vs. B and the numerator and denominator of du/dB are significantly altered. These curves are shown in fig. 4.2 for $\beta_0 = 1/4$ and $\xi = 1.0$ and can be compared to the same curves in fig. 3.4, which is computed for an ideal gas. For an ideal gas, β_0 is always 1.0 and drops out of the analysis. The sonic point has shifted upstream for the case of variable specific heats due to a significant change in the numerator of du/dB which is $(\gamma(h)-1)/\gamma(h) = u'B'/\xi$. The reader should examine the downstream portions of fig. 4.2 and 3.5. In contrast with the ideal gas problem, real gas solutions have reduced pressures at large enthalpies which tend to flatten the downstream portions of the sub- and supersonic velocity profiles.

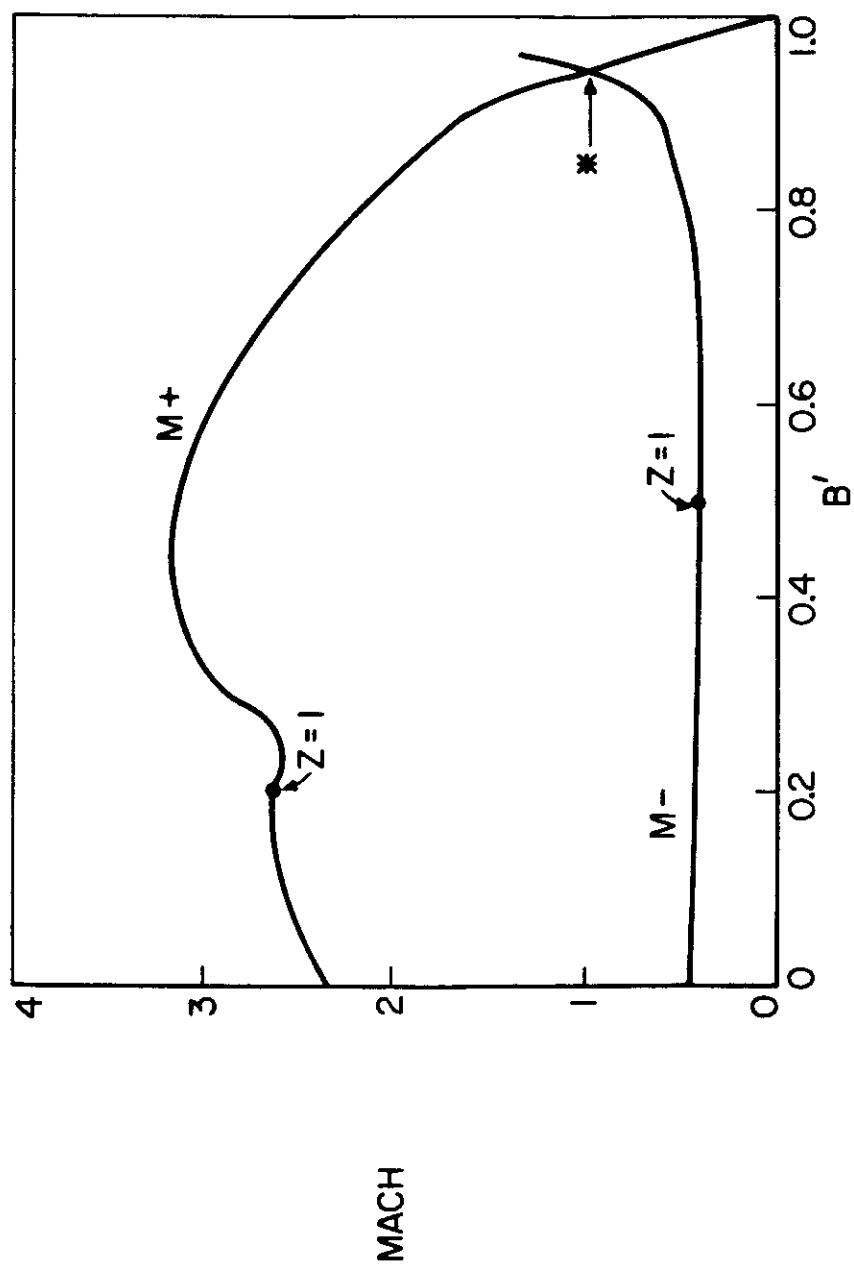
Varying specific heats also affect the Mach number profile and the $\xi = 1.0$, $\beta_0 = 1/4$ case is shown in fig. 4.3. The profiles are in general flatter than in the ideal gas computation, but contain wiggles where the temperature passes through ionization levels. Exit Mach numbers are not limited to 1.8 as in the $\gamma = 5/3$ case, but can reach as high as about 6 at $Rm = \infty$. The supersonic curve near the inlet terminates before B' reaches 1 since the temperature is zero at this point.

Another significant change is the transition β_0 which is no longer constant, but is a function of ξ . Also the value of β_0 at $Rm = \infty$ is a function of ξ .



REAL GAS ELECTROMAGNETIC MODE ACCELERATION
PROFILES, $\beta_0 = \frac{1}{4}$, $\zeta = 1.0$, ($\xi = 1.008$)

FIGURE 4-2



MACH NUMBER PROFILES, $\beta_0 = \frac{1}{4}, \zeta = 1.0$
FIGURE 4-3

D: MAGNETIC REYNOLDS NUMBER

The development, computation, and functional form of the magnetic Reynolds number can be used to explain several phenomena in the MPD channel. In this section the magnetic Reynolds number is related to the inlet pressure ratio β_0 , the dimensionless electric field ξ , and the parameter ξ . This relationship is necessary to couple the electric field to inlet conditions and geometry. The magnetic Reynolds number is a ratio of convected to diffused magnetic field, and can be found after combining two Maxwell equations and Ohm's law:

$$\frac{\partial \underline{B}}{\partial t} = \nabla \times (\underline{u} \times \underline{B}) - \nabla \times \left(\frac{\nabla \times \underline{B}}{\mu_0 \sigma} \right) \quad (6)$$

In accord with previous definitions, the steady, dimensionless, 1-D form of this magnetic diffusion equation is:

$$0 = \frac{du'B'}{dx'} + \frac{1}{R_m} \frac{d}{dx'} \left(\frac{dB'}{dx'} \frac{1}{\mu_0 \sigma} \right)$$

where $R_m = (u_m L) / \left(\frac{1}{\mu_0 \sigma} \right) \quad (7)$

In channel flow, the magnetic Reynolds number can be used to non-dimensionalize Ohm's law, and forms a key relationship between several boundary conditions. This construction was performed in chapter 3, and the result is repeated here for convenience:

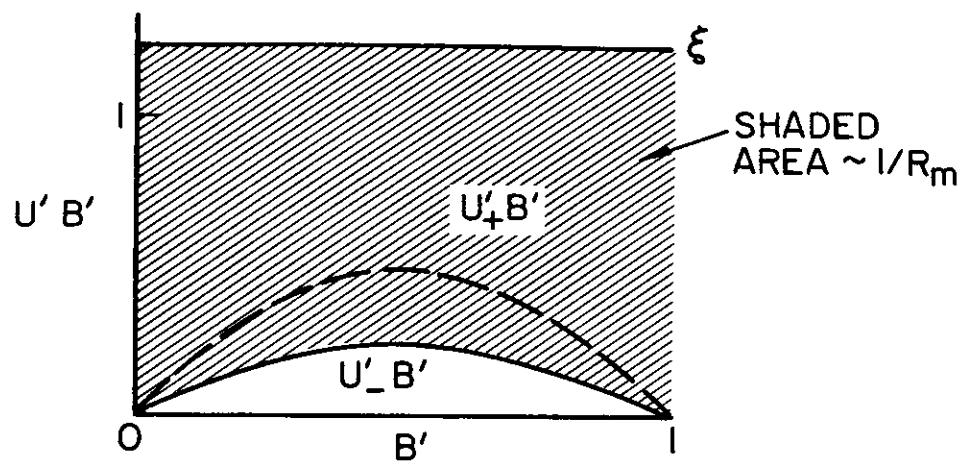
$$\mu_0 \sigma \xi \left(\frac{\beta_0^2}{2\mu_0 F} \right) L = \int_0^1 \frac{dB'}{\sigma'(\xi - u'B')} \quad (8)$$

The magnetic Reynolds number is key to the analysis for two reasons. First equation (8) is useful, in fact essential, for coupling inlet gas dynamics to the arc. Second, the magnetic

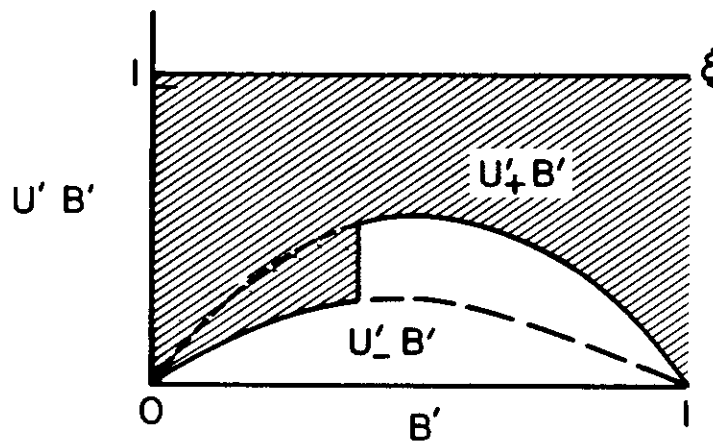
Reynolds number characterizes the flow beyond the simple definition (7); it can also be related to thrust efficiency and tensor conductivity.

The computation of the magnetic Reynolds number from (8) is a mapping of the solution in the $u'-B'$ plane onto the spatial coordinates of the electrodes. Also buried in the mapping is an implicit coupling of the inlet gas dynamics to the arc. To compute R_m , the parameters ξ, β_0 and $T_{os'}$ must be specified and the choking point located at either the exit (the electrothermal mode) or near the inlet (the electromagnetic mode). To illustrate the computation, three sketches, one for each case of $u-B$ profiles, are shown in fig. 4.4. The solid line is the actual locus of (u, B) , the shaded area represents $1/R_m$, and the dotted line shows the alternate, unused (u, B) locus for visual reference. The electrothermal case (fig. 4.4a) has subsonic velocities except for $Me=1$, and has a large shaded area or small R_m . The transition case has two choking points: the exit and near the inlet. There is a single, unique electric field in this case, but a range of R_m values found by adjusting the jump from supersonic to subsonic velocities from left to right on fig. 4.4b. The electromagnetic case (fig. 4.4c) has a choking point near the inlet and a small shaded area hence large R_m . Review figure 4.4 and note that the vertical distance $\xi-u'B'$ is proportional to current density.

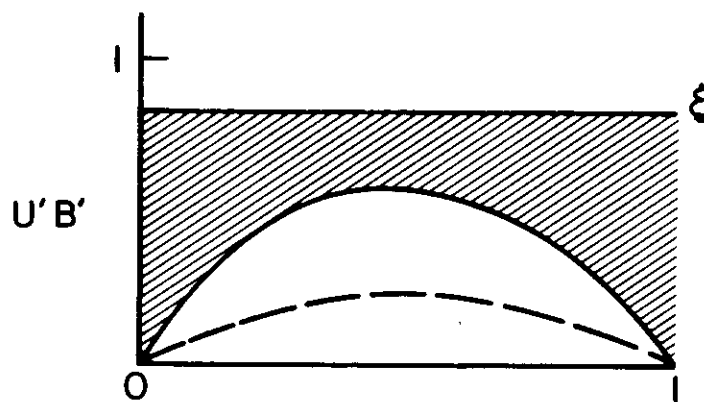
The computation of R_m is represented by a family of curves, parameterized by ξ as shown in fig. 4.5. The lower portion of each curve is labeled as electrothermal, while the vertical line



a) ELECTROTHERMAL



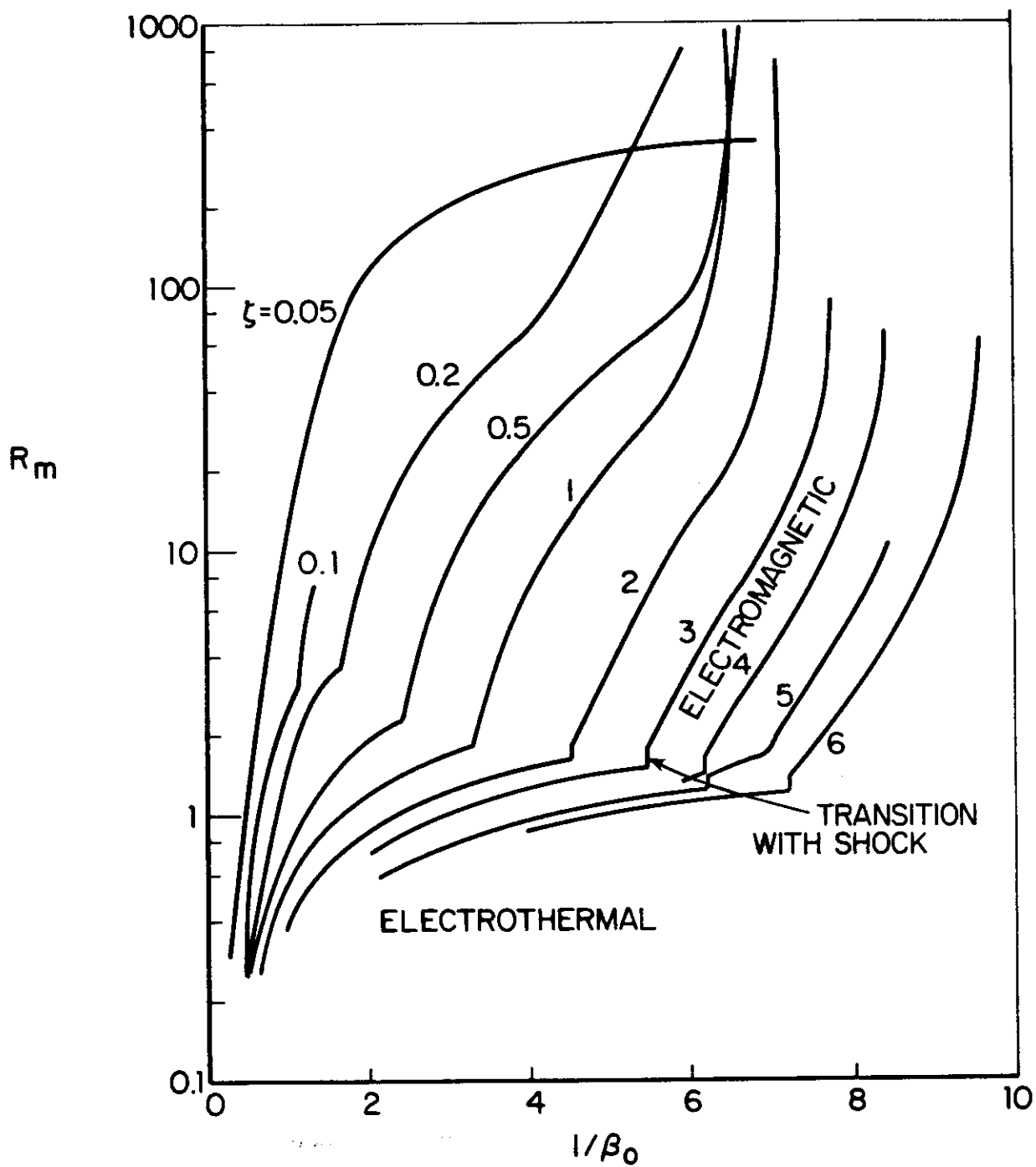
b) TRANSITION



c) ELECTROMAGNETIC

ILLUSTRATION OF 3 CASES OF
 R_m COMPUTATION

FIGURE 4.4



REAL GAS MAGNETIC REYNOLDS NUMBER
FIGURE 4.5

shows the transition region, and the upper portion is labeled as electromagnetic.

The value of β_0 is strongly coupled to the numerical solution as it fixes the right hand side of the momentum equation. β_0 can be interpreted as the ratio of gas dynamic to magnetic interaction. When the MPD channel problem is solved from a dimensional point of view consistent with experiment, the quantities ξ , R_m , and Tos are known and β_0 must be found from fig. 4.5.

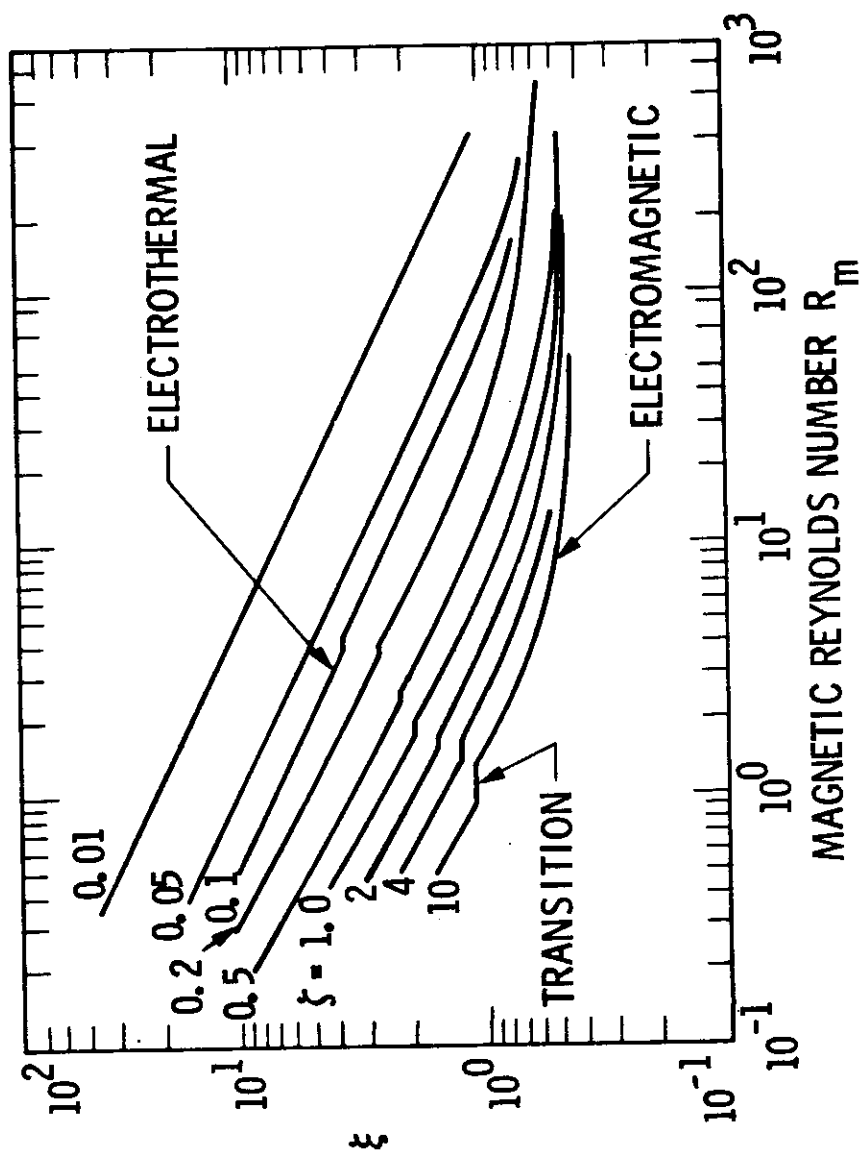
Concurrent with the calculation of R_m is the calculation of the dimensionless electric field. The dimensionless electric field $\xi = (\xi, R_m, Tos')$ expresses the coupling of the sonic point in the discharge to the power input. Given an unlimited power, constant current supply, this phenomena "chokes" the power input; i.e. the power input is related to channel geometry and upstream conditions. Figure 4.6 shows ξ for the three types of MPD acceleration: 1) the electrothermal mode with small R_m , 2) a narrow band of the transition mode, and 3) the electromagnetic mode with large R_m . Electrothermal portions of ξ in fig. 4.6 suggest that the acceleration process is governed by Ohm's law with a small back EMF and that magnetic diffusion controls the current distribution. This can be illustrated by (8) with $u'B' \rightarrow 0$:

$$R_m \approx \int_0^1 \frac{dB'}{\sigma \xi} = \frac{1}{\xi} \int_0^1 \frac{dB'}{\sigma}$$

or

$$\xi \approx \frac{1}{R_m} \int_0^1 \frac{dB'}{\sigma'} \quad (9)$$

Since the integral is of order 1, the dimensionless electric field is approximately proportional to the inverse of the mag-



NOTE: $\zeta = 0.05, 0.01$ ARE ALL ELECTROTHERMAL

DIMENSIONLESS ELECTRIC FIELD, REAL GAS MODEL

FIGURE 4-6

netic Reynolds number, for electrothermal flow. This relation is born out by a rough curve fit of the electrothermal portion of fig. 4.6 which is similar to (9):

$$\xi \propto (R_m \xi)^{-0.75} \quad (10)$$

The electromagnetic current distribution is dominated by magnetic convection, since the magnetic Reynolds number approaches infinity as the back EMF approaches the electric field, according to (8). The asymptote of ξ over R_m in fig. 4.6 is due to this limiting process.

The transition region occurs in fig. 4.6 where $\xi \approx R_m$, that is, where the ratio of the applied field, E , to the back EMF is balanced by the ratio of convected to diffused magnetic field. Flow with $\xi > R_m$ is predominantly subsonic, has a weak back EMF and strong magnetic diffusion. Flow with $\xi < R_m$ is predominantly supersonic, has a strong back EMF and hence strong magnetic convection. Flow with $\xi = R_m$ has comparable portions of sub- and supersonic flow.

Coincidentally, strong magnetic convection occurs with large kinetic energy addition, while significant magnetic diffusion occurs with thermally accelerated flow. For this reason, simple thermodynamics are useful in further illustrating the acceleration process.

E: SIMPLE THERMODYNAMICS OF MPD CHANNELS

By relating energy addition to electrical conduction, a key measure of thruster efficiency is found. This measure can be used to explain the behavior of heat addition, work done on the fluid, and the limitation on thrust efficiency in relation to the magnetic Reynolds number.

Replacing dh and dp/ρ in the combined first and second laws of thermodynamics which is:

$$Tds = dh - \frac{dp}{\rho}$$

with ρ , u , B , E , and dB by using the momentum and energy equations

$$u du + \frac{dp}{\rho} + \frac{B dB}{\mu_0} = 0$$

$$u du + dh + \frac{E dB}{\mu_0 \rho u} = 0$$

results in

$$Tds = -(E - uB) \frac{dB}{\mu_0 F} \quad (11a)$$

$$\frac{\int_{S_{IN}}^{S_{EXIT}} Tds}{2 h_{21} F} = 1 - \frac{1}{F} \int_0^1 u' B' dB' \quad (11b)$$

The integral $\int u B dB$ is the work done on the fluid by the Lorentz force and the rightmost term of (11b) resembles the thrust efficiency. Due to this resemblance, and since it is a useful and important quantity, the ratio of work done on the fluid by the Lorentz force to the electrical power input has been designated the Lorentz efficiency:

$$\eta_L \equiv \frac{1}{F} \int_0^1 u' B' dB' \quad (12)$$

The ratio of heat added to the fluid to the energy input is simply $1-\eta_L$. MPD acceleration with large heat input will be thermally dominated and lossy while acceleration with a large fraction of work done by the Lorentz force can be efficient. For the given assumptions of the model, the limiting case of infinite magnetic Reynolds number can produce maximum Lorentz efficiencies of 0.68, as shown in fig. 4.7.

F: ROLE OF TENSOR CONDUCTIVITY

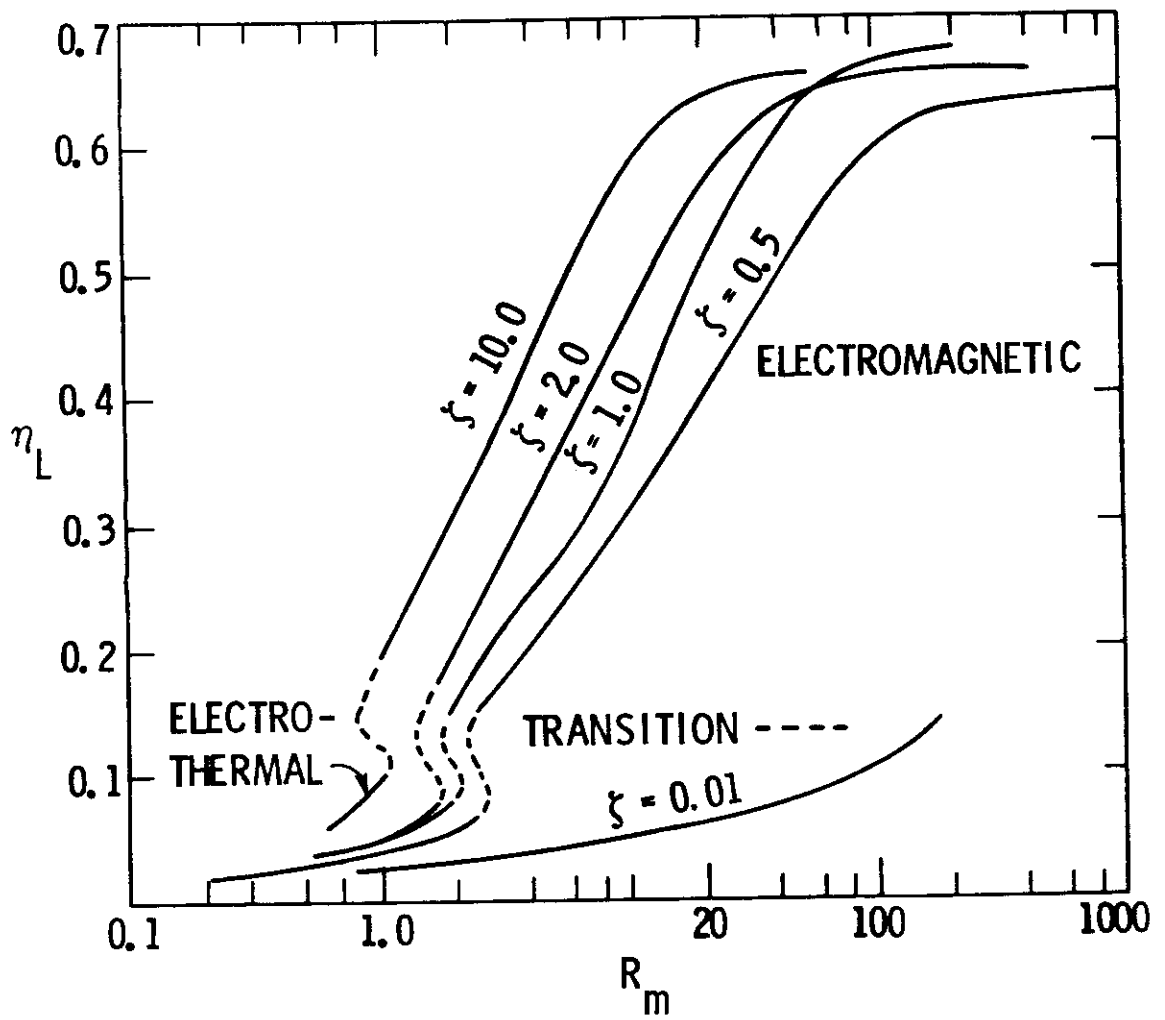
Up to this point the model is based on a set of 1-D equations, and these permit only scalar conductivity to be employed. But experiments (Figs. 2.8, 2.9) indicate large Hall parameters ($\Omega \sim 10$) are common in MPD thrusters, so that the scalar conductivity used in the model may be too large by a factor of $(1+\Omega^2)$ for conduction in the transverse direction.

Reduction of the 2-D MPD equations to a "1.1-D" form shows that the scalar conductivity model may be considered as an approximation for flow with non-zero Hall parameter. Additionally, the first order correction for tensor conductivity involves only Ohm's law and the computation of R_m . The 2-D continuity equation can be used to form an estimate of the transverse velocity (see fig. 3.2 for coordinates):

$$\frac{u_y}{u_x} = O\left(\frac{d}{L}\right) \text{ or } u'_x = O(1); \quad u'_y = O\left(\frac{d}{L}\right).$$

The 2-D transverse momentum equation is:

$$\rho u_x \frac{\partial u_y}{\partial x} + \rho u_y \frac{\partial u_y}{\partial y} = -\frac{\partial p}{\partial y} + j_x B_z \quad (13)$$



LORENTZ EFFICIENCY
FIGURE 4-7

If u_y' is negligible, then a good approximation of the continuity equation is $\rho = \rho_0 \frac{u_{x0}}{u_x}$. Using $x' = x/L$, $y' = y/d$, and other variables made dimensionless as before, the y-momentum equation can be rewritten:

$$\frac{d}{L} \frac{\partial u_y'}{\partial x'} + \frac{u_y'}{u_x'} \frac{\partial u_y'}{\partial y'} \approx \frac{\partial \left(\frac{2\mu_0 p}{B_0} \right)}{\partial y'} + 2 \frac{\partial B_z'}{\partial y'} B_z' \quad (14)$$

$$O\left(\frac{d^2}{L^2}\right) \qquad O\left(2\Omega \frac{d}{L}\right)$$

Further, if both the electric field and the back EMF components that are parallel to the electrodes remain small, then the Hall parameter is related to the current:

$$\Omega = J_x/J_y = -\frac{\partial B_z'}{\partial y'} / \frac{\partial B_z'}{\partial x'} \frac{L}{d} \quad (15)$$

and $\frac{\partial B_z'}{\partial y'} = O\left(\frac{d}{L}\Omega\right)$ since $\frac{\partial B_z'}{\partial x'} = O(1)$.

For large Hall parameters $\Omega \sim L/d$, and for small d/L , the left hand side of (15) can be neglected, and gas pressure will balance magnetic pressure:

$$0 \approx \frac{2}{\partial y'} \left(B_z'^2 - \frac{2\mu_0 p}{B_0^2} \right).$$

Also if d/L is negligible, the 2-D x-momentum equation will approximate the 1-D equation (4). Using the above definitions, and the approximation $\rho u_x = \rho_0 u_0$, the energy equation can be written:

$$\left(\frac{\partial}{\partial x'} + \frac{L}{d} \frac{u_y'}{u_x'} \frac{\partial}{\partial y'} \right) [u_z'^2 + h'] \approx 2 \left(E_x' \frac{\partial B_z'}{\partial y'} \frac{L}{d} - E_y' \frac{\partial B_z'}{\partial x'} \right) \quad (16)$$

$$(O(1) \quad O\left(\frac{L}{d} u_y'\right)) [O(1)] \quad O(E_x' \Omega) \quad O(1)$$

If $u_y' \ll d/L$ and if $E_x' \ll 1/\Omega$ then the 2-D terms in (16) can be

neglected and the equation is one dimensional, i.e. is identical to (5). These two conditions are consistent with those employed in (14) and (15), but may not occur in the thruster except in regions very close to the electrode surfaces. But note that the terms $\frac{L}{d} \frac{u_y'}{u_x'} \frac{\partial}{\partial y'} \left(\frac{u'^2}{2} + h' \right)$ and $2E_x' \frac{\partial B_z'}{\partial y' d}$ are of the same sign (+) and that both tend to increase with Hall parameter. If these terms balance to zero in (16) or if $u_y' \ll d/L$ and $E_x' \ll 1/\Omega$ then the 1-D solutions are an approximation to axial flow with non-zero Hall parameter.

However, the foregoing tensor conductivity approximation assesses the Hall effect on the mapping of the magnetic field to spatial coordinates. The mapping with tensor conductivity, neglecting E_x and $u_y B_z$ is:

$$j_x = \frac{\sigma}{1 + \Omega^2} (E_y - u_x B_z) \quad (17)$$

The Hall parameter is defined as $\Omega = \omega_b / \gamma_c$ where $\omega_b = qB/m$ is the electron gyro frequency and γ_c is the electron-other collision frequency. The electron collision frequency can be related to a weighted average of electron-neutral and electron-ion conductivities:

$$\gamma_c = \frac{n_a q^2 \bar{R}}{m} \quad (18a)$$

$$\bar{R} = \left(1 - \frac{n_i}{n_a}\right) \frac{1}{\sigma_{en}} + \frac{n_i}{n_a} \frac{1}{\sigma_{ei}} \quad (18b)$$

where n_i is the ion number density. The Hall parameter is thus:

$$\omega_b / \gamma_c = \frac{B}{q n_a \bar{R}}$$

and using $u = F/\rho$ and $\rho = m_a n_a$ with dimensionless variables is:

$$\Omega = \left[\mu_0 \sigma_{zi} \frac{B_0^2}{2\mu_0 F} \left(\frac{m_a}{q\mu_0} \frac{B_0}{F} \right) \right] \frac{u' B'}{R \sigma_{zi}} \quad (19)$$

The factor in brackets is designated the transverse magnetic interaction parameter:

$$\frac{S_T}{2} \equiv \mu_0 \sigma_{zi} \frac{B_0^2}{2\mu_0 F} \left(\frac{m_a}{q\mu_0} \frac{B_0}{F} \right) \quad (20)$$

This differs from the magnetic Reynolds number (7) by the length scale (in parenthesis) which has the form of the ion gyro radius:

$$r_{b,i} \equiv \frac{m_a}{qB} v_{\perp}$$

where $B=B_0$ and $v = u_m$

$$r_{b,i} = \frac{m_a B_0}{2\mu_0 q F}$$

The transverse magnetic interaction parameter, computed from simple inlet conditions, is a useful measure of the peak Hall parameter. This peak Hall parameter will occur at the peak back EMF, provided the gas is singly ionized.

For energetic, highly ionized flow, the back EMF will peak near $B'=0.5$ such that $(u'B')_{peak} \sim \xi$. Large Hall parameters can occur at this point for channel conditions of typical MPD thrustors, as shown by some values in Table 4.1.

(1) B	(2) ξ	(3) Rm	St	(4) Ω	$\tan^{-1} \Omega$
0.05	0.017	1.95	0.161	0.03	1.8
0.10	0.272	7.80	1.28	0.64	33
0.15	1.38	17.5	4.34	2.17	65
0.20	4.36	31.2	10.3	5.14	79
0.25	10.6	48.7	20.1	10.0	84

Notes:

- (1) For a coaxial thruster $B = 2E-7$ J/r
- (2) $F=1.0$; $h_{zi}=5.82E7$ (mks)
- (3) $L=0.2$ m; $\sigma_{zi}=7800$ (mks)
- (4) Estimated for $\overline{R}\sigma_{zi}$ = exit value and $u'B'=0.5$

Hall and Transverse Magnetic Interaction Parameters
in the MPD Thruster

Table 4.1

Note that large St and Ω occur with large Rm. For MPD channels operated like MPD thrusters with fixed mass flow and electrode length, the peak Hall parameter increases like B_o^3 and Rm like B_o^2 .

G: EFFECT OF TENSOR CONDUCTIVITY

The first order correction to the earlier $\Omega=0$, 1-D solutions for the effects of tensor conductivity is made by redefining R_m :

$$R_{m\Omega} \equiv \int_0^1 \frac{\left[\frac{1+\Omega^2}{1+(St/2)^2} \right] dB'}{\sigma'(\xi - u'B')} \simeq \frac{R_m}{1+(St/2)^2} \quad (21)$$

This corrects the mapping of magnetic field to spatial coordinates for tensor conductivity. The factor $\frac{1+\Omega^2}{1+(St/2)^2}$ is of order 1 over $0 \leq B' \leq 1$ so that the integral is similar to (8). For purposes of discussion, R_m in figs. 4.5 - 4.7 can be replaced by $R_m/(1+(St/2)^2)$, for low and moderate values of R_m (<10).

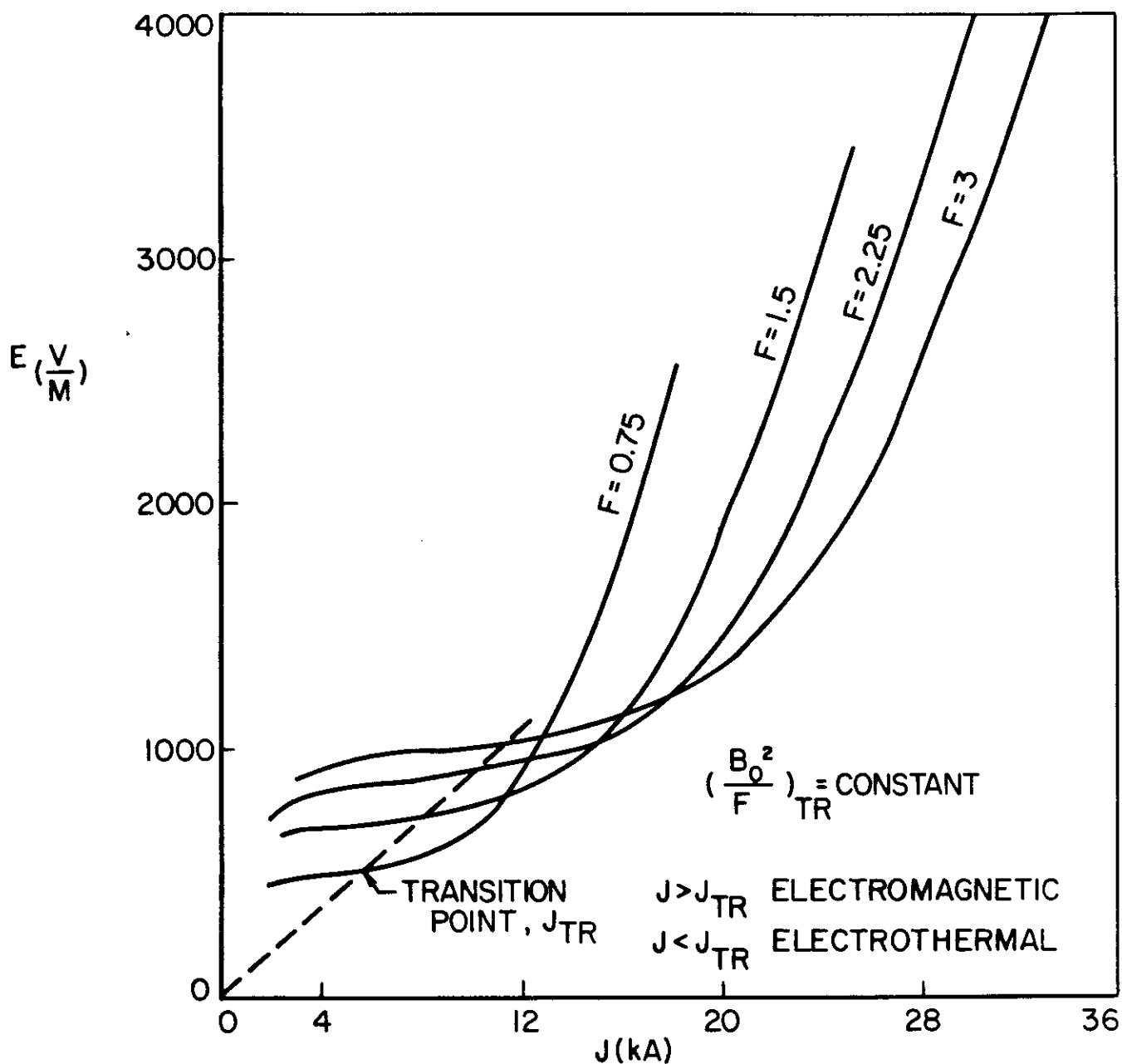
In fig. 4.6, for fixed thruster conditions B_0 , F , L , and Tos , this correction reduces the ordinate by a factor of $1/(1+(St/2)^2)$ and implies a larger electric field \mathcal{E} . The Lorentz efficiency (fig. 4.7) would similarly be corrected to a smaller value. In general, the tensor conductivity correction increases the electric field, heat addition, and discharge losses over the $\Omega=0$, 1-D calculation.

H: 1-D STREAMTUBE "TERMINAL" CHARACTERISTICS

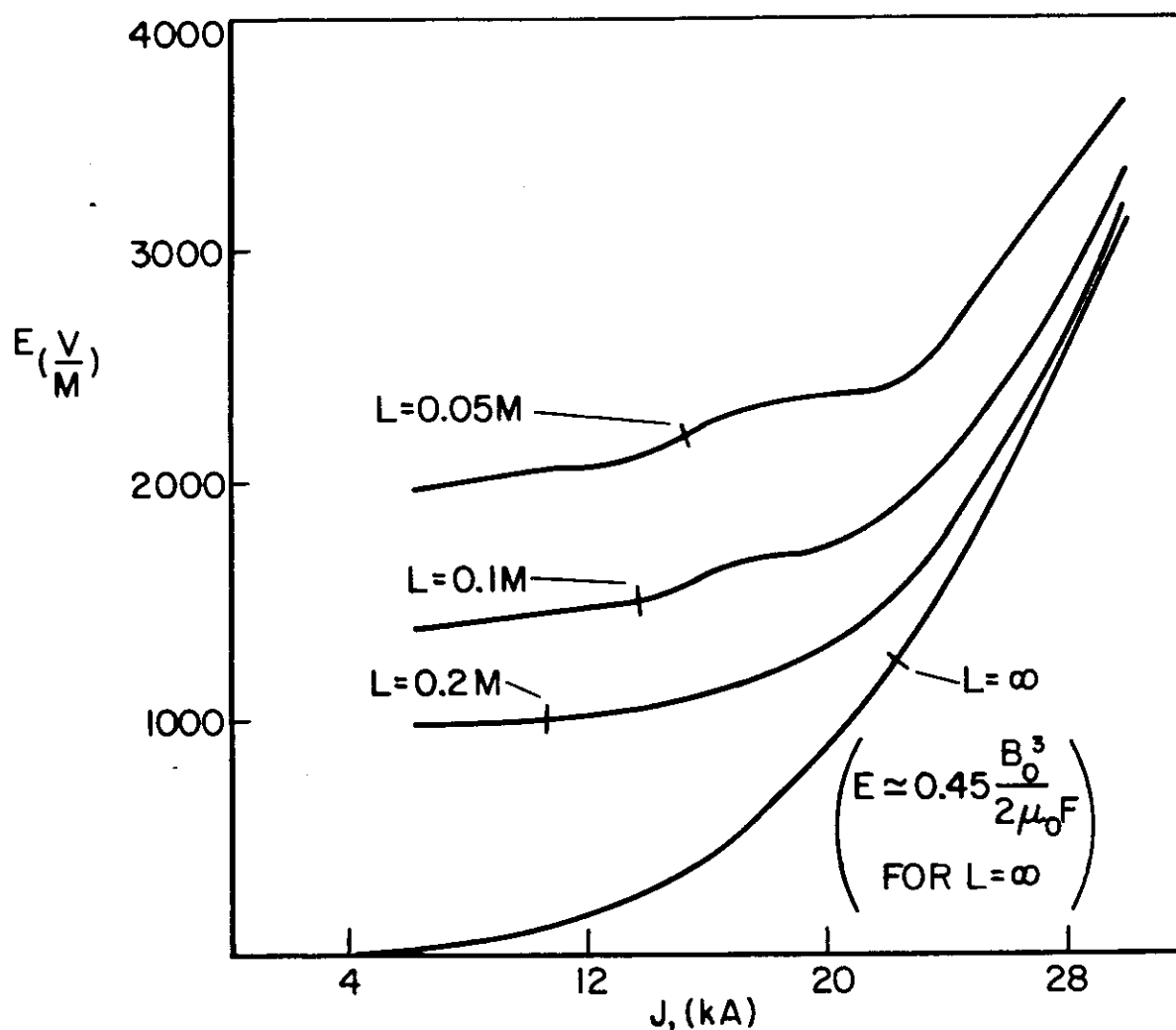
By relating the dimensionless MPD channel parameters to a thin annular streamtube, some characteristics of coaxial thrusters can be explained. Using the methods in section 3H and figs. 4.5 and 4.6, the electric field accross a streamtube can be found for the real gas accelerator given B_o , F , L , and Tos . For a thin annular streamtube in a coaxial geometry, the magnetic field is $B_o = \frac{\mu_o J}{2\pi r}$. In this manner, the electric field is computed as a function of current. Figure 4.8 shows the electric field vs. current computation for several mass flux values, a 0.016 m radius and a 0.2 m length. In this figure, at low currents, ($J < 10$ kA) the electric field is roughly proportional to $B_o \sqrt{F}$, while at high currents ($J > 2$ kA) is approximately $0.45 B_o^3 / 2\mu_o F$. The transition from electrothermal to electromagnetic acceleration occurs roughly at fixed Rm so that $E_{tr} = f(L, Tos) J_{tr}$. Other characteristics are shown for fixed mass flux and several electrode lengths in fig. 4.9. These curves show that the electric field rapidly approaches its minimum value, given by $L = \infty$, at high currents.

The exit velocity and Mach number are shown in fig. 4.10 for the annular streamtube. The velocity scales with $B_o^2 / 2\mu_o F$ and is insensitive to length at high currents. The Mach number clearly illustrates the electrothermal ($Me=1$) to electromagnetic ($Me>1$) mode transition. The transition point and electromagnetic mode Mach numbers are significantly affected by the different length electrodes.

The behavior of the thrust efficiency resembles the exit

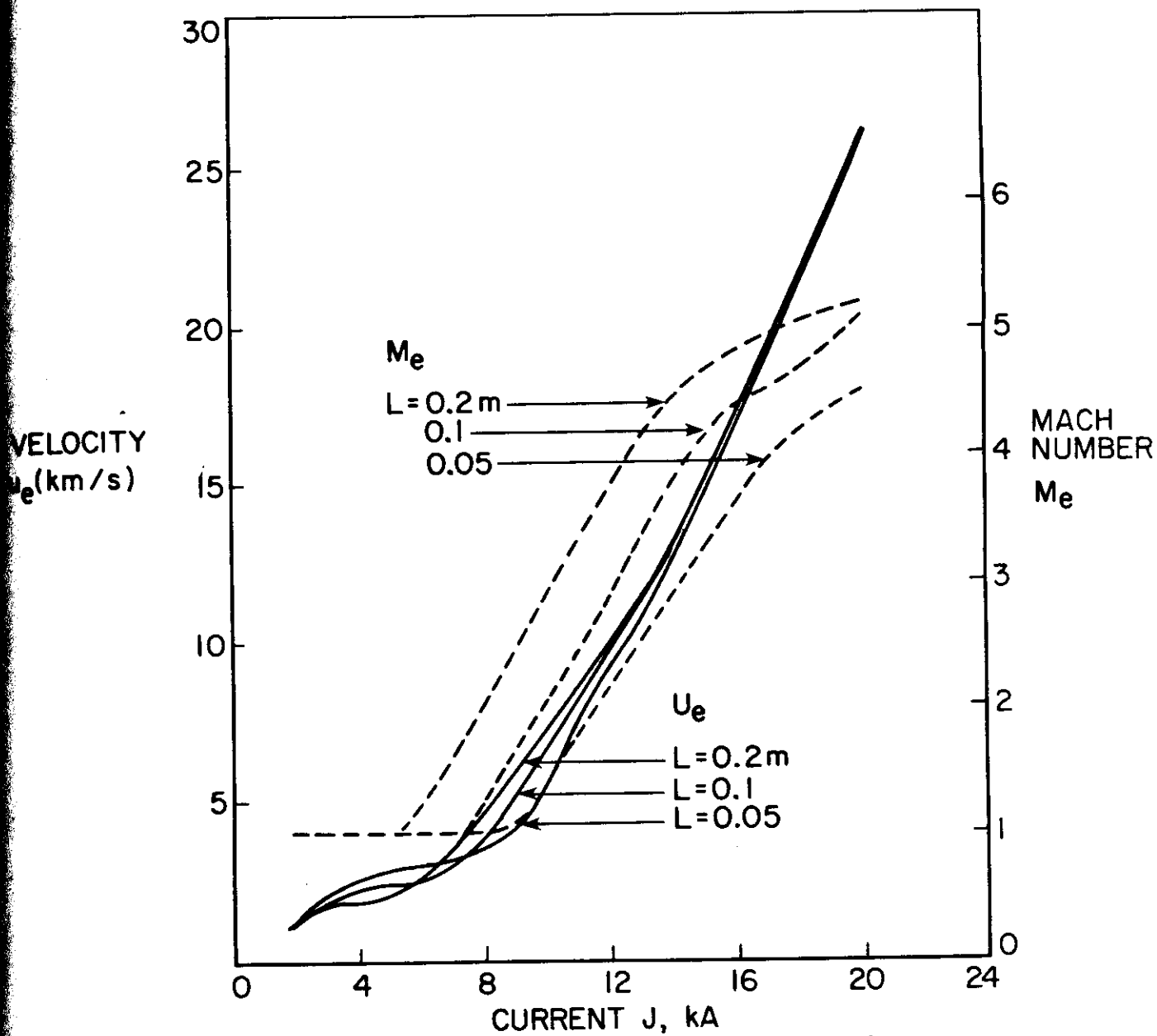


STREAMTUBE ELECTRIC FIELD vs CURRENT FOR $L=0.2\text{m}$
FIGURE 4.8



STEAMTUBE COMPUTED ELECTRIC FIELD vs CURRENT
FOR 3 LENGTHS, $F = 3$

FIGURE 4.9



STREAMTUBE EXHAUST CHARACTERISTICS, $F=1 \frac{\text{kg}}{\text{s}}$, $r=0.016\text{m}$

FIGURE 4-10

Mach number, and for ideal gases is approximately:

$$\eta \approx \frac{m_e^2 (1 + \frac{1}{\gamma_0 m_e^2})^2}{m_e^2 + \frac{2}{\gamma_0 - 1}} \quad (22)$$

For the real gas analysis, the thrust efficiency is more readily computed from ξ and β_0 . Operating in a vacuum, the thrust density is:

$$f = p_e + F u_e = \frac{\beta_0^2}{2\mu_0} (1 + \beta_0 + u_0') \quad (23)$$

where the inlet velocity, given T_{0s} is:

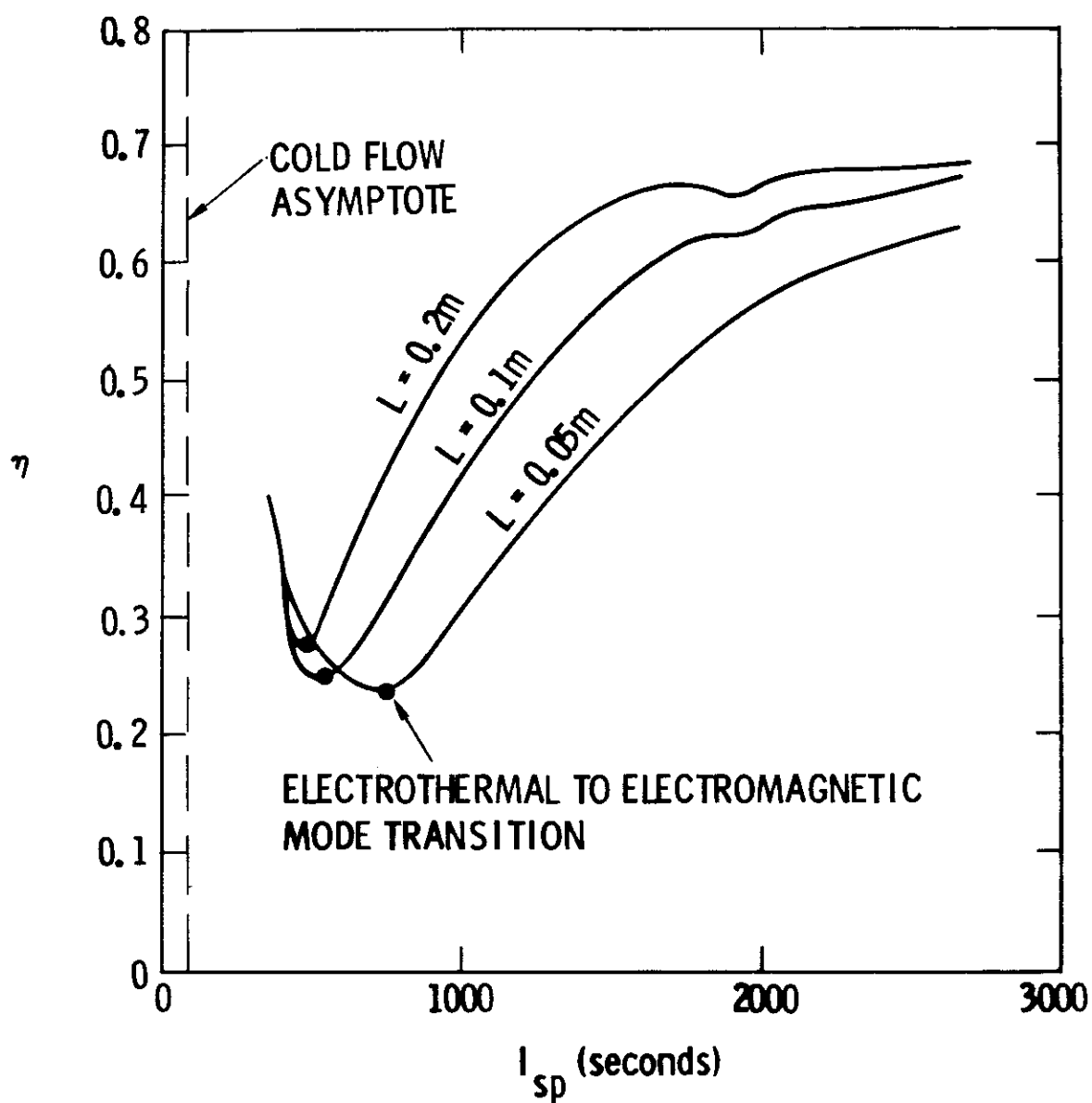
$$u_0' = \frac{-\gamma_0}{\gamma_0 - 1} \beta_0 + \sqrt{\left(\frac{\gamma_0}{\gamma_0 - 1} \beta_0\right)^2 + \frac{2 c_p T_{0s}}{\gamma h_{zi}}} \quad (24)$$

The specific impulse and thrust efficiency are:

$$I_{sp} = \frac{f}{F g_E} = \frac{u_m}{g_E} (1 + \beta_0 + u_0') \quad (25)$$

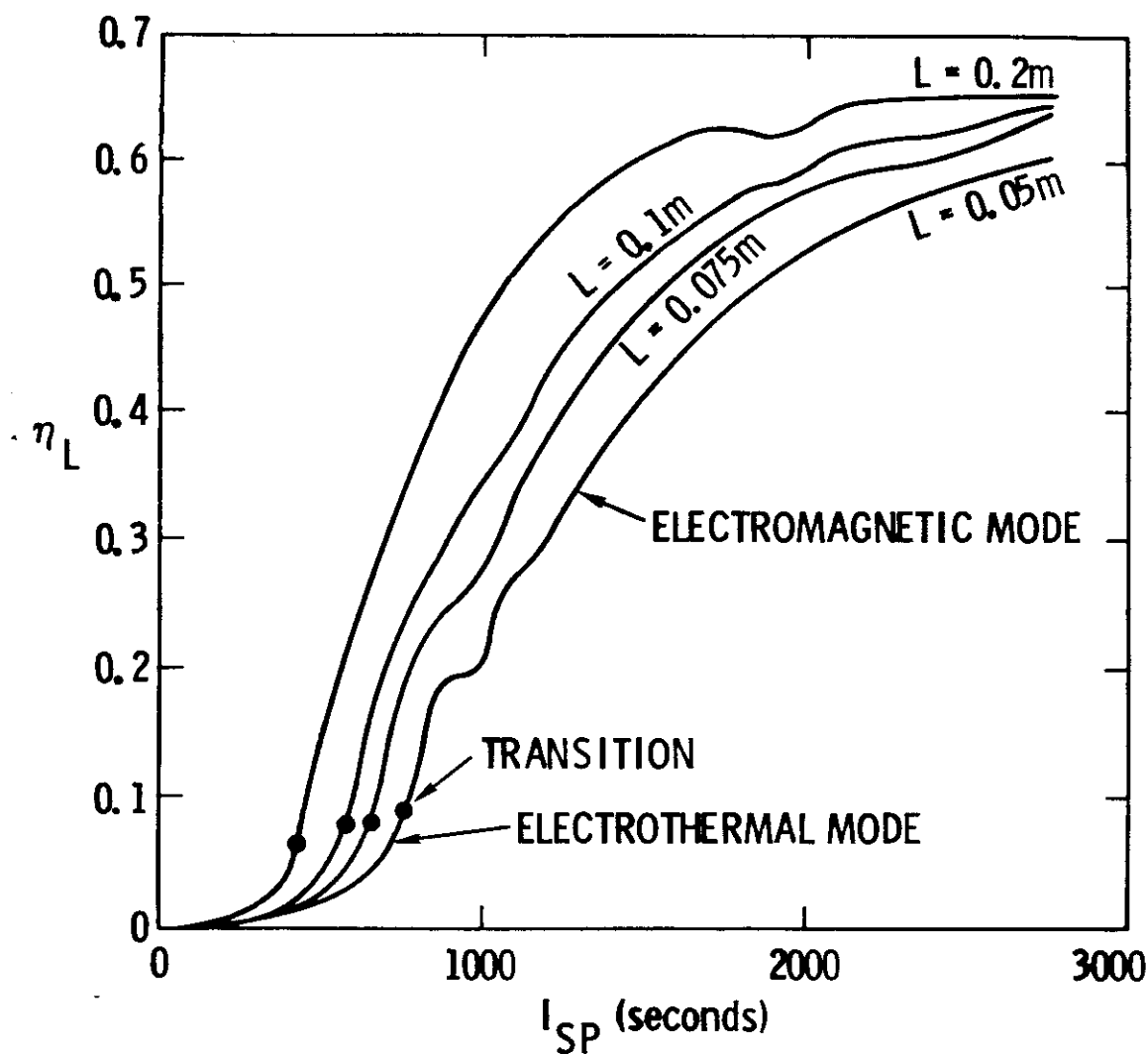
$$\eta = (f^2 / 2F) / \left(\frac{E \beta_0}{\mu_0} \right) = \frac{(1 + \beta_0 + u_0')^2}{4 \xi} \quad (26)$$

The thrust efficiency-specific impulse characteristic for three electrode lengths is shown in fig. 4.11. As the electrical power is reduced to zero, the cold flow provides an asymptote in thrust efficiency. The gap in η between 70 and 200 secs Isp is not correctly computed by the program. In this range, the gas dynamic values overflow the machines infinity as these values are made dimensionless by small electromagnetic parameters.



STREAMTUBE THRUST EFFICIENCY
FIGURE 4-11

A comparison of the thrust efficiency and the Lorentz efficiency which is the fraction of work done by the body force, provides a clear picture of energy addition in the channel. The Lorentz efficiency, η_L , is small in the electrothermal region as seen in fig. 4.12. The fractional heat added $1-\eta_L$, is large in the thermal mode, and yet provides moderate thrust efficiencies. Increasing specific impulse from 200 secs, the thermally dominated thrust efficiency decreases until the transition to the electromagnetic mode acceleration is reached. In the electromagnetic mode, the heat addition may be larger than the work done by the body force and yet the exit velocity is supersonic. At large Isp, the Lorentz efficiency approaches an asymptotic value of 0.66. Finally the wiggles in the Lorentz efficiency near 950 secs for $L=0.05$ m and near 1900 secs for $L=0.2$ m occur at the same total heat input $\int T ds = 2 h_{zi} \xi \xi (1-\eta_L)$. For this range of energies the specific heats vary rapidly as the gas is singly ionized near the choking point in the channel. The electric field is determined at this location and is affected by these rapidly varying specific heats. These wiggles may be removed by using a smooth equation of state.



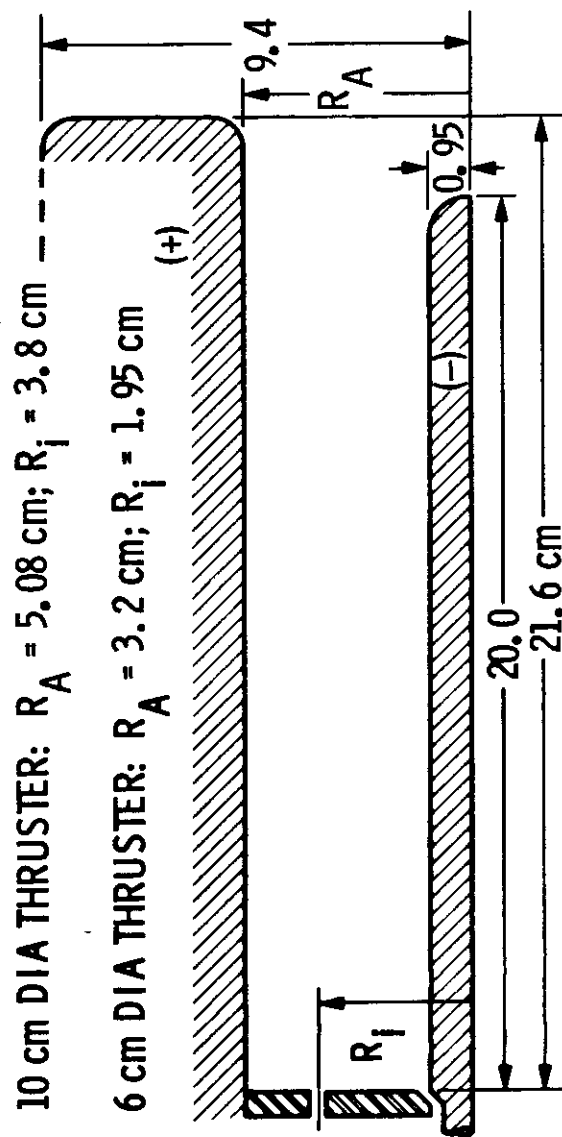
STREAMTUBE LORENTZ EFFICIENCY
FIGURE 4-12

I: COMPARISON OF THEORY AND EXPERIMENT

In this section, a comparison of theory and experiment is presented, and the sensitivity explicit to parameters and implicit to formulation is explored.

The electric field is a good index for comparison since it is both readily measured and is sensitive to the formulation and boundary conditions of the model. If the thruster to be operated from a constant current power supply, then the electric field will depend strongly upon inlet conditions (current, mass flux, and stagnation temperature), the propellant (equation of state), electrode length, and electrical conductivity. Correct modeling of the physics of the acceleration process can be inferred from experimental verification of the electric field, as shown in the following. Since there are three terms in the energy equation (5), and since at high currents the first term (velocity) can be found within a few percent of the correct value via Maxwell's stress tensor, it follows that the correct modeling of the second term (enthalpy) can be inferred by verifying the third term (given by the electric field). At low currents the component of electromagnetic acceleration is small, the acceleration is governed by gas dynamics and the total heat input, and correct modeling of total power input can be inferred from verification of the electric field.

A 10 cm dia., 20 cm long thruster (same as VCL20 in chapter 2) is selected for comparison with theory (fig. 4.13). The electrode geometry and current streamline data suggest that the flow near the cathode is subject to little curvature effects and traverses a region of moderate Hall parameter, i.e., is nearly



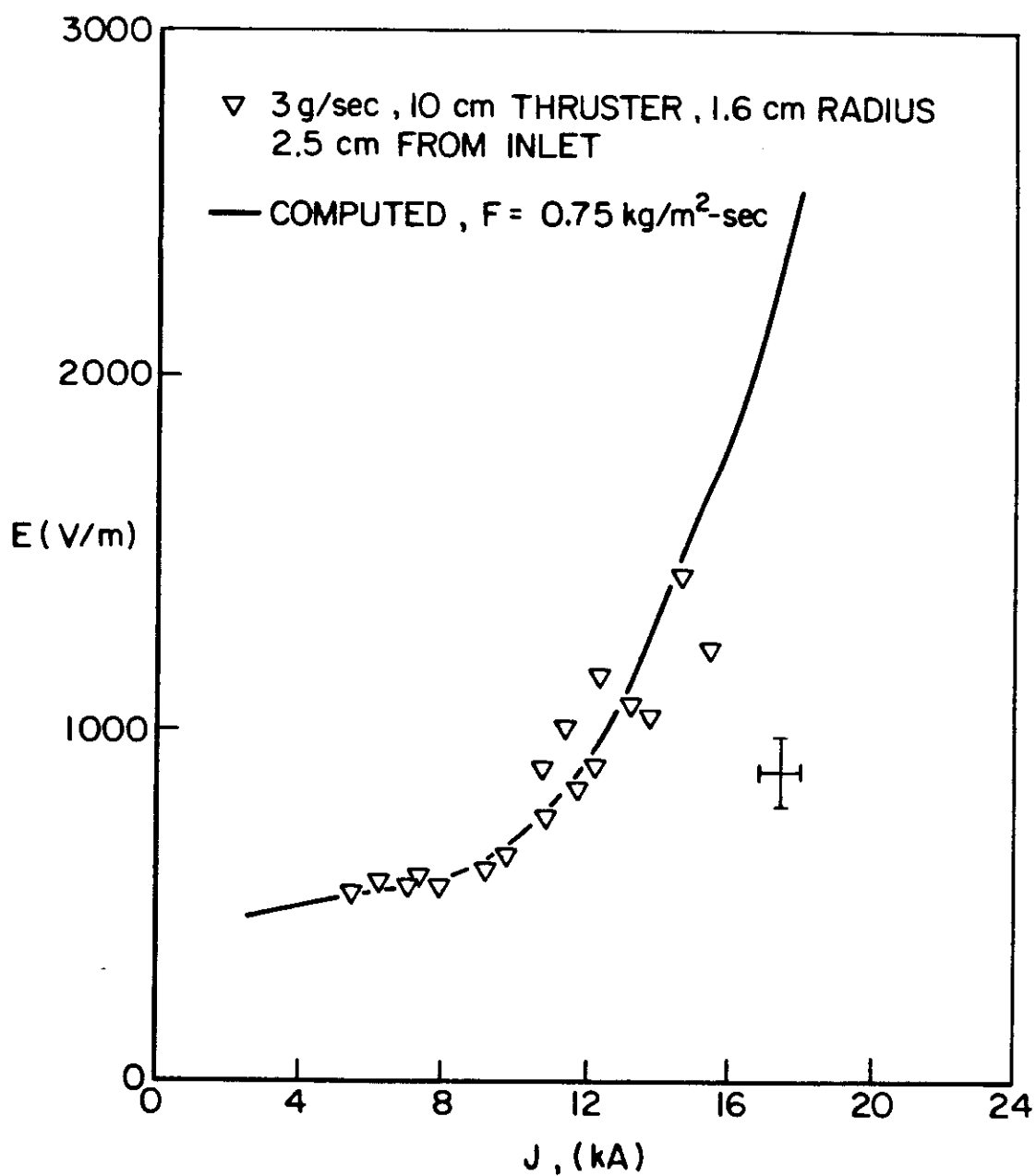
HIGH ASPECT RATIO THRUSTERS
FIGURE 4.13

one-dimensional with predominantly scalar conductivity.

A radial survey, 2.5 cm downstream of the inlet, of the radial electric field shows a sharp peak near a radius of 2 cm at a current and mass flow just below the onset limit of 1.2×10^{11} A²-sec/kg. At this radius, which is midway between the gas injection ports, and at the onset limit luminous layers and large Hall parameters have been observed. For these reasons, a radius of 1.6 cm was selected as a benign but typical location for further electric field measurements.

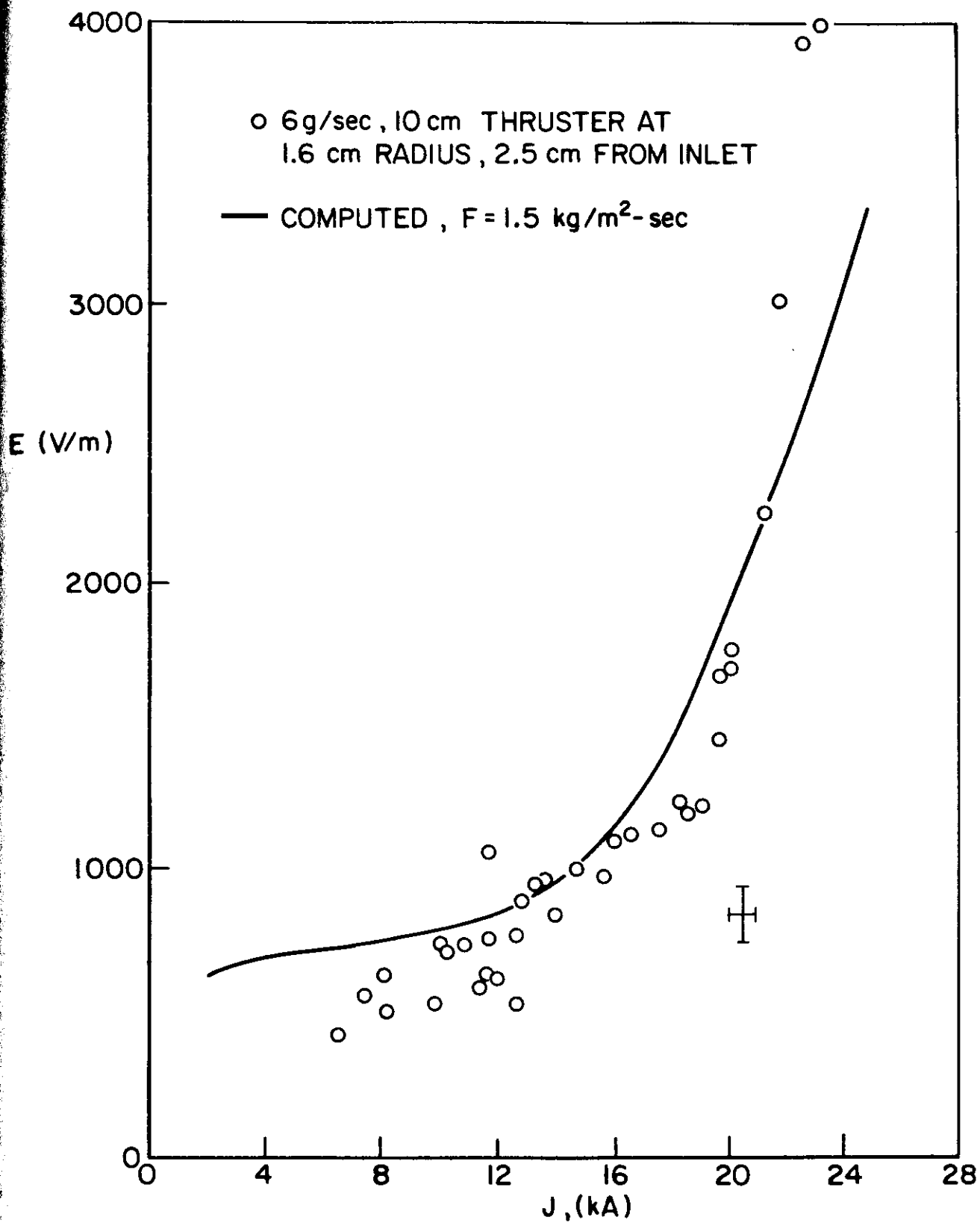
The theory is verified by the following comparison. The radial electric field vs. current data at an argon mass flow of 3 g/sec is shown in fig. 4.14. The solid curve represents the computed electric field. The mass flux in the computation has been adjusted for good fit with the data, and is a reasonable value, twice the average mass flux in the experiment. Photographs of the discharge indicate that the mass flux in the experiment is not uniform, and is therefore unknown at the measurement location. In figures 4.15 and 4.16, the mass flux in the computation, and mass flow in the experiment have been systematically varied, and good agreement is evident over a 3 to 1 change in mass flow, and 6 to 1 change in current.

Explicitly, the modeled electric field can be expressed as a function of four parameters, $E(J, F, L, T_{os})$, at a fixed radius. The sensitivity to the first three parameters is shown in figs. 4.8 and 4.9. Here, E varies over a range of 8 to 1 while current varies over a domain of 6 to 1 and mass flux over 4 to 1. At large currents, E is insensitive to L , and this corresponds to



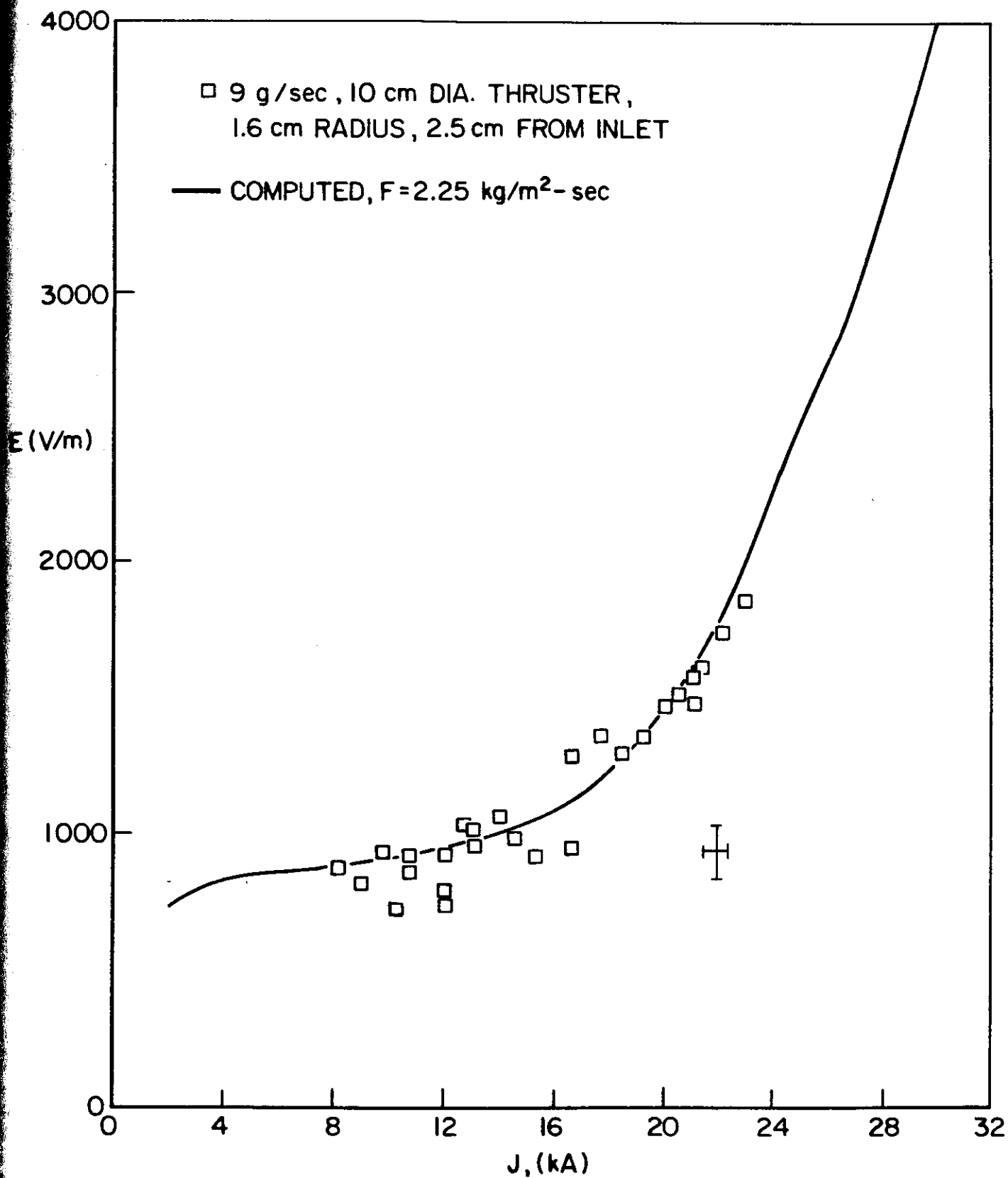
RADIAL ELECTRIC FIELD vs CURRENT

FIGURE 4.14



RADIAL ELECTRIC FIELD vs CURRENT

FIGURE 4.15



RADIAL ELECTRIC FIELD vs CURRENT

FIGURE 4.16

the behavior of ξ at large R_m . E is insensitive to Tos since this quantity represents a small inflow of energy with regard to the electrical energy added to the fluid.

Implicitly, the electric field value is sensitive to the formulation of conductivity. This sensitivity can be explored using the function $\xi(R_m, \zeta)$ or fig. 4.6. To generate figs. 4.14-4.16, R_m varies over a domain of 1 to 100 and ζ over about 0.05 to 10. Tensor conductivity effects are small for $R_m < 2$ due to a weak magnetic interaction. For $R_m > 20$, e approaches an asymptote which is unaffected by tensor conductivity. Applying the tensor conductivity approximation of section F to a curve fit (equation (10)) of fig 4.6, the electric field is roughly:

$$\xi \propto \left[\frac{(1 + (St/2)^2)^2}{R_m \xi} \right]^{0.75}; 2 \leq R_m \leq 20 \quad (27)$$

The tensor conductivity approximation can be applied for small moderate St , i.e. $St < 2$. This approximation and equation (27) are intended to show the Hall effect on E , rather than provide an accurate assessment of tensor conductivity. The development of (27) exaggerates these effects on E , and for $St < 2$, the Hall effect increases E over the scalar conductivity computation by no more than a factor of 1.7.

The mass flux affects both R_m and ξ such that errors in the assumed mass flux value and errors in the conductivity formulation are very difficult to separate by comparison with experiment.

To summarize, the electric field is strongly dependent upon the theoretical formulation and is sensitive to the parameters used in the comparison. After matching theory to experiment at one datum, parametric agreement is maintained over a significant range of currents and mass flow, thus supporting the utility of the theory.

J: SUMMARY

The 1-D, steady, equilibrium gas, scalar conductivity, MPD channel theory has been compared with experiment and is found to be in agreement over parametric variations of current and mass flux. Since the computation is sensitive to these parameters, the agreement supports the utility of the theory.

Computations are made using scalar conductivity, but consideration of tensor conductivity requires use of approximate 1-D equation. The introduction of tensor conductivity would increase the electric field and decrease thrust efficiency from the values of the scalar conductivity model, while holding other parameters fixed. This effect has not been computed, but is negligible in the electrothermal mode due to small magnetic interaction. In the electromagnetic mode, the tensor effects occur primarily downstream of the choking point, and therefore have a weak, indirect effect on terminal properties.

By considering flow along a typical streamtube of an experimental thruster, the model can be used to interpret the effects of geometry parameters in terms of thrust, work done on the fluid, heat added, total power input, and thrust efficiency. At fixed current and mass flow, a reduction in anode orifice area quenches and cools the discharge which has a higher mass density profile but a lower thrust efficiency. Also at fixed operating conditions, an increase in electrode length results in a more diffuse current density, cooler discharge and improved thrust efficiency.

Chapter 5

APPLICATIONS OF THE 1-D REAL-GAS MODEL

A: INTRODUCTION

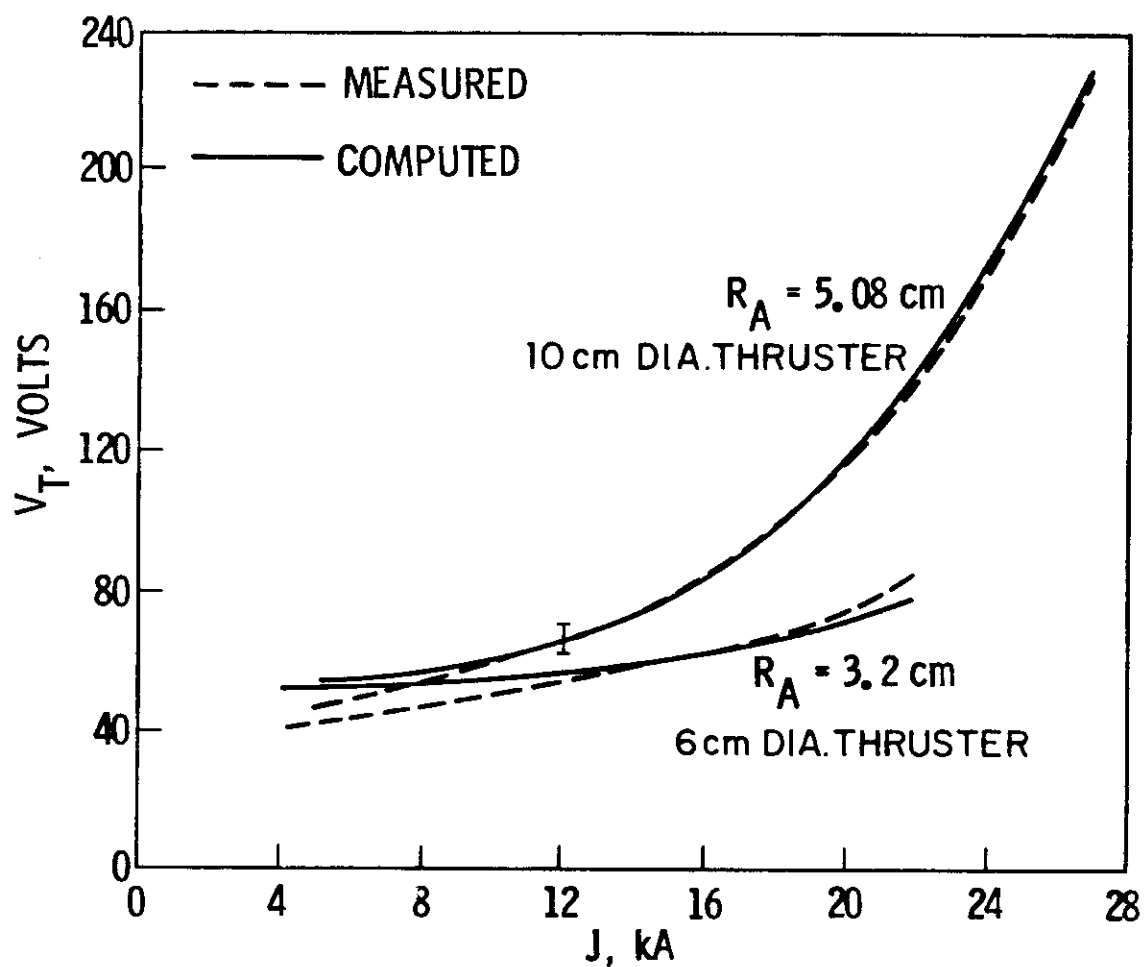
By treating the coaxial MPD thruster as a set of thin, concentric streamtubes, the 1-D model can be employed to estimate the voltage-current and thruster efficiency-specific impulse characteristics. These annular streamtubes allow the cylindrical curvature effects to be neglected, and the 1-D approximation restricts the modeling to thrusters with long electrodes which constrain the flow to the axial direction. Since the axial momentum added to the gas is large, and the density of the gas is low, viscous coupling between both adjacent streamtubes and electrode-gas interfaces can be neglected without penalty.

B: VOLTAGE-CURRENT CHARACTERISTICS AND ELECTRODE GEOMETRY

With the electric field from fig 4.6, a constant mass flux given by $F = \dot{m}/\text{area}$, and V_f to represent the electrode sheaths, the terminal voltage can be approximated by:

$$V_t = \int_{R_c}^{R_a} E dr + V_f \quad (1)$$

Experiments show that the sheath potential drop is roughly constant over a wide range of currents, and a drop of 35 volts is used. Figure 5.1 shows the measured and computed voltage-current characteristics for the high aspect ratio 10 cm and 6 cm thrusters (fig. 4.13).³⁷ The calculation for the 10 cm thruster agrees with measurements, within the error bar, over a range of



MEASURED AND COMPUTED VOLTAGE - CURRENT CHARACTERISTICS
FOR TWO HIGH ASPECT RATIO THRUSTERS

FIGURE 5.1

8 to 27 kA, and the 6 cm thruster over 10 to 22 kA. Variations in electrode length and anode orifice radius agree parametrically with experiments, but only qualitatively since these other thrusters exhibit two-dimensional behavior. Cautious use of the model in the form of (1) can supplement experimental data in design of a thruster for a given power level and I_{sp} .

C: ONSET LIMIT AND THRUSTER GEOMETRY

Experiments with various thruster geometries and the 1-D theory suggest that the onset limit, electrode erosion, and voltage oscillations occur when the Hall parameter exceeds a critical value somewhere in the flow. The model can be used to assess the effect of electrode geometry on this parameter. It indicates for electromagnetic mode operation at a given I_{sp} , J^2/\dot{m} , and hence input power, that an increase in electrode length will increase the Lorentz efficiency (fig 4.12) and hence decrease the temperature profile along a streamline. Also, according to theory, for operation at fixed length and J^2/\dot{m} a decrease in anode orifice radius increases mass flux and quenches the arc to an extent such that the temperature profile again decreases. In a Coulomb-collisional plasma, the collision frequency is inversely proportional to, and the Hall parameter is directly proportional to temperature to the $3/2$ power. On these premises, both longer electrodes and smaller anode diameters should cause a reduction in the Hall parameter, at a given operating condition. The theory indicates that to regain given temperature and Hall parameter profiles after lengthening electrodes will require a small increase in J^2/\dot{m} (weak effect), but a reduction in anode orifice radius

will require a large increase in J^2/\dot{m} (strong effect). Experiments agree with this theory and show that lengthening electrodes is related to a weak increase in the onset limit $(J^2/\dot{m})^*$, while reducing anode orifice radii produces a strong increase in $(J^2/\dot{m})^*$.

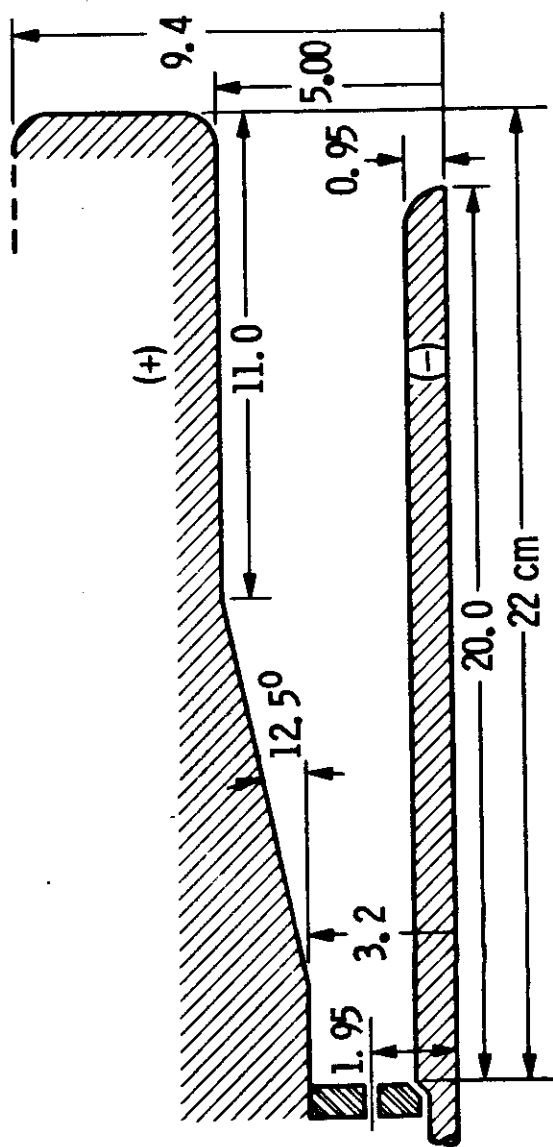
D: THRUST EFFICIENCY AND ELECTRODE DESIGN

To illustrate the utility of the model, a means of obtaining high thrust efficiency, proposed by the model, is evaluated by designing, building, and testing a new thruster configuration. The theory suggests that when operated in the electromagnetic mode, the terminal voltage-current characteristic is insensitive to changes in electrode geometry downstream of the choking point. But changing electrode shape here can have a favorable influence on thrust and thrust efficiency. For illustrative purposes, the predominant portion of the thrust at high currents can be written:

$$f_{em} = \frac{\mu_0}{4\pi} \ln r_{ac}$$

where r_{ac} is the ratio of effective anode and cathode current attachment radii. The electromagnetic mode choking point is shown in the analysis to be within 1 cm of the inlet, and employing a diverging anode cross section downstream of this point may increase the ratio r_{ac} , thrust, and hence thrust efficiency.

A thruster designed on this basis is shown in fig. 5.2. Note that the anode radius near the inlet, insulator, and cathode have the same dimensions as the 6 cm thruster shown in fig. 4.13, but that the downstream section diverges.



IMPROVED THRUST EFFICIENCY DESIGN

FIGURE 5.2

According to the model and the design, the diverging cross section thruster should have a voltage-current characteristic similar to the 6 cm (cylindrical) thruster but an improved thrust efficiency. Experiments agree: the voltage-current characteristics are identical within the error bar while the effective current attachment ratio has increased from $r_{ac} = 3.4$ with the 6 cm cylindrical anode thruster to $r_{ac} = 4.5$ for the diverging anode thruster. Comparing these two thrusters at the onset limit of 21 kA, the inferred electromagnetic thrust efficiency has increased from 0.12 to 0.18 for the cylindrical and diverging anode thrusters, respectively.

With respect to other high aspect ratio or small anode orifice thrusters, the onset limit of 21 kA is low and this fault has been traced to the gas injection geometry which has a strong effect on this limit. In the case of the diverging area thruster, moving the radius from 1.95 cm to a point closer to the anode should greatly improve the onset limit.

E. SUMMARY

Within the framework of the 1-D real gas model, the geometry effects incurred with changing electrode length and anode diameter have been explained. Increasing the electrode length has the primary effect of decreasing losses, conductivity and Hall parameter at fixed current and mass flow. Decreasing anode orifice radius has the effect of reducing the thrust efficiency and the Hall parameter at fixed operation conditions. Anode orifice radius has a strong effect on the Hall parameter, while electrode length has a weak effect. To regain a given and perhaps limiting value of the Hall parameter after a geometry change, the model shows that a large increase in J^2/\dot{m} is required for an anode radius reduction while a small increase in J^2/\dot{m} is required for lengthening of electrodes.

Again using the 1-D model, a method for integrating the stream-tube electric field to the terminal voltage is established. The resulting estimate of the terminal voltage-current characteristic agrees within 10% of that measured for a long constant cross section coaxial thruster.

A basic rule of MPD thruster design has been identified. The subsonic inlet region and the sonic location determine the terminal voltage as a function of geometry and operating conditions, while the downstream supersonic portion has only a weak effect on voltage. But the downstream supersonic portion has a strong effect on exit Mach number and thrust efficiency. This rule has been demonstrated by designing and testing a flaired, 3:1 expansion ratio thruster. The thruster has a terminal voltage as predicted by theory, and a thrust efficiency 1.5 that of a constant area, reference thruster.

Chapter 6

CONCLUSIONS

Experiments have guided the development of a 1-D, real gas model of steady, accelerating flows. Parametric agreement with experiment suggests that the model contains a reasonably complete portion of the physics governing the acceleration process. Using the model as if it were an interior diagnostic tool, the effects of electrode length and diameter changes have been explained in detail.

Two key components in thruster geometry design are electrode length and diameter, and experiments show that these have a significant effect on terminal characteristics. The theory indicates that the larger conduction volume provided by longer electrodes reduces Ohmic losses, plasma temperatures, terminal voltage, and increases thrust efficiency at a fixed current and mass flow. Reduced temperatures and higher pressures postpone the occurrence of large Hall parameters to larger J^2/\dot{m} values, and this mechanism is the suggested link between electrode geometry and the onset limit. Theoretically, both increased electrode length and reduced anode diameter will postpone the occurrence of large or perhaps critical Hall parameter values to higher J^2/\dot{m} operation, and this effect correlates with observed effects on the onset limit $(J^2/\dot{m})^*$.

Decreasing anode diameter reduces thrust at a given J^2/\dot{m} but the increased onset limit compensates for this and allows operation at larger specific impulse and thrust efficiency. By increasing the mass flux through a smaller anode, the magnetic Reynolds number is reduced at a given J^2/\dot{m} . This number is a significant dimensionless measure and large values correspond to efficient acceleration profiles. Significant increase in J^2/\dot{m} are required to restore large magnetic Reynolds numbers and efficient acceleration after decreasing anode orifice diameter. Note that electrode length can increase the magnetic Reynolds number and hence thruster efficiency as well.

The practical use of the model is in thruster design. By considering the thruster as a concentric set of quasi 1-D stream-tubes, the voltage-current characteristic, exclusive of the electrode sheaths can be estimated. Other characteristics can be estimated with this technique, and this parametric representation of geometry parameters could be used to rough-out thruster dimensions for a given set of performance figures. Confidence in this method is demonstrated by computing a voltage-current characteristic that agrees with experimental data for two long, high aspect ratio thrusters. Also, the method was used to correctly predict the voltage-current characteristic for a subsequently designed and tested low voltage, high efficiency anode.

The low voltage design confirms the theoretically suggested choking phenomena which relates terminal voltage to current, mass flow and electrode geometry. This theory indicates that terminal voltage is strongly coupled to electrode geometry upstream of and at the choking point, but is insensitive to the downstream electrode configuration. Also, at high powers the choking point is driven close to the inlet by Joule heating. The thrust of the coaxial MPD accelerator is favored by increasing the ratio of anode to cathode radius. By using a short, constant cross section inlet to establish the choking point and terminal voltage, and by using a long, diverging section downstream, a higher efficiency thruster was designed and constructed. The measured terminal voltage-current characteristic was as predicted and thrust efficiency improved by 50% over the reference thruster with a constant cross section.

There are two major problems not treated by the model. First, the electrode sheaths are very complex and are not analysed. This omission may not be deleterious as experiments^{31,37} suggest that the voltage fall at the electrodes is insensitive to current and can be less than 20% of the terminal voltage at high powers. The second major problem incurred in the use of the 1-D model is the imprecise treatment of the Hall parameter. At the electrodes, the Hall field is shorted out and the model provides solutions to a consistent set of 1-D equations with zero Hall parameter. Away from the electrodes, the Hall field and current are not zero,

and the correct formulation of this effect requires a 2-D analysis. However, the Hall effect can be approximately treated by the 1-D equations by substituting tensor conductivity in Ohm's law. The results are not exactly correct but are good enough to show the qualitative effect of tensor conductivity on the terminal characteristics.

Employing the approximate 1-D model to a coaxial electrode geometry has shown that computed voltage-current characteristics agree with experiment in two cases. Apparently, the model contains the correct parameterization of magnetic field and mass flux in spite of the actual 2-D current conduction. Other characteristics such as thrust efficiency can be estimated and are useful in thruster design by parameterizing thruster geometry.

Appendix 1

Additional Calculations for Ideal Gas Acceleration

When solutions to the 1-D ideal equations are found (3.7-3.9) with $u_0=0$, $T_0=0$, and p_0 finite, there is a small portion of the u_+ curve near the inlet that has negative temperatures. This region should be excluded from the R_m calculations for the $T_0 = 0$ case. The location where T' and $a' = 0$ again and $M^2 = \infty$ is denoted by $B'_{T=0}$. By setting $M^2 = \infty$ in equation (3.18) this point can be found:

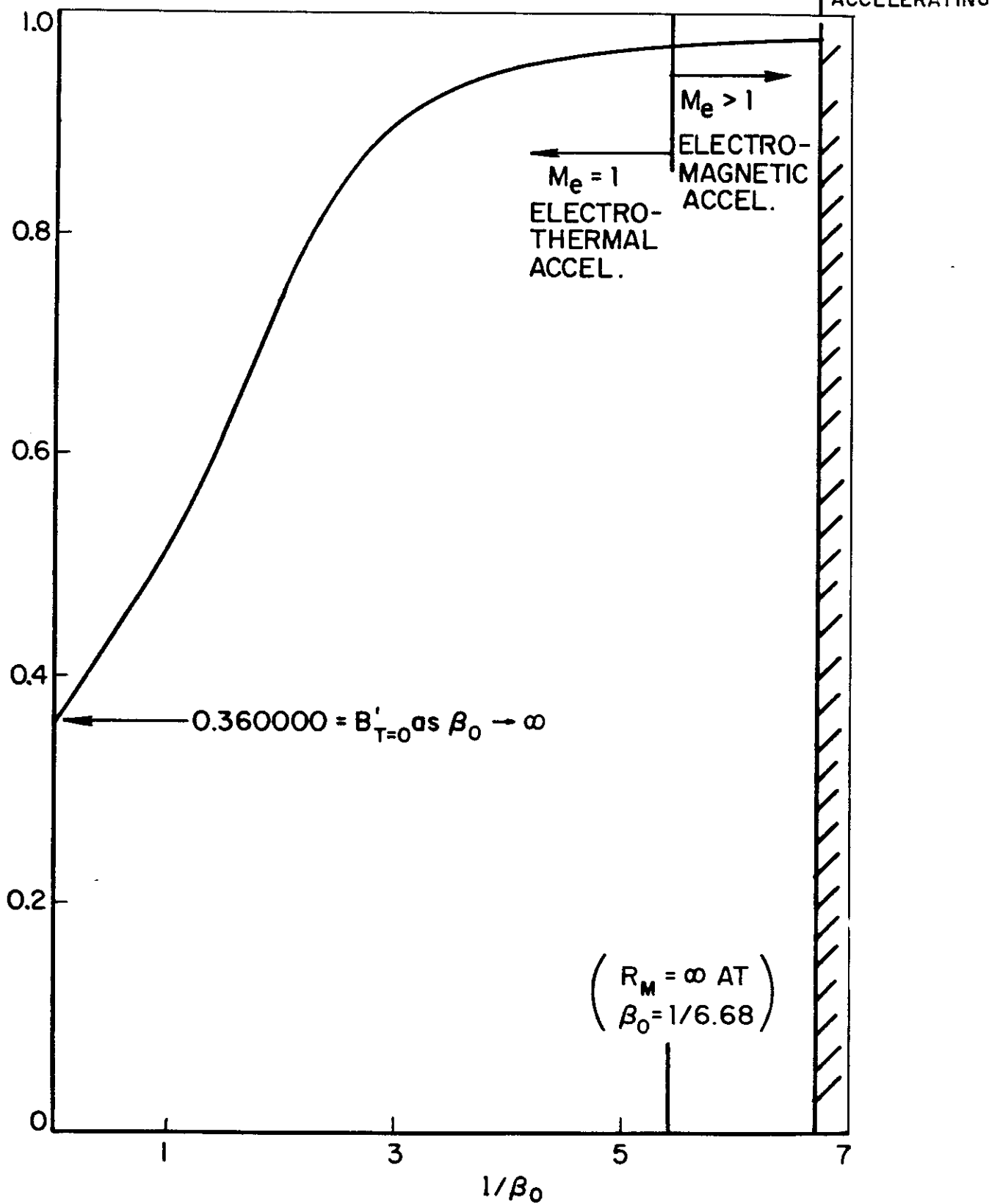
$$\frac{1}{2} = \frac{2(1 - B'_{T=0}) \mathcal{E}(\beta_0)}{(1 + \beta_0 - B'^2_{T=0})^2} \quad (1)$$

$B'_{T=0}$ has been plotted in fig. A1.1, and for the electromagnetic mode is about 0.95.

Solutions with non-zero inlet temperatures can be obtained from the general solution by a simple origin shift. Denoting shifted quantities by a hat ($\hat{}$), the following definitions ensue. Given \hat{B}_0 , \hat{F} , \hat{T}_{0s} and $\hat{\beta}_0$, the problem is to find \hat{L} .

$$\begin{aligned} \hat{B}_0 &= \alpha B_0 & ; & \alpha \hat{B}' = B' \\ \hat{B} &= B \\ \hat{u} &= u & ; & \alpha^2 \hat{u}' = u' \\ \hat{p} &= p \\ \hat{E} &= E & ; & \alpha^3 \hat{\mathcal{E}} = \mathcal{E}(\beta_0) \\ \hat{F} &= F \\ \hat{u}_m &= \frac{\hat{B}_0^2}{2\gamma_0 \hat{F}} & ; & \hat{T}_{0s}' = \frac{c_p \hat{T}_{0s}}{\hat{u}_m^2} = \frac{\hat{u}_0'^2}{2} + \hat{h}_0' \end{aligned}$$

$B'_{T=0}$



$B'_{T=0}$ VS $1/\beta_0$

FIGURE A1.1

Both α and β_0 must be found before \hat{L} . Equating the momentum and energy equations in shifted coordinates to unshifted coordinates, provides two equations:

$$\hat{u}'_0 + 1 + \hat{\beta}_0 = \frac{1 + \beta_0}{\alpha^2} \quad (2)$$

$$\hat{T}'_{0s} = 2 \left(\frac{1}{\alpha^4} - \frac{1}{\alpha^3} \right) \mathcal{E}(\beta_0) \quad (3)$$

With the stagnation temperature and $\hat{\beta}_0$ given the inlet velocity is

$$\hat{u}'_0 = \frac{\gamma}{\gamma-1} \hat{\beta}_0 + \sqrt{\left(\frac{\gamma}{\gamma-1} \hat{\beta}_0 \right)^2 + 2 \hat{T}'_{0s}} \quad (4)$$

After solving for α and β_0 numerically the magnetic Reynolds number can be computed from the general form of solution:

$$\hat{R}_m(\hat{\beta}_0, \hat{T}'_{0s}) = \alpha^2 \int_0^{\alpha} \frac{dB'}{\mathcal{E} - u' B'} \quad (5)$$

\hat{L} is found from \hat{R}_m :

$$\hat{L} = \frac{\hat{R}_m}{\mu_0 \sigma \hat{u}_m}$$

Appendix 2

Approximate Real Gas State Equation

The equation of state

$$p = \rho G(h) \quad (1)$$

is an approximation for a plasma or a chemical system of a dissociating, diatomic molecules since, at a fixed temperature, higher density or pressure favors the higher molecular weight species. For a plasma this effect is weak and (1) is a good approximation (see fig. 4.1). The isentropic speed of sound for an equation of state is derived from the second law:

$$T ds = dh - \frac{dp}{\rho} \quad (2)$$

With $dp = G d\rho + \rho \frac{dG}{dh} dh$ from (1) and $ds = 0$,

$$a^2(h) \equiv \left. \frac{\partial p}{\partial \rho} \right|_s = \frac{G(h)}{1 - \frac{dG}{dh}} \quad (3)$$

Since $G = RT$, and the textbook expression $a^2 = \gamma RT$ can be shown to be valid for $\gamma = \gamma(T)$ and $R = R(T)$, the ratio of specific heats is:

$$\gamma = \frac{1}{1 - \frac{dG}{dh}} \quad (4)$$

Conductivity

The scalar conductivity of a partially ionized plasma depends upon the electron-other collision frequency and can be written as the series resistance due to electron-neutral collisions ($1/\sigma_n$)

and due to electron-ion collisions ($1/\sigma_c$):

$$\frac{1}{\sigma_0} = \frac{1}{\sigma_n} + \frac{1}{\sigma_c} \quad (5)$$

where Capman and Cowling³⁸ give

$$\sigma_n = \frac{z}{8.210E8 (T/1E3)^{1/2} \cdot Q_{en}}$$

$z = n_e/n_a$; n_e = electron number density; n_a = ion number density;

Q_{en} = electron neutral cross section. The electron-neutral cross section is a curve fit³⁹,

$$Q_{en} = 10E-17(((-0.009926 \cdot T/1E3 + 0.3187) \cdot T/1E3 - 2.231) \cdot T/1E3 + 6.652) \quad (6)$$

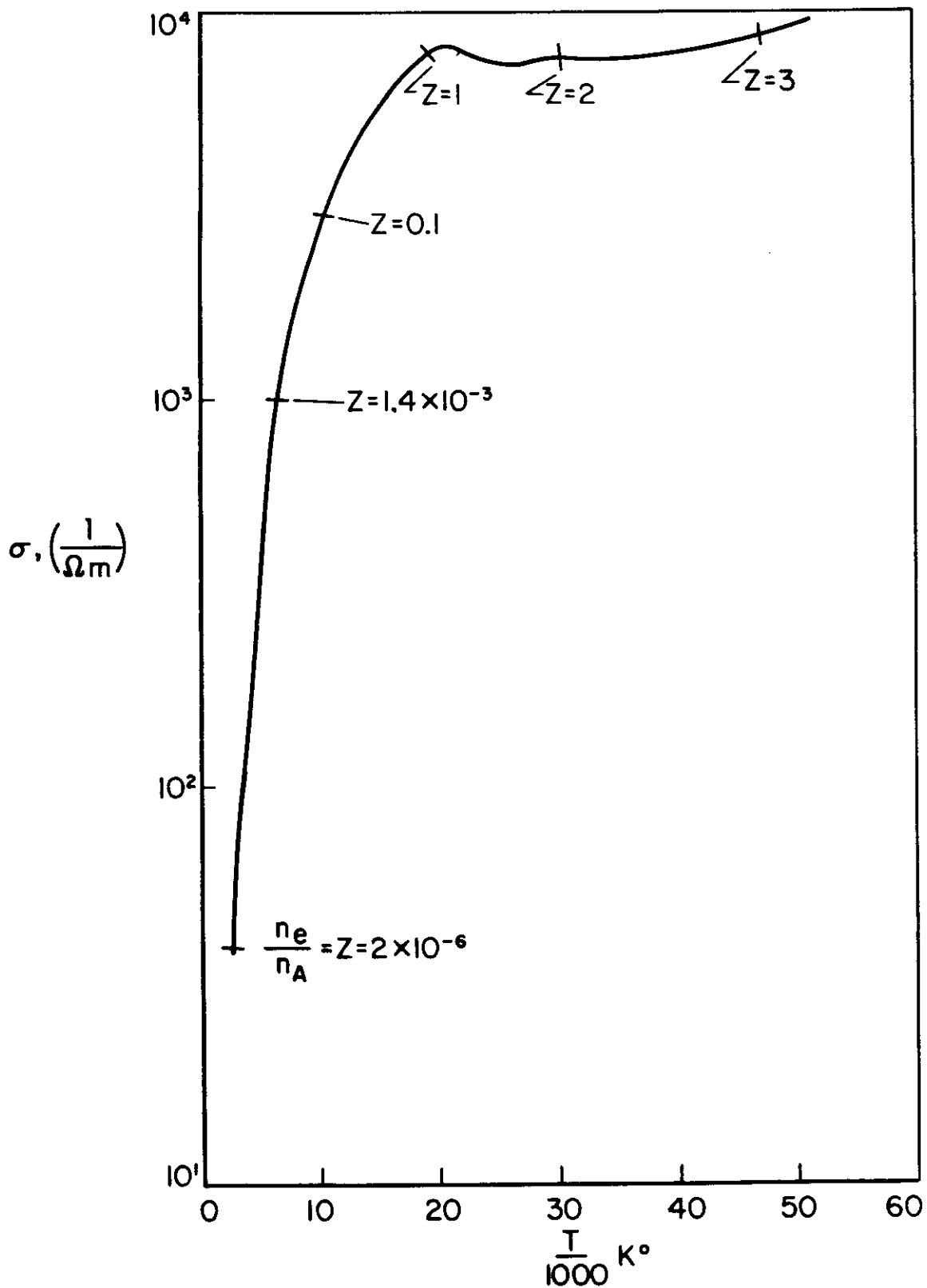
The Coulomb portion is the Spitzer-Harm formula⁴⁰,

$$\sigma_c = \frac{2 (T/1E3)^{3/2}}{2.063E-3 \frac{n_e}{n_i} \ln [0.0102 (T/1E3)^3 / (z\rho)]} \quad (7)$$

For reference, fig. A2.1 shows the conductivity as a function of temperature, and fig. A2.2 shows enthalpy as a function of temperature as used in the real gas model.

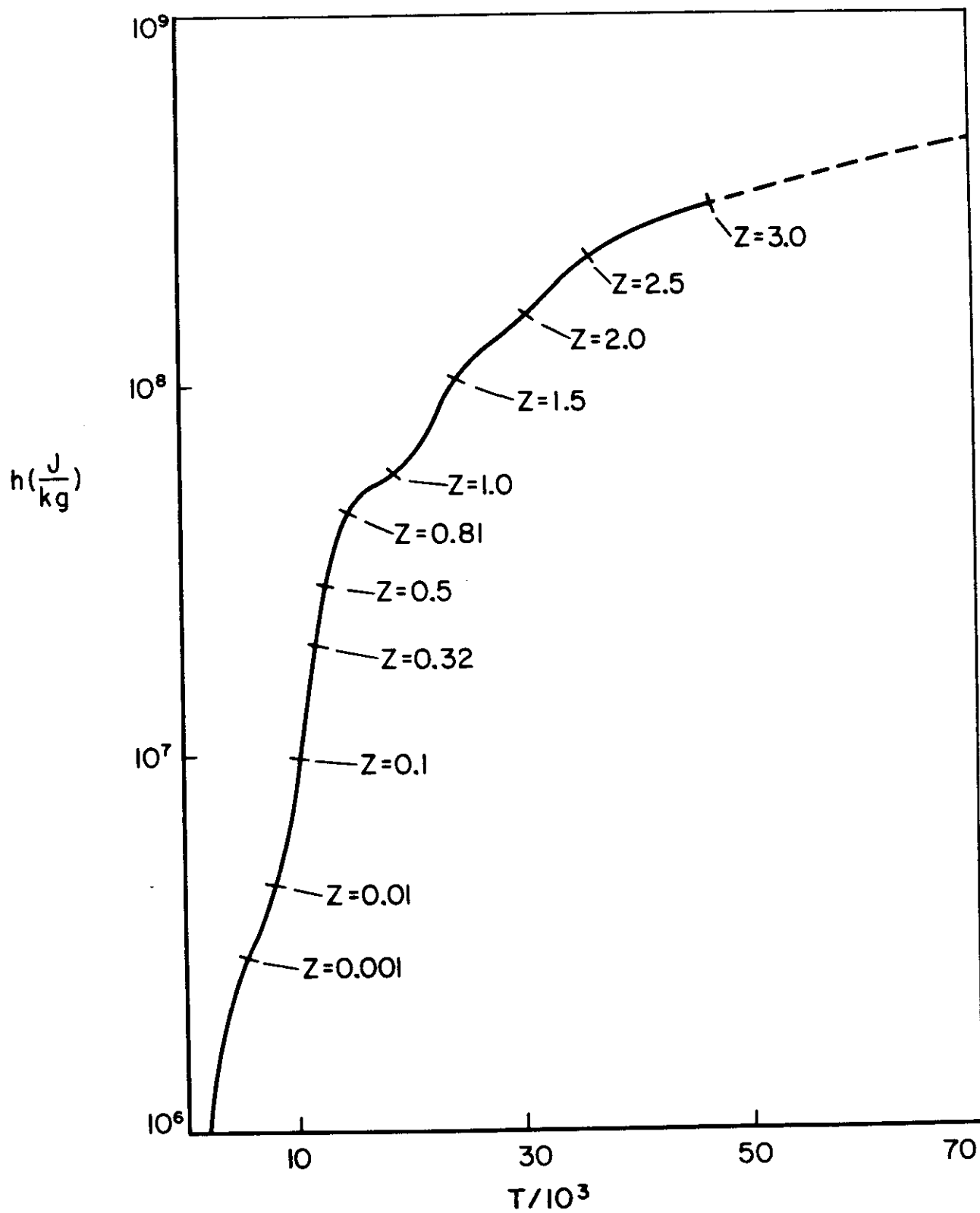
Computer Program

The function $G(h)$ is formed from a tabular, equilibrium argon equation of state in the form $R(\rho, T)$. To operate the program "MAKEARGN" only a value of ρ need be specified in MKS units and the computer will generate $G(h) = R(\rho, T)$ where ρ is the specified constant. The output is stored on a disk in a form readily used by the program "RGL".



ARGON SCALAR CONDUCTIVITY

FIGURE A2.1



ENTHALPY VS TEMPERATURE, $\rho=0.003$

FIGURE A2.2

Splined quasi Hermitian cubic polynomials are used to interpolate between points since they provide smooth monotonic curves between monotonically increasing data.

REFERENCES

- 1 Silva T.H., Byers D.C., "Nuclear Electric Propulsion Systems Utilization For Earth Orbit Transfer of Large Spacecraft Structures," AIAA paper 79-2042, 1979.
- 2 Byers D.C., "Characteristics of Primary Propulsion Systems," AIAA paper 79-2041, 1979.
- 3 Young L.E., "Solar Array Technology for Solar Electric Propulsion Missions," AIAA paper 79-2086, 1979.
- 4 Costogue E. N., Hasbak W.A, "Solar Array Technology Developements and Design Evolutions for Electric Propulsion Applications," AIAA paper 79-2086, 1979.
- 5 Austin R.E., "Solar Electric Propulsion System (SEPS) Tomorrow's Propulsion System - Today," AIAA paper 79-2045, 1979.
- 6 Buden D., "100 kWe Nuclear Space Electric Power Source," AIAA paper 79-2089, 1979.
- 7 Hudson W.R., "NASA Electric Propulsion Technology Program," AIAA paper 79-2118, 1979.
- 8 Kaplan H.M., Trn R.M., Buden D., "A Nuclear/Electric Orbital Transfer Vehicle for the Shuttle Era," AIAA paper 79-2109, 1979.
- 9 Ducati, Adriano C., Giannini, Gabriel M., and Muehlberger E., "Experimental Results in High-Specific-Impulse Thermo-Ionic Acceleration," AIAA J. vol 2 No 8, p1452, 1964.
- 10 Jahn R.G., Physics of Electric Propulsion, McGraw Hill, 1968.
- 11 Malliaris A.C., et al, "Quasi-Steady MPD Propulsion at High Power," Final Technical Report AVSD-0146-71-RR, AVCO Corporation, February 1971.
- 12 Clark K.E., "Quasi-Steady Plasma Acceleration," Ph.D. thesis, May 1969, Princeton Univ., Princeton, N.J.
- 13 Boyle M.J. and Jahn R.G., "Acceleration Processes in the Quasi-steady Magnetoplasmdynamic Discharge," Aerospace and Mechanical Sciences Report No. 1188, October 1974, Princeton Univ., Princeton, N.J.
- 14 Rudolph L.K. "The MPD Thruster Onset Current Performance Limitation," Ph.D. thesis, Nov 1980, Princeton University, Princeton N.J.

- 15 Jahn R.G. and von Jaskowsky W.F., "The Plasma Pinch as a Gas Accelerator," AIAA Preprint 63013, AIAA Electric Propulsion Conference, Colorado Springs, Colo., 11-13 Mar 1963.
- 16 Clark K.E. and Jahn R.G., "Quasi-steady Plasma Acceleration," NASA NGL 31-001-005, Aerospace and Mechanical Sciences Rept. No 859, May 1969, Princeton Univ., Princeton, N.J.
- 17 Boyle M.J., "Acceleration Processes in the Quasi-steady Magnetoplasmadynamic Discharge," Ph.D. thesis, Oct 1974, Princeton Univ. Princeton, N.J.
- 18 Boyle M.J., and Jahn R.G., "Effects of Insulator Ablation on the Operation of a Quasi-steady MPD Arc," AIAA Paper 73-1099, AIAA 10th Electric Propulsion Conference, Lake Tahoe, Nev., Oct. 31 - Nov. 2, 1973.
- 19 Jahn R.G., and Clark K.E., "A Large Dielectric Vacuum Facility," AIAA Journal, Vol. 4, No 6, June 1966, p. 1135.
- 20 Black N.A., "Pulse-forming Networks for Propulsion Research," Proceedings of the 7th Symposium on Engineering Aspects of Magnetohydrodynamics, Princeton Univ., Princeton, N.J., Mar. 30 - April 1, 1966, p. 10-11.
- 21 Jahn R.G., von Jaskowsky, W.F., and Casini A.L., "Gas-triggered Pinch Discharge Switch," NASA NSG-306-63, Aerospace and Mechanical Sciences Tech. Note No. 101, July 1964, Princeton Univ., Princeton, N.J.
- 22 Jahn R.G., and Wright E.S., "Minature Rogowski Coil Probes for Direct Measurement of Current Density Distribution in Transient Plasmas," The Review of Scientific Instruments, Vol. 36, No. 12, Dec. 1965, p. 1891-1892.
- 23 Boyle M.J., "Plasma Velocity Measurements with Electric Probes," B.S.E. thesis, April 1969, Princeton Univ., Princeton, N.J.
- 24 Rudolph L.K., Jahn R.G., Clark K.E. and von Jaskowsky W.F., "Performace Characteristics of Quasi-Steady MPD Discharges," AIAA Paper 76-1000, AIAA 12th Internotional Electric Propulsion Conference, Key Biscayne, Florida, Nov. 14-17, 1974.
- 25 Boyle M.J., Clark K.E., and Jahn R.G., "Flowfield Characteristics and Performace Limitations of Quasi-steady Magnetoplasmadynamic Accelerators," AIAA Journol, Vol. 14, No. 7, July 1976, p. 955-962.

- 26 Jahn R.G., von Jaskowsky W.F., and Clark K.E., "Pulsed Electromagnetic Gas Acceleration," NASA NGL 31-001-005 semi-annual report for period 1 July 1975 to 31 December 1975, Aerospace and Mechanical Sciences Report 634z, January 1976, Princeton Univ. Princeton, N.J.
- 27 Jahn R.G., von Jaskowski W.F., and Clark K.E., "Pulsed Electromagnetic Gas Acceleration," Semi-annual report 634ac, Jan 1977 - Mar 1978, see section by Smith W.W., p 40-49.
- 28 Clark K.E., Jahn R.G., and von Jaskowsky W.F., "Measurements of Mass Momentum and Energy Distributions in a Quasi-steady MPD Discharge," AIAA paper 72-497, AIAA 9th Electric Propulsion Conference, Bethesda, Md., April 17-19, 1972.
- 30 Turchi P.J. and Jahn R.G. "The Cathode Region of a Quasi-steady Magnetoplasma dynamic Arcjet," NASA NGL 31-001-005, Dept. AMS (now MAE) report no. 940, 1970, Princeton Univ., Princeton, N.J.
- 31 Saber A.J. and Jahn R.G., "Anode Power Deposition in Quasi-steady MPD Arcs," AIAA paper 73-1091, 1973.
- 32 Hughes, and Young, The Electromagnetodynamics of Fluids, John Wiley & Sons inc, New York, 1966.
- 33 Martinache G.H.C., "A Theory on a Parrallel Plate Accelerator," Ph.D. thesis, Princeton Univ., Princeton N.J., 1971.
- 34 Mitchner M. and Kruger C.H. Jr., Partially Ionized Gases, Plasma Physics Series, Wiley, 1973.
- 35 Lam S.H., Lectures from Dept. MAE course 582, "Plasma Dynamics," Princeton Univ. Princeton N.J., 1978.
- 36 Sparks W.M., and Fischel D., "Partition Functions and Equations of State in Plasmas," NASA SP-3066, Scientific and Technical Information Office, Washington D.C., 1971.
- 37 Jahn R.G., Clark K.E., "Pulsed Electromagnetic Gas Acceleration," Dept. MAE report, Princeton Univ, Oct 1980 - Apr 1981, section by Wolfe M.
- 38 Chapman S. and Cowling T.G., "Mathmatical Theory of Non-Uniform Gases," Chambridge University Press, London, 1952.
- 39 Lin S.C., Resler E.L., Kantrowitz A., "Electrical Conductivity of Highly Ionized Argon Produced by Shock Waves," J. App Phys. vol 26, pp 95-109, 1955.
- 40 Spitzer L. and Harm R., "Transport Phenomena in a Completely Ionized Gas," Phys. Rev., vol 89, pp 977-981, 1953.